5-2013

Impact-Acoustic Evaluation Method of Internal Crack in Rubber Composite Structure

Qin Shen
Clemson University

IMPACT-ACOUSTIC EVALUATION METHOD OF INTERNAL CRACK IN RUBBER COMPOSITE STRUCTURE

A Dissertation
Presented to
the Graduate School of
Clemson University

In Partial Fulfillment
of the Requirements for the Degree
Doctor of Philosophy
Automotive Engineering

---

by
Qin Shen
May 2013

Accepted by:
Dr. Mohammed A. Omar, Committee Chair
Dr. Thomas R. Kurfess, Co-Committee Chair
Dr. Laine Mears
Dr. Timothy B. Rhyne

ABSTRACT

The main objective of this work is to investigate the impact acoustic method as a means of nondestructive testing (NDT) for internal cracks in a rubber composite structure, such as that found in a tire. As demonstrated in this dissertation, this approach is an effective and economical alternative to the current NDT methods for tires casing integrity inspection. There are two separate aspects of the impact acoustic signals considered in this work: the impact force signal and the resultant acoustic signal. First, a contact dynamics model is developed based on the Hertz's impact theory and modified for rubber composite materials. The model generates prediction of major impact dynamics quantities, which are theoretically proven to be sensitive to the existence of internal structural cracks. For the purpose of applying the impact acoustic method for tire casing integrity inspection, models are developed for simplified tire structures, which are a cubic shape comprised of rubber compound material without reinforcements. The prepared cubic rubber samples are designed to roughly approximate the profile of the sectional tire casing and the cracks embedded at the belt edge in the shoulder area. The rationality of the simplification is explained both theoretically and experimentally.

Based on comprehensive theoretical analysis of the impact acoustic signals, several direct and indirect experimental features are identified that are equivalent to the theoretical dynamic quantities, thus correlated to the presence of internal crack. The experimental discriminators can be extracted from either impact force signal or acoustic time- and frequency-domain signal. They are verified as promising indicators of internal crack in both simplified cubic rubber structures and complicated tire casings. Integration

of the experimentally extracted discriminators helps to mitigate the deficiencies and noise caused by relying heavily on a single discriminator, while providing an integrated index identifying the damage conditions with good accuracy and robustness.

DEDICATION

I'd like to give my thanks to my advisors Dr. Omar and Dr. Kurfess and the other two professors Dr. Mears and Dr. Rhyne on my committee team. Thank you so much for your guidance and comments on my work. Thanks to my advisors for supporting me throughout the four years of my doctoral research. Also I need to give my sincere thanks to the two project superintendents from Michelin, Frank and David. It was really invaluable experience for me to work with you over the last two years. Thanks for providing me with this opportunity.

Also thanks to my lab colleagues, especially to Dr. Gheorghe Bunget, who has dedicated a lot to this work and gave me many advices. I'm very grateful of him. And also I would like to give all my appreciations to my fellow graduate students at ICAR and my friends, and family back in China.

TABLE OF CONTENTS

Page

LIST OF FIGURES

LIST OF TABLES

LIST OF SYMBOLS

A_1	:	Accumulated area under the initial contact sound waveform
A_2	:	Accumulated area under the ringing sound waveform
c	:	Sound wave speed
C_h	:	Hysteretic damping coefficient
C_f	:	Equivalent viscous damping coefficient
d_{max}	:	Maximum deformation
D, D_1, D_2	:	Distance from the point source of sound to the sound receiver
e	:	Restitution coefficient
E_1	:	Elastic modulus of the impactor
E_2	:	Elastic modulus of the impacted target
E_f	:	Accumulative spectral energy of higher frequency range
f	:	Frequency of sound
f_c	:	Resonant frequency subjected to local contact force
f_i	:	The left boundary of the interested higher frequency range
f_{max}	:	The left boundary of the interested higher frequency range
F_{avg}	:	Average impact force during collision
F_c	:	Contact force
F_{max}	:	Maximum impact force
$G(f)$	:	Microphone gain at a given frequency
h	:	Crack depth
h_1	:	Drop height in rebound test
h_2	:	Rebound height in rebound test
k	:	Structural stiffness
K_c	:	Nonlinear contact stiffness
K_f	:	Bending stiffness
l	:	Crack length
l_e	:	Effective crack length
m_1	:	Mass of the impactor
m_2	:	Mass of the impacted target
Nor_RMSE	:	Normalized root-mean-squared-error
P_f	:	Local peak spectral density at higher frequency
PR	:	Accumulative power ratio
$PSD(f)$	:	Power spectral density at a given frequency
r_1	:	Radius of the impactor
r_2	:	Radius of the impacted target
R	:	Rebound resilience
$\tan\delta$	:	Loss tangent

U, U_1, U_2	:	Voltage of the electret microphone recorded at a given distance from the point source of sound
U_c	:	Resonant vibration energy
U_f	:	Flexural vibration energy
V_i	:	Impact velocity
w	:	Width of the impacted target
x_1	:	Displacement of the impactor
x_2	:	Displacement of the impacted target
α	:	Relative contact deformation
α_{max}	:	Maximum contact deformation
δ_f	:	Bending deflection
δ_{fmax}	:	Maximum bending deflection
ΔPR	:	Difference of power ratio values
ΔV_i	:	Relative approach velocity before impact
ΔV_f	:	Relative separation velocity after impact
λ	:	Impact energy loss factor
τ	:	Impact duration
υ_1	:	Poisson's ratio of the impactor
υ_2	:	Poisson's ratio of the impacted target
ω_n	:	Natural frequency
ω_i	:	i-th modal frequency of the structure

LIST OF ABBREVIATIONS

CIA: Casing integrity analyzer

DOF: Degree of freedom

NDT: Nondestructive testing

P-wave: Primary (longitudinal) wave

RMSE: Root-mean-squared error

R-wave: Rayleigh (surface) wave

S-wave: Secondary (transverse) wave

1 INTRODUCTION

Truck tire retreading industries have been reported as the largest remanufacturing industry in the United States. Retreading not only extends the service life of the tires, but also is significantly less expensive than manufacturing new tires (Boustani, et al., 2010). Recycling and retreading is the key for reducing costs and energy used for manufacturing of the tire casings, thus the cost per mile for operations. An effective retread necessitates a tire casing with good structural integrity, without internal damages. As a result, a reliable non-destructive testing (NDT) technique to accurately determine the internal damages in a tire casing is highly demanded. However due to the high cost of the existing tire casing inspection techniques such as shearography, thermography and ultrasound, tire retreading business is normally restricted to the markets where the consumption of truck tires is significantly large (RMA, 2009). Therefore the development for a cost effective NDT technique for the purpose is clearly demanded.

In addition to those common types of NDT techniques used for tire defect inspection, there is growing interest to a promising and intuitive solution – the impact-acoustic methods. Impact-acoustic methods for structural integrity assessment have not been comprehensively investigated until the end of 20^{th} century (Ito, et al., 1997). They are essentially NDT technique based on applying a local disturbance on structural surface while recording the resulting airborne sound waves. Significant research based on impact-acoustic method is driven by the fact that the human ear can capture the difference in the sound while tapping or hammering the structure. An automation of this

procedure would make the test operation more efficient, less subjective and operator independent. Impact-echo (Sansalone, et al., 1986) and ultrasonic (Rens, et al., 1997) methods are the similar type of NDT techniques based on the use of stress (sound) waves. (The comparison among these methods will be discussed in Chapter 2.) There have been numerous applications of the impact-echo and impact-acoustic methods, including thickness measurements of concrete slabs (ASTM C 1383), void localization and quantification of defects in concrete structures (Sansalone, et al., 1986; Asano, et al., 2003), and quality control of round fruits to ensure firmness and maturity (Armstrong, et al., 1990). However, rather few attempts using impact-acoustic method have been made for the purpose of defect detection in rubber composite structures (Heirtzler, et al., 2002), and those few are usually limited to insufficient theoretical explanations.

Truck tire casings as typical rubber composite structures are mainly composed of rubber compounds and reinforcing steel cords (Mark, et al., 2005). Tire challenges almost all engineering disciplines. For example from the aspect of material properties, rubber compounds used in tires are seriously inelastic, and the steel cords are not homogeneous. The presented research addresses the linearized simplification of the tire structure in the case of impact-acoustic method. Besides, knowledge about the tire structure including components and macro shape effects is essential to the success of the field work.

The purpose of this work is to investigate and analyze the dynamic response of rubber composite structure to an impact. The impact force signal has been identified as a useful means to characterize the impact response from testing on a rubber composite structure. Furthermore the impact induced acoustic signal can be studied in two separate

stages: (1) initial contact sound due to local deformation at the impact region; (2) ringing sound due to free vibration of the structure. Both parts of the impact sound were demonstrated as related to the structural properties, which can be used to determine the existence of the structural defects. An integrated approach by measuring both impact force and the impact sound is adopted in this work, and analytical modeling are provided to explain the relationship between the impact acoustic signals and the internal cracks. Experimental validations are performed on both the rubber structure solved by the analytical model and the complex tire casings.

2 LITERATURE REVIEW

2.1 Nondestructive Evaluation Methods used for Rubber Composite Structures

Before or after a truck tire casing has been retreaded, a non-destructive inspection method is usually suggested to guarantee the remanufacturing quality. The primary purpose of this inspection procedure is to detect and locate internal defects such as cracks, voids or foreign material. Numerous attempts have been made for this purpose using advanced NDT techniques, and several types of inspection procedures have been authorized by the tire remanufacturing industry and commercialized as well. The most prevailing NDT methods which were or are being used for tire casing integrity detection are outlined in details as follows.

2.1.1 X-ray Examination

Industrial radiography with X-ray has been emphasized as a real-time method for tire inspection since 1950s (Forney, 1974). It provides high sensitivity to such types of defects as foreign materials or porosity due to that the variations in the radiation intensity of the X-rays penetrating through different materials, however smaller bonding defects can be difficult to detect (Berger, 1981). The penetration capability of the X-rays is dependent on the material densities, therefore is limited to evaluate the condition of non-steel reinforcement due to the similarity in densities of polyester, rayon, nylon and rubber.

The commercial X-ray devices applied for tire casing inspection can be used to examine the status of the steel belts and cables hidden within the casings. It can possibly

identify severe damage conditions such as zipper failures, run flat abuse, road hazardous damages, and so forth through early identification to eliminate the tire casings which are not qualified for remanufacturing. Figure 1 shows a typical X-ray setup where the X-rays pass from the center of the tire to the detector. X-ray examination technique is relatively less expensive than other NDT methods and useful for several areas of damage conditions in the tires, however further inspection procedures are required to investigate those conditions which are not detectable by X-rays.

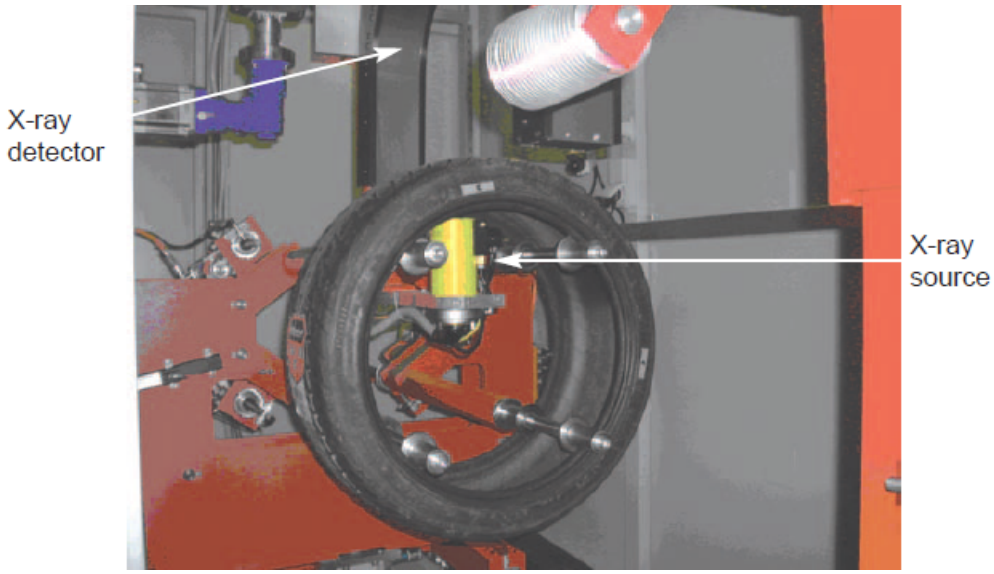

Figure 1: Typical X-ray setup (Gent, et al., 2005)

2.1.2 Holography and Shearography

Holographic interferometry has been another powerful technique for bonding integrity evaluation. It is a method that measures displacements produced by pressure, thermal or mechanical stressing applied to the surface of the test object (Borza, 1998).

Holography is extremely sensitive to environmental vibration, and found later not as efficient as shearography method for tire voids detection. The shearography was developed by Hung in 1974 as an enhanced laser interferometry technique by measuring displacement gradients directly (Hung, 1974). It has been proved to be remarkably insensitive to environmental vibration compared to holography method, and it can be easier to correlate internal defects with the variances in displacement gradients than in actual displacements.

A schematic diagram of a digital speckle shearing interferometer is shown in Figure 2, where the test object is illuminated with laser light source. The reflected light rays pass through a shearing device which allows each point to be mapped into two points in the image plane. The two sheared points interfere with each other producing a speckle image, which will change due to the deformation on the object surface. A fringe

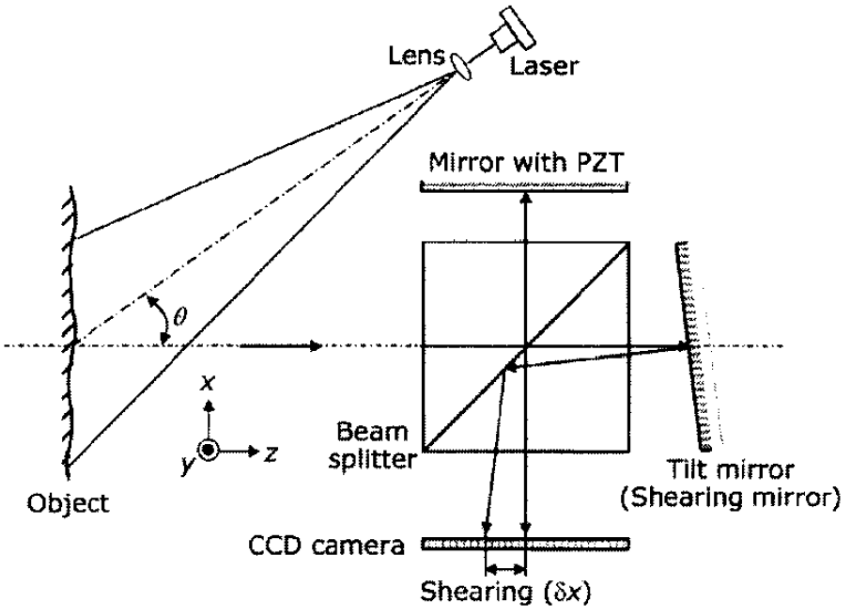

Figure 2: Digital Speckle Shearing Interferometery (Kim, et al., 2004)

pattern is then produced by comparing the two speckle images before and after the deformation to depict the surface strain distribution. An internal defect usually induces strain concentrations under stressing which can cause differences between the two speckle images and be translated into an anomaly in the fringe pattern (Hung, Shearography for non-destructive evaluation of composite structures, 1996; Kim, Kang, Jung, & Ko, 2004).

Shearography technique used for tire casing inspection can detect various types of defects such as voids and delaminations in belts and sidewalls. When a tire is under test using shearography device, it is firstly scanned by the laser light placed in the center of the tire casing under normal atmospheric pressure to obtain a baseline photograph. Then the tire casing is placed in a vacuum such that if there is an anomaly such as an air filled void, the low pressure around the casing causes the air trapped in the void to expand. A stressed photograph is obtained by scanning the tire casing under vacuum, and compared with the baseline photograph to produce a fringe pattern. Figure 3 shows a processed image which reveals the discontinuous anomalies in the belt edge area of a tire casing.

However, shearography device is usually overly expensive and time consuming for large batches of examinations. Interpretation of the shearogram is difficult which often requires a skilled operator. It has also been discovered that detection of defects which are less sensitive to stressing (e.g. voids far away from the inner contour of the tire casing) can be difficult. The knowledge about damage conditions in actual tire samples in this thesis is largely relied on but not limited to the shearograms.

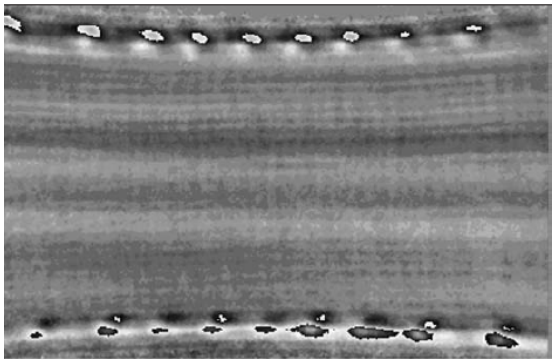

Figure 3: Shearogram of the crown area of a tire (Gent, et al., 2005)

2.1.3 Ultrasonic

The ultrasonic method as a powerful NDT tool has been widely applied to quality control in manufacturing. Ultrasound vibrating at higher frequencies (usually 1-10MHz used in the tire industry) attenuates much faster in the air than the audible sound; therefore, coupling material is normally required to guarantee sufficient energy transmitted to the test object. The ultrasonic method can be used to examine abnormal cord spacing, belt anomalies or change in the wall thickness of a tire. The principle of the ultrasonic testing is that the reflection and refraction of the ultrasound waves are dependent on the median properties such as acoustic impedance. Change in the propagating path of the ultrasound waves can result in differences in the received waveforms.

Automation of this testing procedure is difficult due to the need for coupling medium between the transducer and the object surface. The most common way is to immerse the tire in a water tank to used water as coupling material (Downs, et al., 1999).

Air-coupled ultrasonic technique is another solution that has been applied in tire inspection (dos Reis, et al., 2000), but is limited to low spatial resolution. The ultrasonic method is normally expensive and also requires much skill, training and experience to interpret the data.

2.2 Impact-Echo and Impact-Acoustic Method

2.2.1 Impact-Echo Method

The impact-echo method relies on sensing the surface displacement after local mechanical disturbance. The propagation of impact-induced transient stress waves in the test object varies due to the presence of internal defects such as disbanding or delaminations. Piezoelectric based transducers measure the surface displacement response by contacting with the test object. Earlier researchers in this field have used impact-echo for integrity testing in concrete structures (Sansalone, et al., 1986).

In the case of either impact-echo or impact-acoustic method, the material undergoes very small strains, thus only the initial tangent modulus is relevant which greatly reduces the complexity of the problem. Linearized approximation is an important and fundamental assumption which supports all the solutions mentioned in this work.

Study of three dominant types of stress waves (P wave, S wave and R wave) propagating through the solids are the key to understand the stress wave responses. R-wave travels along the surface, while P-wave and S-wave propagate into the solid structure along spherical wave fronts as illustrated in Figure 4. Frequency-domain

characteristics such as resonant frequency are mostly focused, which is an inverse value of the time that dominant stress waves travel in the solid. (Sansalone, 1986).

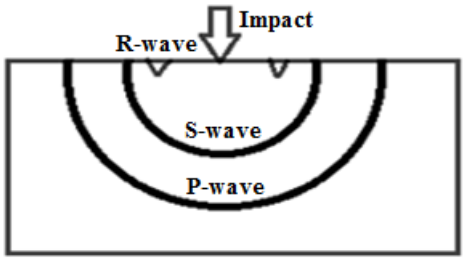

Figure 4: Impact-induced transient stress waves propagation in a solid plate

The presence of an internal damage such as delamination in the propagation path of the P and S waves yields change in the received stress waves. Thickness measurement is based on observed “resonant” frequency which is essentially an inverse of the travel time between the top and bottom of a solid. A disbonding crack with a large transverse length will cause sufficient reflections of stress waves on the disband interface which shorten the traveling path, hence yields a resonant frequency higher than the thickness frequency. However a smaller crack where P-wave can still pass through along the crack edges yields sheared waves which vibrate in a perpendicular direction to the P-wave. As a result the one-way traveling path is slightly longer than the thickness depending on the size of the crack, and the resonant frequency is therefore shifted lower.

Impact-echo responses in the plate structures are dominated by the P-wave mode, however wave reflections from the structure boundaries of the circular cross-sections can change the wave patterns. Multiple reflections of stress waves within a cross-section perpendicular to the axis excite cross-sectional modes of vibration, which requires

adequate attention in the study of impact-echo response (Lin, et al., 1993; Lin, et al., 1994a; Lin, et al., 1994b).

One limitation is that impact-echo is essentially a contact NDT method, which requires a careful design of the mechanism enabling the transducer to approach or leave the testing surface to realize robust online testing. The displacement signal can be greatly influenced by an uneven surface that is not capable to provide a fully contact.

2.2.2 Impact-Acoustic Method

The impact-acoustic method replaces the contact transducer with an air-coupled transducer, which records the sound waves generated by the vibration of the neighboring structure excited by an impact. The impact generated dynamic response of the structure results in compression and rarefaction of the surrounding air, thus forming the concentric wave fronts of increased and decreased pressure originated from the point of contact. The sound pressures monitored by a microphone near the impact location correspond to the movement history of the target.

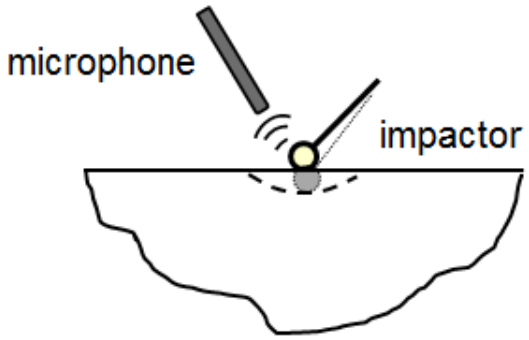

Figure 5: Illustration Diagram of Impact-acoustic Testing

The initial stage of the acoustic signal is due to the deformation and restitution of the target within the duration of impact, in Figure 5. It is not only valuable to analyze the acoustic signal in this stage, but also the corresponding impact force contains substantial structural information. The rest of the acoustic signal is produced by free vibration of the structure. The embedded internal damages dissipate the energy from the resonant modes to other flexural modes, which can be observed in the frequency domain using the Fourier Transform.

Impact dynamics has been vigorously studied with the birth of the science of mechanics. The Hertz's law of contact (Goldsmith, 1965) provided a solution to predict accurately most of the impact parameters that can be experimentally verified. The impact force response is correlated with the various properties of the target and the impact parameters. The details of the impact dynamic analysis are discussed in this work (see in Chapter 3) and applied to internal damage evaluation.

According to acoustics theory, the intensity of sound is directly proportional to the square of the amplitude of source vibration. It provides the basis to incorporate vibration analysis of the structure to explain the acoustic response. Some researchers (Mujumdar, et al., 1988; Zou, et al., 2000) have derived comprehensive analytical models to estimate the flexural vibrations influenced by embedded damages in the structure. Most of these studies rely heavily on mode modeling and frequency-domain analysis on experimental data.

Energy based analysis of the structure is another useful approach to understand the effect of embedded damages on the impact behavior. The differences of the material

properties of the two colliding bodies result in energy loss, which is dependent upon properties such as stiffness, density, shape and so forth. Based on the modeling of energy loss in the impact process, it was analytically and experimentally proved that the intensity of sound excited by flexural vibration after impact can be used as an indicator for the structural integrity identification (Luk, et al., 2011).

It is much easier to implement automation by using the impact-acoustic method compared to impact-echo. The non-contact NDT method can enhance the robustness of the measurements. Impact-acoustic signal is sensitive to the environmental noises, which can be fixed by various techniques such as using noise cancelling microphone or phase-arrayed microphone noise cancelling algorithm. Rubber composite material as the test object in this research is almost new to the application of impact-acoustic method, which requires special emphasis to address the simplification and linearization problems. This research studies simplest cubic blocks of rubber composite material initially, and then extends the evaluation methods to the actual tire measurement.

3 IMPACT DYNAMICS ANALYSIS

3.3 Theoretical Basis for Impact Dynamics

3.3.1 Introduction

Impact behavior usually involves the description of the impact momentum change, transient stresses, contact forces, deformations and so forth. Based on the impact-induced transient stresses, the behavior of impacted solids can be divided into different regimes. For stresses below the yield strength, materials behave elastically. Two extremes of this regime are: a perfectly elastic impact, and a perfectly inelastic impact. The restitution coefficient *e* introduced by Newton is a dimensionless quantity, usually between 0 and 1. It is a measure of the energy loss during impact, defined as the ratio of the relative separation velocity after impact, ΔV_f, to the relative approach velocity before impact, ΔV_i:

$$e = \frac{\Delta V_f}{\Delta V_i} \qquad \text{Eq. 1}$$

For a perfectly elastic impact, the kinetic energy of the system is fully conserved, thus $e=1$; while for a perfectly inelastic impact, the two bodies coalesce and move as a single mass after impact, so $e=0$. However, most impacts are intermediate between perfectly elastic and perfectly inelastic corresponding to $0<e<1$, which are called partially elastic impact.

Another regime of impact is where the loading intensity is increased such that the stresses exceed the yield strength. The material behaves in the plastic range and usually

involves failure of the impact body. The deformation history of an impact normally consists of approach phase and restitution phase, see Figure 6.

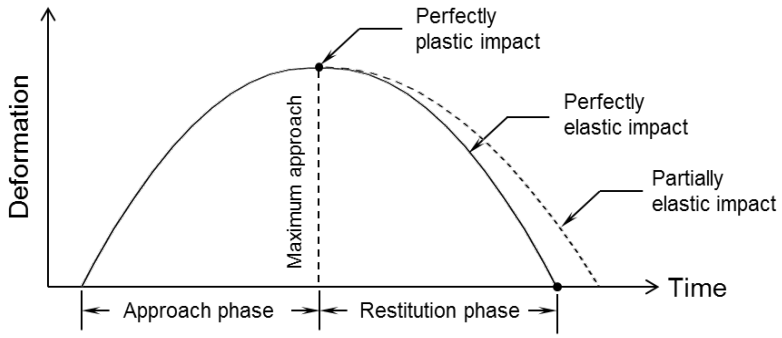

Figure 6: Deformation history of different impact regimes

Impact-acoustic method is discussed in the regime of partially elastic impact, in which the restitution coefficient e is between 0 and 1. In this situation, part of the impact energy is transmitted into the impacted target, and the rest of them conserved into the impactor. Three major interests are normally discussed in this regime: contact mechanics, impact energy loss and elastic wave propagation. Contact mechanics is mainly concerned with contact force, deformation and impact duration. Impact energy loss can be addressed by the impulse momentum theory based on classical mechanics, given the knowledge of the coefficient of restitution. Elastic wave propagation in the impacted solid transforms into vibrations, which extensively relies on the wave propagation approach (Zukas, et al., 1992). Effective models of these subjects allow us to theoretically study the effect of structural parameters and apply the model for defect identification. In this thesis, a contact mechanics model describing the impact dynamics associated with the impact-acoustic signal is generated. Then the model quantities will be linked with the presence of

internal cracks in the impacted target to determine the defect discriminators. Meanwhile, the connections between the impact acoustic signals and the model quantities are significant for practical defect inspection. This chapter mainly focuses on the development of contact mechanics model and sensitivity analysis of the model.

3.3.2 Impact Energy Loss

To derive the analytical solution for the partially inelastic impact dynamic process, the restitution coefficient *e* is a significant parameter. In the case of rubber materials which involve a non-negligible nonlinear hysteretic damping effect, impact energy loss is majorly associated with the hysteretic damper. There are various experimental means to determine the restitution coefficient *e*. It was pointed out (Goldsmith, 1965) that the combined coefficient of restitution *e* is related to like-material coefficients e_1, e_2 and respective elastic moduli, by the equation

$$e = \frac{e_1 E_2 + e_2 E_1}{E_1 + E_2} \qquad \text{Eq. 2}$$

Judging from the expression, the structural stiffness can influence the coefficient of restitution. If $e_1 > e_2$(e.g. a steel impactor and a rubber target), then a reduced target stiffness (E_2) can result in a smaller e, which means more energy is lost. Theoretically the existence of an internal crack can reduce the structural stiffness, and the flexural vibration introduced by the crack will dissipate the total energy. The energy loss factor λ can be calculated on the basis of the coefficient of restitution as

$$\lambda = 1 - e^2 \quad \text{Eq. 3}$$

This measure of energy dissipation is similar as the rebound resilience *R* (Gent, et al., 2005) which is an important index that estimates the loss properties of rubber. The resilience R is usually measured from a drop test, which can be determined by taking down the drop height h_1 and rebound height h_2, then derived as

$$R = e^2 = {}^{h_2}/_{h_1} \quad \text{Eq. 4}$$

In this case, the λ can be written as

$$\lambda = 1 - R \quad \text{Eq. 5}$$

3.3.3 Integral Model based on Hertz's Contact Mechanics Model (Zukas, et al., 1992)

First, a general case of a spherical solid impacting an isotropic integral target is considered. A single degree-of-freedom spring-mass-damper system is used to describe the impact dynamics model as in Figure 7.

The mass and displacement of the impactor are denoted as m_1 and x_1, and those of the target are denoted as m_2 and x_2. The relative deformation due to local compression at the center of the contact surface is

$$\alpha = x_1 - x_2 \quad \text{Eq. 6}$$

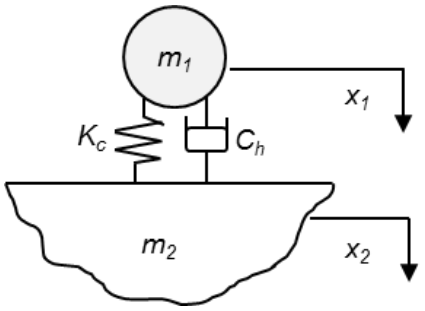

Figure 7: Single DOF spring-mass-damper model of an impact

The penetration velocity accordingly is defined as

$$\frac{d\alpha}{dt} = \frac{dx_1}{dt} + \frac{dx_2}{dt} \quad \text{Eq. 7}$$

Initial approaching velocity is denoted by impact velocity V_i, which is equivalent to $\dot{\alpha}|_{t=0}$.

According to the Hertz's contact model with hysteretic damping (Goldsmith, 1965), the impact force is related to the relative displacement and penetration velocity by

$$F_c = K_c\alpha^{3/2} + C_h\dot{\alpha} \quad \text{Eq. 8}$$

The term K_c is the nonlinear contact stiffness, C_h is the hysteretic damping coefficient, and respectively defined as

$$K_c = \frac{4}{3\pi} \cdot \frac{\sqrt{\bar{r}}}{k_1 + k_2} \quad \text{Eq. 9}$$

$$C_h = \xi\alpha^{3/2} \quad \text{Eq. 10}$$

where $\bar{r} = r_1 r_2/(r_1 + r_2)$, $k_i = (1 - \nu_i^2)/E_i,\ i = 1,2$, E and ν are the Young's modulus and Poisson's ratio. r is the colliding sphere radius. For non-spherical colliding bodies, the equivalent radius can be estimated as:

$$r_i = \sqrt[3]{\frac{3m_i}{4\pi\rho}} \quad \text{Eq. 11}$$

The subscripts 1 and 2 refer to the impactor and the target. ξ is the damping constant which can be expressed as (Muthukumar, 2003):

$$\xi = \frac{3K_c(1-e^2)}{4V_i} \quad \text{Eq. 12}$$

Therefore the contact force expression can be rewritten as:

$$F_c = K_c\alpha^{\frac{3}{2}}\left[1 + \frac{3(1-e^2)}{4V_i}\dot{\alpha}\right] \quad \text{Eq. 13}$$

Based on the energy method by equating the energy loss derived from the momentum impulse approach and the one derived from hysteretic damping at time *t*, the penetration velocity $\dot{\alpha}$ can be found in terms of the relative contact deformation α as:

$$\frac{d\alpha}{dt} = \sqrt{V_i^2 - \frac{4}{5}K_cM\alpha^{5/2}} \quad \text{Eq. 14}$$

where $M = \frac{1}{m_1} + \frac{1}{m_2}$. Therefore the maximum local contact deformation α_{max} can be calculated by substituting $\dot{\alpha} = 0$ into Eq. 14 as

$$\alpha_{max} = \left(\frac{5{V_i}^2}{4K_cM}\right)^{2/5} \quad \text{Eq. 15}$$

As a result, the maximum impact force is

$$F_{max} = K_c \cdot \left(\frac{5V^2}{4K_cM}\right)^{3/5} \quad \text{Eq. 16}$$

The impact duration τ can be estimated based on the relationship between impulse and momentum in terms of the formula as

$$F_{avg} \cdot \frac{\tau}{2} = m_1 V_i \quad \text{Eq. 17}$$

where F_{avg} is the average impact force during the collision, and the force-time curve approximated as sinusoidal can be written by an equation

$$F_c = F_{max} sin\left(\frac{\pi}{\tau} t\right) \quad \text{Eq. 18}$$

Therefore, F_{avg} is related to F_{max} by a simple ratio as

$$F_{avg} = \frac{2}{\pi} \cdot F_{max} \quad \text{Eq. 19}$$

Substitution of Eq. 19 into Eq. 17 yields the expression for the impact duration as

$$\tau = \frac{\pi\, m_1 V_i}{F_{max}} \quad \text{Eq. 20}$$

The three dynamic quantities discussed in the contact mechanics model are the maximum impact force F_{max}, the impact duration τ and the maximum contact deformation α_{max}. All of these quantities are related to the masses, the impact velocity V_i, the contact stiffness K_c and the restitution coefficient e, where K_c is dependent on the material properties of the two impact bodies. The effects of these parameters on the contact dynamics quantities will be studied through the sensitivity analysis later on.

3.4 Defect Model of Contact Mechanics

A thin transverse crack is introduced in the structure to generate a defect model of contact mechanics. The impact system is approximated as a second degree-of-freedom spring-mass-damper model, as in Figure 8.

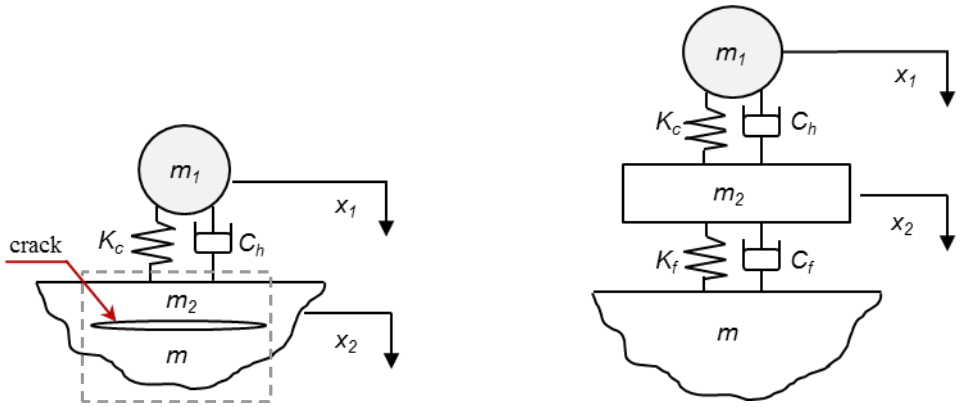

Figure 8: Two DOF spring-mass-damper model of impact system with embedded crack

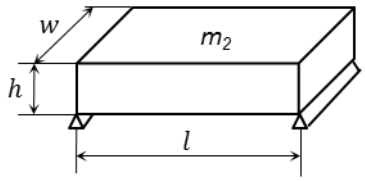

Figure 9: Materials above the crack modeled as a thick plate
freely supported at two opposite edges

Consider that the transverse area of the crack is much larger than the contact area of impact, it can be assumed that the impact only excites local dynamic vibrations. Therefore, in a planar model, the material above the crack can be simplified as a flexural plate supported at both ends of the crack as shown in Figure 9. The rest of the materials beneath the crack is so large that it can be treated as an infinite mass. Similar as the integral model, the flexural plate m_2 is subjected to the impact force by the impactor m_1 through the contact stiffness K_c and the damper C_h. But the flexural plate will deflect further down by a bending stiffness K_f and be damped by a hysteretic damper C_f.

The equation of motions of the system can be written as

$$F_c = -m_1 \frac{dx_1^2}{d^2t} = K_c \alpha^{\frac{3}{2}} \left[1 + \frac{3(1-e^2)}{4V_i}\dot{\alpha}\right] \quad \text{Eq. 21}$$

$$F_c = m_2 \frac{dx_2^2}{d^2t} + K_f x_2 + C_f \frac{dx_2}{dt} \quad \text{Eq. 22}$$

The local flexural plate m_2 has length of l which is taken as the transverse size of the crack, and thickness of h as the depth of the crack. Bending stiffness of a plate K_f with simply supported edges is solved as (Roark, 1954)

$$K_f = \frac{4\pi h^3}{3l_e^2} \cdot \frac{E_2}{(1-\nu_2)(3+\nu_2)} \quad \text{Eq. 23}$$

where l_e is defined as effective length determined by the aspect ratio of block width to actual crack length w/l as presented in Figure 9. Considering that the impact is uniformly distributed over a fairly small circular area (i.e., radius of contact area $c_r = 0$), the ratio of the effective length l_e to the actual length of crack l is given in Table 1. All the rest of the aspect ratio scenarios which are not listed in the table can be satisfied by interpolating the given values linearly. For a given block width w, the increase in the actual length of crack l leads to a smaller effective length ratio l_e/l.

Table 1 Ratios of the Effective Length to the Actual Length of Crack

l_e/l	$w/l = 1$	$w/l = 1.2$	$w/l = 1.6$	$w/l = 2$	$w/l = \infty$
Central loading $c_r = 0$	0.568	0.599	0.633	0.648	0.656

The equivalent viscous damping C_f is used to define a hysteretic material to formulate the problem as the viscous materials. By comparing the energy loss in

hysteretic materials and viscous materials, the equivalent viscous damping C_f is found to be:

$$C_f = \frac{C_f''}{\omega} \quad \text{Eq. 24}$$

$$C_f'' = K_f tan\delta \quad \text{Eq. 25}$$

where $tan\delta$ is the loss tangent which is strongly dependent on the frequency of excitation and the temperature. A rough approximation of $tan\delta$ is to relate with the rebound resilience R as

$$tan\delta = -lnR/\pi \quad \text{Eq. 26}$$

Assume a solution to the motion equation in Eq. 22 as

$$x_2 = X_2 e^{i\omega t} \quad \text{Eq. 27}$$

Therefore

$$\frac{dx_2}{dt} = i\omega x_2 \quad \text{Eq. 28}$$

Combining Eq. 24, Eq. 25, Eq. 27 and Eq. 28 gives the damper force as

$$C_f \frac{dx_2}{dt} = i\, K_f tan\delta\, x_2 \quad \text{Eq. 29}$$

Substituting the expression for the damper force back into the motion equation Eq. 22 and considering the steady-state solution gives the bending deflection δ_f as

$$\delta_f = \frac{F_c}{K_f} \cdot cos^2\delta \quad \text{Eq. 30}$$

An alternative approach to solve for the problem is energy-based. Assuming that both m_2 and m are infinite and stationary and the energy balance becomes

$$\frac{1}{2}m_1V_i^2 = \int_0^{\alpha_{max}} F_c d\alpha + \int_0^{\delta_{fmax}} F_c d\delta_f \quad \text{Eq. 31}$$

Substituting $\alpha_{max} = F_{max}^{5/3}/K_c^{2/3}$ and $\delta_{fmax} = F_{max} \cdot cos^2\delta/K_f$ into Eq. 31 which gives

$$\frac{1}{2}m_1V_i^2 = \frac{2}{5} \cdot \frac{F_{max}^{5/3}}{K_c^{2/3}} + \frac{1}{2}cos^2\delta \cdot \frac{F_{max}^2}{K_f} \quad \text{Eq. 32}$$

It can be observed that the maximum impact force F_{max} is smaller than the integral model due to the energy dissipated by the term of flexural bending. Eq. 32 can be numerically solved to obtain the relationship between the maximum impact force and the dimensions (l and h) of the crack. Furthermore, the impact duration can be obtained based on the derived F_{max} according to Eq. 20. The overall maximum deformation is the superposition of the maximum local contact deformation and maximum bending deformation of the flexural part as $(\alpha_{max} + \delta_{fmax})$, which can be solved respectively based on Eq. 33 and Eq. 30 by substituting F_{max} for F_c.

$$\alpha_{max} = \left(\frac{F_{max}}{K_c}\right)^{2/3} \quad \text{Eq. 33}$$

Similarly as the integral model, the dynamic quantities are associated with material properties of the two colliding bodies and the initial impact velocity. For the defect model, the two dimensional parameters h and l that define the crack are incorporated in the expressions for the dynamic quantities through the bending stiffness K_f. This suggests that these dynamic quantities are correlated with the dimensions of an internal crack. The impact energy is partially dissipated into bending deformation due to the internal crack, which leads to additional energy loss. λ_f is defined to measure the

percentage of the flexural energy loss, which can be estimated from the defect model of contact dynamics as

$$\lambda_f = \frac{U_f}{U_{tot}} = \frac{\int_0^{\delta_{fmax}} F_c d\delta_f}{\frac{1}{2} m_1 V_i^2} = cos^2\delta \cdot \frac{F_{max}^2}{m_1 V_i^2 K_f} \quad \text{Eq. 34}$$

A convenient experimental method to estimate λ_f from the impact acoustic signals is to identify the resonant frequencies and flexural frequencies from the power spectral density (PSD) of impact response, which is further discussed in Chapter 4. It is obvious to tell from Eq. 34 that the crack length and depth play important role in the amount of flexural energy loss, which makes λ_f another promising indicator for identification of internal defects in rubber structure.

3.5 Sensitivity Analysis

3.5.1 Sample Preparation and Material Properties

The material properties of the rubber target and the impactor are to be determined experimentally. It was assumed earlier that the strain in the impact-acoustic is so low which varies in a very small range, thus the rubber material can be treated as a linear material with the low strain area of the stress-strain curve in Figure 10 that $E_2 \cong$ 17.9MPa. The rubber measured in the stress testing is same as the materials used around the belt edges in the tire shoulders.

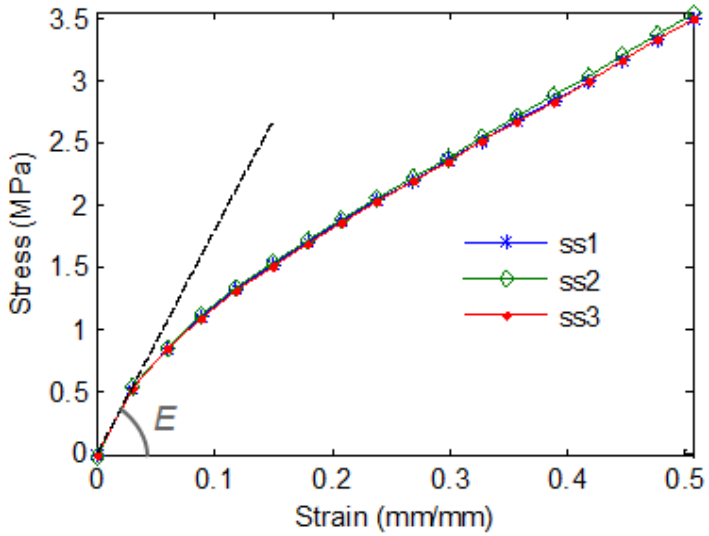

Figure 10: Stress-strain curves measured on the sample rubber composite material

Material properties of the rubber target and the impactor are given in Table 2, and notice the impactor is made of aluminum.

Table 2: Material Properties of Sample Rubber and Aluminum Impactor

	Sample Rubber	**Aluminum**
Density (ρ) kg/m^3	1143	2700
Elastic Modulus (E) MPa	17.9	0.7e5
Poisson's Ratio (ν)	0.49	0.3

The rebound resilience R of the sample rubber material is measured through the rebound test as 0.25, therefore the loss tangent can be calculated from Eq. 26 as

$$tan\delta = -ln0.25/\pi \approx 0.44 \qquad \text{Eq. 35}$$

3.5.2 Sensitivity Analysis of the Integral Model

First, the contact dynamics model for an integral solid structure is further analyzed in order to learn the effect of each influencing factor on the predicted discriminators. The factors considered for sensitivity analysis are: the impact speed (V_i), the impactor's mass (m_1), the target mass (m_2), the impactor's stiffness (E_1), and the target stiffness (E_2). A set of trial parameters in Table 3 is used initially to obtain a baseline scenario. Three discriminators are monitored which are the maximum impact force (F_{max}), impact duration (τ) and maximum contact deformation (α_{max}),

Table 3: Baseline Influencing Factors

	V_i(m/s)	m_1(kg)	m_2(kg)	E_1(Pa)	E_2(Pa)
Baseline	1.85	0.0045	1.6483	70e9	17.9e6

Each variable is multiplied by a factor *N* ranges from 0.1 to 2, and the baseline values correspond to *N=1*. F_{max}, τ and α_{max} are calculated for each influencing factor which is individually varied, see in Table 4 through Table 6. Plots of the three quantities are presented in Figure 11 through Figure 13.

It can be observed directly from the plots that m_2 and E_1 are the two least influencing factors, which only slightly change the three observed discriminators throughout the variations. Both m_2 and E_1 have much greater orders of magnitude than m_1 and E_2, which yield negligible terms while taking their inverse to derive the contact mass M and contact stiffness K_c.

Table 4: Values of F_{max} derived for each factor individually varied from integral model

Maximum Impact Force F_{max} (N)					
Factors / N*Baseline	V_i	m_1	m_2	E_1	E_2
0.1	2.1546634	7.4454159	32.963587	34.111551	13.596505
0.2	4.9501166	11.788598	33.48798	34.132401	17.940477
0.3	8.0523925	15.419186	33.709185	34.139361	21.09916
0.4	11.372382	18.651379	33.839152	34.142843	23.672021
0.5	14.864265	21.615561	33.927569	34.144933	25.881773
0.6	18.49954	24.381786	33.99295	34.146326	27.839486
0.7	22.258561	26.993182	34.043975	34.147321	29.609741
0.8	26.126872	29.478682	34.085325	34.148068	31.233889
0.9	30.093344	31.858884	34.119781	34.148649	32.740232
1	34.149113	34.149113	34.149113	34.149113	34.149113
1.1	38.28694	36.36116	34.17451	34.149494	35.475718
1.2	42.500783	38.504342	34.196802	34.14981	36.731723
1.3	46.785519	40.586184	34.216594	34.150078	37.92633
1.4	51.136744	42.612875	34.234336	34.150308	39.066938
1.5	55.550624	44.589584	34.250368	34.150507	40.159597
1.6	60.02379	46.52068	34.264959	34.150682	41.209327
1.7	64.553254	48.409905	34.278319	34.150835	42.220345
1.8	69.136349	50.26049	34.290619	34.150972	43.196235
1.9	73.770674	52.07525	34.301996	34.151094	44.14007
2	78.454061	53.856658	34.312564	34.151204	45.054509

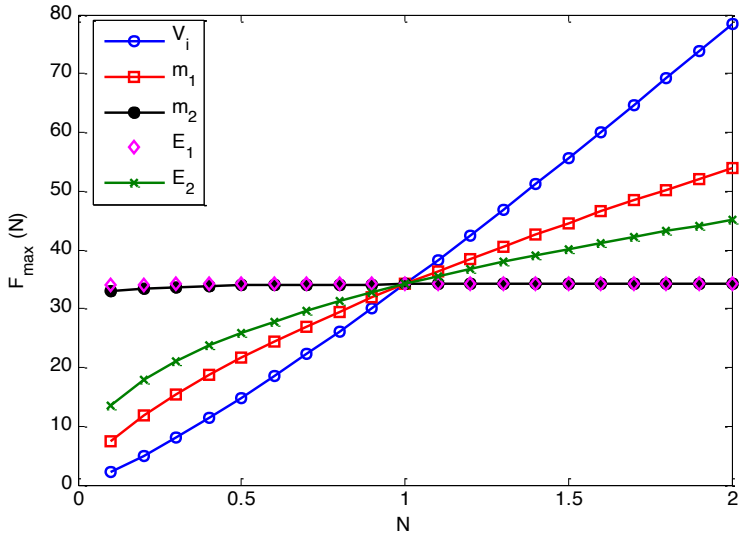

Figure 11: Integral model sensitivity of influencing factors on maximum impact force F_{max}

Table 5: Values of τ derived for each factor individually varied from integral model

Impact Duration τ (msec)					
Factors / N*Baseline	V_i	m_1	m_2	E_1	E_2
0.1	1.2138211	0.3512733	0.7934136	0.7667127	1.9235648
0.2	1.0566926	0.4437128	0.7809895	0.7662443	1.4578073
0.3	0.9743846	0.5088548	0.7758645	0.7660881	1.239564
0.4	0.9199044	0.5608971	0.7728846	0.76601	1.1048384
0.5	0.8797528	0.6049752	0.7708704	0.7659631	1.0105088
0.6	0.8482511	0.6436057	0.7693877	0.7659319	0.9394484
0.7	0.8224984	0.6782317	0.7682346	0.7659095	0.8832823
0.8	0.8008233	0.7097674	0.7673026	0.7658928	0.837352
0.9	0.7821791	0.7388326	0.7665277	0.7658798	0.7988263
1	0.7658693	0.7658693	0.7658693	0.7658693	0.7658693
1.1	0.7514086	0.7912051	0.7653002	0.7658608	0.7372299
1.2	0.7384455	0.8150902	0.7648013	0.7658537	0.712021
1.3	0.7267182	0.8377207	0.7643589	0.7658477	0.6895937
1.4	0.7160265	0.8592535	0.7639628	0.7658425	0.6694602
1.5	0.7062142	0.8798162	0.7636052	0.7658381	0.6512455
1.6	0.6971571	0.8995142	0.76328	0.7658342	0.6346563
1.7	0.6887552	0.9184358	0.7629825	0.7658307	0.6194587
1.8	0.6809264	0.9366555	0.7627089	0.7658277	0.6054639
1.9	0.6736029	0.9542372	0.7624559	0.7658249	0.5925174
2	0.666728	0.9712359	0.762221	0.7658224	0.5804915

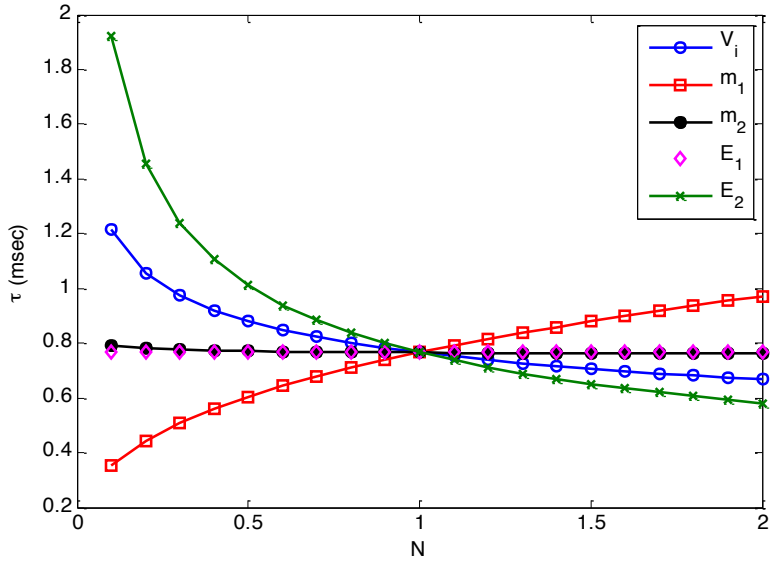

Figure 12: Integral model sensitivity of influencing factors on impact duration τ

Table 6: Values of α_{max} derived for each factor individually varied from integral model

Maximum Contact Deformation α_{max} (mm)					
Factors / N*Baseline	V_i	m_1	m_2	E_1	E_2
0.1	0.0891051	0.2584988	0.5685042	0.5628342	1.4120648
0.2	0.155141	0.326435	0.567138	0.5624904	1.0701581
0.3	0.2145851	0.3742573	0.5659569	0.5623757	0.9099484
0.4	0.2701161	0.4124212	0.5650572	0.5623183	0.811048
0.5	0.3229078	0.4447101	0.5643498	0.5622839	0.7418018
0.6	0.3736143	0.4729779	0.5637746	0.562261	0.6896373
0.7	0.42265	0.4982884	0.5632941	0.5622446	0.6484064
0.8	0.4702995	0.5213152	0.5628841	0.5622323	0.6146896
0.9	0.5167691	0.5425155	0.5625282	0.5622227	0.5864084
1	0.5622151	0.5622151	0.5622151	0.5622151	0.5622151
1.1	0.6067596	0.5806556	0.5619364	0.5622088	0.5411912
1.2	0.6505003	0.5980218	0.5616859	0.5622036	0.5226857
1.3	0.6935171	0.6144584	0.5614591	0.5621992	0.5062221
1.4	0.7358765	0.630081	0.5612521	0.5621954	0.4914423
1.5	0.7776345	0.644984	0.5610622	0.5621921	0.4780712
1.6	0.8188389	0.6592452	0.560887	0.5621893	0.4658932
1.7	0.8595312	0.6729297	0.5607245	0.5621867	0.4547368
1.8	0.8997472	0.6860927	0.5605734	0.5621845	0.4444634
1.9	0.9395186	0.6987813	0.5604321	0.5621825	0.4349596
2	0.9788733	0.7110361	0.5602997	0.5621807	0.4261315

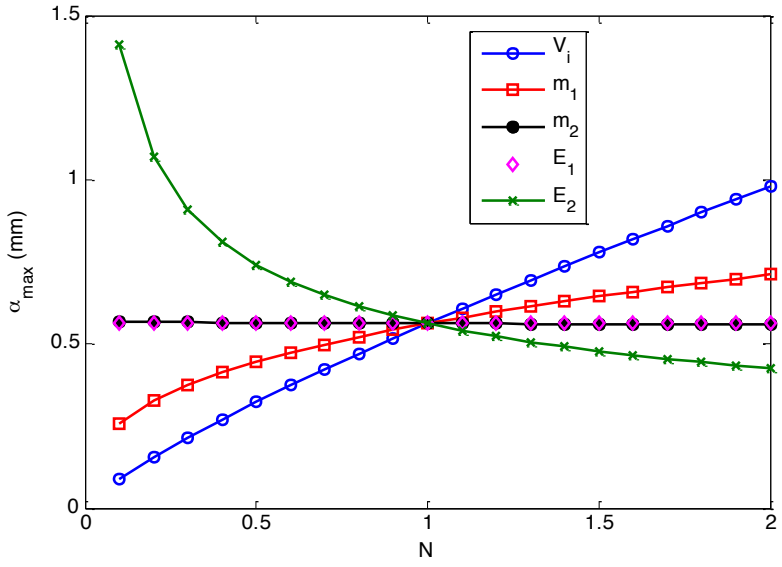

Figure 13: Integral model sensitivity of influencing factors on maximum contact deformation α_{max}

More significantly, the sensitivity analysis of m_2 on the impact dynamics discriminators provide theoretical basis for model approximation used to simplify the shape of tire casing. The assumption made for the defect model that the target mass can be treated as infinite and stationary is valid. One major prerequisite to simplify the model approximating a section of tire casing into a cubic rubber block as shown in Figure 14 is to assume that the applied impact only affects the mechanical dynamics within a limited

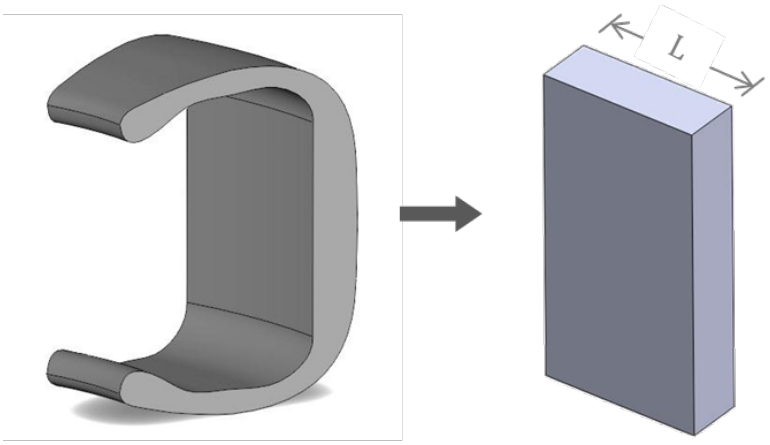

Figure 14: Model approximation of tire section

local area of materials around the contact region. Based on the fact that m_2 has much higher order of magnitude than m_1, along with the prerequisite assumption about local effects, the two sidewalls were eliminated in the simplified model. Since the mass of the rubber block m_2 is much greater than that of the impactor's, the error introduced by the approximation in m_2 can be neglected. The curvature of the tread was deemed as zero for a small curved segment considering that the boundary contours have minor effect on impact response. The vertical height of the cube simulates the shoulder to shoulder distance, and the horizontal thickness corresponds to the distance from tread surface to

inner carcass. The effect of the lateral length L of the cubic rubber block will be further studied through experimental investigations.

The impact velocity V_i, the mass of the impactor m_1 and the stiffness of the target structure E_2 are all influential factors on the discriminators. All the monitored dynamic quantities are very sensitive to the variation in V_i. This relationship suggests that to guarantee a stably constant V_i is crucial throughout impact tests for the purpose of defect identification, so that the fluctuations introduced by variations in V_i can be mitigated as much as possible.

Moreover, the mass of the impactor m_1 influences the discriminators much more dominantly than the target mass m_2. This observed conclusion can be further exploited to acquire the sensitivities of the curvatures of the colliding bodies, or the contact radii r_1 and r_2. According to the relationship between the colliding bodies' masses m_1, m_2 and the equivalent contact radii r_1, r_2 by Eq. 11, it can be concluded that the curvature of the target surface affects the discriminators much less than the curvature of the impactor surface does. The sensitivity study of the target surface radius r_2 yields instructive conclusion on how the tire surface curvature affects the impact responses. The surface curvature of the tire shoulder can thus be deemed as zero, which is equivalent to a flat surface perpendicular to the applied impact. Alternatively, the sensitivity plots show that the impactors' radius r_1 relating to the impactor's mass m_1 has a great influence on all the three discriminators. The effects of the impact velocity V_i and impactor's radius r_1 on the impact duration τ will in turn be reflected on the frequency features of the impact

responses, which is decisive for the frequency domain analysis of the impact acoustic signal (discussed in Chapter 4).

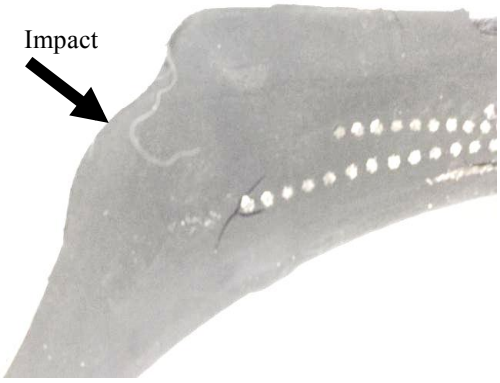

Figure 15: Cross sectional view of the crack around belt edges

Another dominant factor on the impact acoustic discriminators is the elastic modulus of the target E_2, which can be observed from Figure 11 to Figure 13. In the case of a tire casing structure, E_2 is influenced by various facts such as embedded steel belts, quality of uniformity, foreign inclusions etc. Considering the prerequisite for the impact acoustic method, which assumes that the impact induced stresses only take effect in a limited region around the contact area, the far-field reinforcements such as steel belts provide little changes to the impact responses. The most significant factor that changes the target stiffness is considered as attributed to lateral cracks located around the belt edges as shown in Figure 15. As a result, the variations observed in the dynamic quantities can be due to the existence of embedded cracks while the other two influential factors V_i and m_1 are maintained stable throughout the tests, which provide indication of structural integrity. To simplify the experimental study, approximation of the sectional

tire structure as discussed earlier can also involve further simplification of material properties, which assume the shoulder areas where the impact is applied are homogeneously consisted of rubber compound without any reinforcements.

3.5.3 Sensitivity Analysis of the Defect Model

The corresponding defect model has incorporated two additional parameters h and l which define the geometry and location of the internal crack. The effects of varying these parameters on impact dynamic responses need to be understood in terms of F_{max}, τ, $(\alpha_{max} + \delta_{fmax})$ and the flexural energy loss λ_f. Baseline values of the evaluated factors are given in Table 7, and the four impact dynamic discriminators are calculated for each individually varied influencing factor listed from Table 8 to Table 11.

Table 7: Baseline Influencing Factors and Dimensions of Crack

	V_i(m/s)	m_1(kg)	m_2(kg)	E_1(Pa)	E_2(Pa)	h (mm)	l (mm)
Baseline	1.85	0.0045	1.6483	70e9	17.9e6	25.4	25.4

Sensitivity analysis of the first five factors considered for the defect model yields similar conclusions as integral model. The two least influential factors m_2 and E_1 can be eliminated in the sensitivity plots to make the charts more legible. The figures provide clear comparison between the defect parameters and the other five factors. It was assumed previously that variations in the target stiffness E_2 are attributed to the existence of crack, which can therefore be related to the two defect parameters h and l. It can be

seen that increase in crack depth h and decrease in crack length l are both equivalent to increase in E_2, the elastic modulus of the target structure. To compare the sensitivity between the two defect parameters, it can be observed from the plots that the effect of the depth of crack h is much more dominant than the effect of the length of crack l for $\mathrm{N} = 0\sim1$ (equivalent to $h = 0\sim25.4mm$, $l = 0\sim25.4mm$). However, when $\mathrm{N} = 1\sim2$ (eq. to $h = 25.4mm\sim50.8mm$, $l = 25.4mm\sim50.8mm$) the two parameters have comparatively subtle influences on the observed quantities. This trend implies a sensitive range for the discriminators to sense the existence of crack, and this will be further discussed in details afterwards. Also the crack length l is shown less significant compared to all the other plotted factors for the first three dynamic quantities F_{max}, τ, $(\alpha_{max} + \delta_{fmax})$ as shown in Figure 16, Figure 17, and Figure 18. However, the flexural energy loss percentage λ_f presents much higher sensitivity to variation in both the crack depth h and the crack length l. It can be read from Table 11 that λ_f increases about 4.6% by doubling the crack length l, which is much higher compared to 0.74% by doubling the impact velocity V_i. Due to this significant difference in the variation range between the first five parameters $(V_i, m_1, m_2, E_1, E_2)$ and the two defect parameters (h, l), the sensitivity plots were separated in Figure 19 and Figure 20. λ_f is approaching the maximum value one as the crack is getting closer to the impacted surface, and decreases rapidly as the crack goes deeper. Alternatively with the increase in the crack length, λ_f arises at a relatively stable rate reflecting more energy lost due to flexural vibrations induced by the growing crack.

Table 8: Values of F_{max} derived for each factor individually varied from defect model

Maximum Impact Force F_{max} (N)							
Factors / N*Baseline	V_i	m_1	m_2	E_1	E_2	h	l
0.1	2.1419536	7.3932016	32.503623	33.61455	13.286167	6.6127609	34.143878
0.2	4.9117079	11.685247	33.012323	33.634503	17.582262	16.284706	34.128469
0.3	7.9790776	15.265281	33.226317	33.641163	20.709702	23.845762	34.102933
0.4	11.256425	18.447355	33.351842	33.644495	23.258809	28.319637	34.067344
0.5	14.698815	21.361775	33.43714	33.646495	25.449174	30.724168	34.021808
0.6	18.278357	24.078543	33.500161	33.647828	27.390393	32.024235	33.966457
0.7	21.975864	26.640751	33.549312	33.648781	29.146229	32.759178	33.901452
0.8	25.777242	29.077305	33.589122	33.649495	30.757524	33.197063	33.82698
0.9	29.671658	31.408784	33.62228	33.650051	32.252244	33.47121	33.74325
1	33.650495	33.650495	33.650495	33.650495	33.650495	33.650495	33.650495
1.1	37.706724	35.814214	33.674917	33.650859	34.96729	33.77223	33.574732
1.2	41.834488	37.909248	33.696348	33.651162	36.214177	33.857592	33.494096
1.3	46.028826	39.943111	33.71537	33.651419	37.400257	33.919129	33.40871
1.4	50.285476	41.921983	33.732417	33.651639	38.532849	33.964563	33.3187
1.5	54.600733	43.851025	33.747819	33.651829	39.617939	33.998815	33.224198
1.6	58.971344	45.734602	33.761833	33.651996	40.660495	34.025112	33.125338
1.7	63.394429	47.576447	33.774664	33.652143	41.664691	34.045628	33.022261
1.8	67.867417	49.379786	33.786473	33.652274	42.634073	34.061866	32.915108
1.9	72.387998	51.14743	33.797396	33.652391	43.571685	34.074882	32.804023
2	76.954083	52.881847	33.807541	33.652496	44.480159	34.085437	32.689154

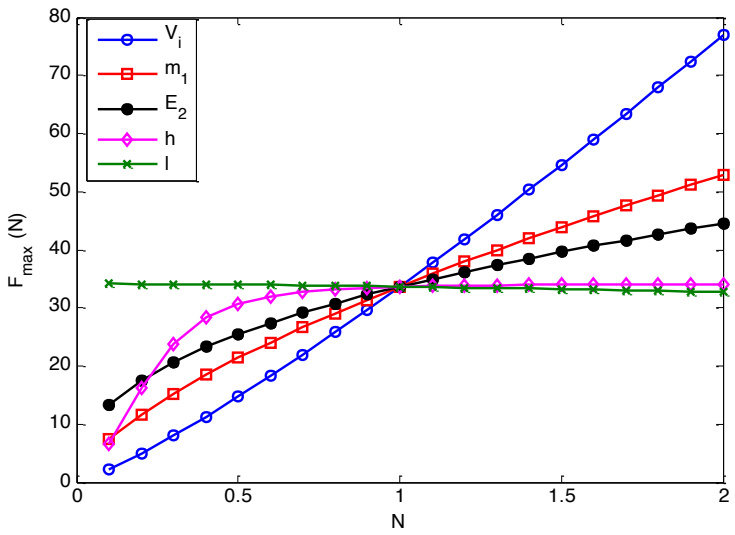

Figure 16: Defect model sensitivity of influencing factors on maximum impact force F_{max}

Table 9: Values of τ derived for each factor individually varied from defect model

Impact Duration τ (msec)							
Factors / N*Baseline	V_i	m_1	m_2	E_1	E_2	h	l
0.1	1.2210236	0.3537542	0.8046413	0.7780488	1.9684954	3.955044	0.765987
0.2	1.0649558	0.4476373	0.7922423	0.7775872	1.4875082	1.606032	0.766333
0.3	0.9833377	0.5139851	0.7871399	0.7774333	1.2628747	1.096789	0.766906
0.4	0.9293807	0.5671005	0.7841773	0.7773563	1.1244668	0.92352	0.767708
0.5	0.8896554	0.6121626	0.7821769	0.7773101	1.027686	0.851244	0.768735
0.6	0.8585157	0.6517112	0.7807055	0.7772793	0.9548515	0.816686	0.769988
0.7	0.833079	0.687204	0.7795617	0.7772573	0.8973291	0.798364	0.771464
0.8	0.8116852	0.7195649	0.7786378	0.7772408	0.8503207	0.787834	0.773163
0.9	0.7932952	0.7494204	0.7778699	0.7772279	0.8109128	0.781381	0.775081
1	0.7772177	0.7772177	0.7772177	0.7772177	0.7772177	0.777218	0.777218
1.1	0.7629709	0.8032882	0.776654	0.7772092	0.7479493	0.774416	0.778971
1.2	0.7502066	0.8278853	0.77616	0.7772022	0.7221967	0.772464	0.780847
1.3	0.7386651	0.8512078	0.7757221	0.7771963	0.6992936	0.771062	0.782843
1.4	0.7281479	0.8734144	0.7753301	0.7771912	0.6787393	0.770031	0.784957
1.5	0.7185002	0.8946345	0.7749763	0.7771868	0.6601494	0.769255	0.78719
1.6	0.7095991	0.9149749	0.7746546	0.777183	0.6432228	0.76866	0.789539
1.7	0.7013454	0.9345252	0.7743603	0.7771796	0.62772	0.768197	0.792004
1.8	0.6936578	0.9533611	0.7740896	0.7771766	0.6134473	0.767831	0.794582
1.9	0.6864693	0.9715472	0.7738395	0.7771739	0.6002467	0.767538	0.797273
2	0.6797237	0.9891394	0.7736073	0.7771714	0.5879871	0.7673	0.800074

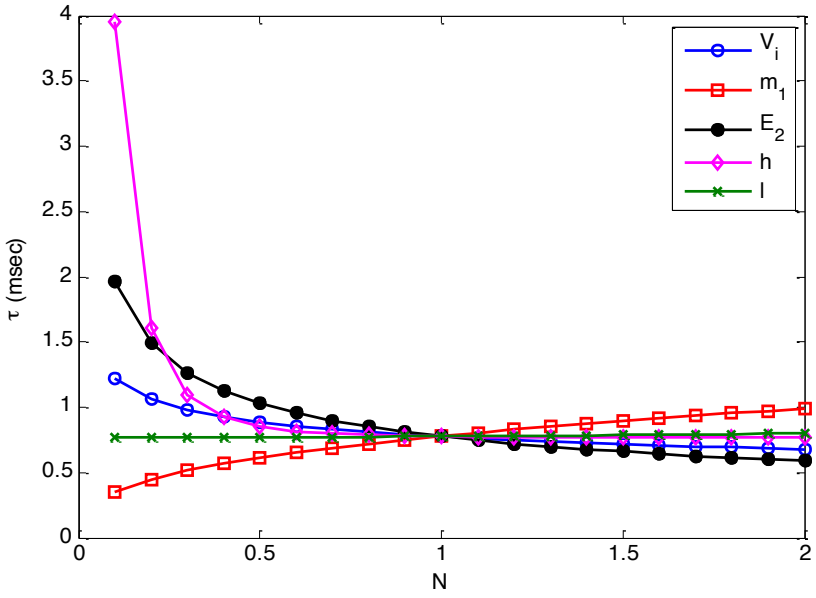

Figure 17: Defect model sensitivity of influencing factors on impact duration τ

Table 10: Values of $\alpha_{max}+\delta_{fmax}$ derived for each factor individually varied from defect model

Maximum Deformation $\alpha_{max}+\delta_{fmax}$ (mm)							
Factors / N*Baseline	V_i	m_1	m_2	E_1	E_2	h	l
0.1	0.0895949	0.2601902	0.575959	0.5705455	1.4426353	2.783273	0.5622949
0.2	0.156265	0.32911	0.5747101	0.5702063	1.0903648	1.1420056	0.5625301
0.3	0.2164119	0.3777533	0.5735784	0.5700931	0.925807	0.7891019	0.5629203
0.4	0.2726943	0.4166476	0.5727077	0.5700366	0.8244011	0.6699098	0.5634651
0.5	0.3262755	0.4496056	0.57202	0.5700026	0.7534872	0.6204243	0.564164
0.6	0.3778034	0.4784974	0.5714594	0.56998	0.7001156	0.5968272	0.565016
0.7	0.427688	0.5043965	0.5709903	0.5699638	0.657962	0.584335	0.5660203
0.8	0.4762103	0.5279833	0.5705895	0.5699517	0.6235116	0.5771614	0.5671757
0.9	0.5235745	0.5497196	0.5702413	0.5699422	0.5946302	0.5727681	0.568481
1	0.5699347	0.5699347	0.5699347	0.5699347	0.5699347	0.5699347	0.5699347
1.1	0.6154115	0.5888729	0.5696616	0.5699285	0.548483	0.5680284	0.5711283
1.2	0.6601011	0.6067211	0.5694162	0.5699234	0.5296076	0.5667001	0.5724047
1.3	0.7040824	0.6236257	0.5691937	0.569919	0.5128202	0.5657468	0.5737632
1.4	0.7474208	0.6397038	0.5689907	0.5699153	0.4977542	0.5650452	0.575203
1.5	0.7901716	0.6550509	0.5688043	0.5699121	0.4841278	0.5645175	0.5767232
1.6	0.8323817	0.6697457	0.5686324	0.5699092	0.4717204	0.5641132	0.5783231
1.7	0.8740919	0.6838544	0.5684729	0.5699067	0.4603563	0.5637982	0.5800017
1.8	0.9153376	0.6974327	0.5683245	0.5699045	0.4498939	0.5635491	0.5817581
1.9	0.9561498	0.7105285	0.5681857	0.5699025	0.4402171	0.5633496	0.5835913
2	0.996556	0.723183	0.5680557	0.5699007	0.4312301	0.563188	0.5855004

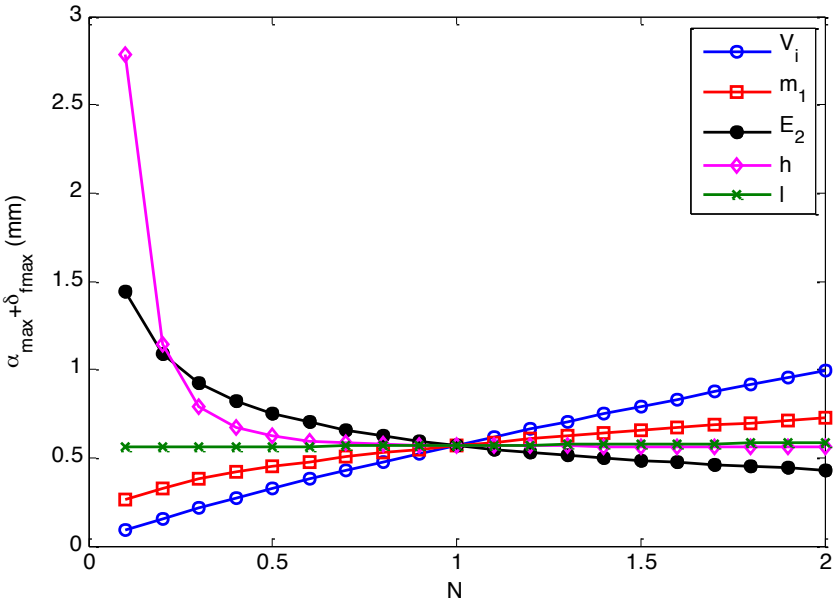

Figure 18: Defect model sensitivity of influencing factors on maximum contact deformation $\alpha_{max}+\delta_{fmax}$

Table 11: Values of λ_f derived for each factor individually varied from defect model

Flexural Energy Loss λ_f							
Factors / N*Baseline	V_i	m_1	m_2	E_1	E_2	h	l
0.1	0.979%	1.166%	2.253%	2.410%	3.765%	93.264%	0.025%
0.2	1.286%	1.456%	2.324%	2.413%	3.297%	70.700%	0.100%
0.3	1.509%	1.657%	2.355%	2.414%	3.049%	44.917%	0.225%
0.4	1.689%	1.814%	2.372%	2.414%	2.884%	26.727%	0.398%
0.5	1.843%	1.946%	2.385%	2.415%	2.763%	16.106%	0.619%
0.6	1.979%	2.061%	2.394%	2.415%	2.667%	10.126%	0.887%
0.7	2.102%	2.162%	2.401%	2.415%	2.588%	6.673%	1.203%
0.8	2.214%	2.254%	2.406%	2.415%	2.522%	4.591%	1.563%
0.9	2.318%	2.338%	2.411%	2.415%	2.465%	3.278%	1.968%
1	2.415%	2.415%	2.415%	2.415%	2.415%	2.415%	2.415%
1.1	2.506%	2.487%	2.419%	2.415%	2.371%	1.828%	2.780%
1.2	2.592%	2.554%	2.422%	2.415%	2.331%	1.415%	3.168%
1.3	2.674%	2.618%	2.424%	2.415%	2.295%	1.117%	3.578%
1.4	2.752%	2.677%	2.427%	2.415%	2.262%	0.897%	4.009%
1.5	2.826%	2.734%	2.429%	2.415%	2.232%	0.730%	4.461%
1.6	2.897%	2.788%	2.431%	2.415%	2.204%	0.603%	4.933%
1.7	2.966%	2.840%	2.433%	2.415%	2.178%	0.503%	5.424%
1.8	3.032%	2.889%	2.435%	2.415%	2.154%	0.424%	5.934%
1.9	3.096%	2.937%	2.436%	2.415%	2.131%	0.361%	6.461%
2	3.158%	2.982%	2.438%	2.415%	2.110%	0.310%	7.004%

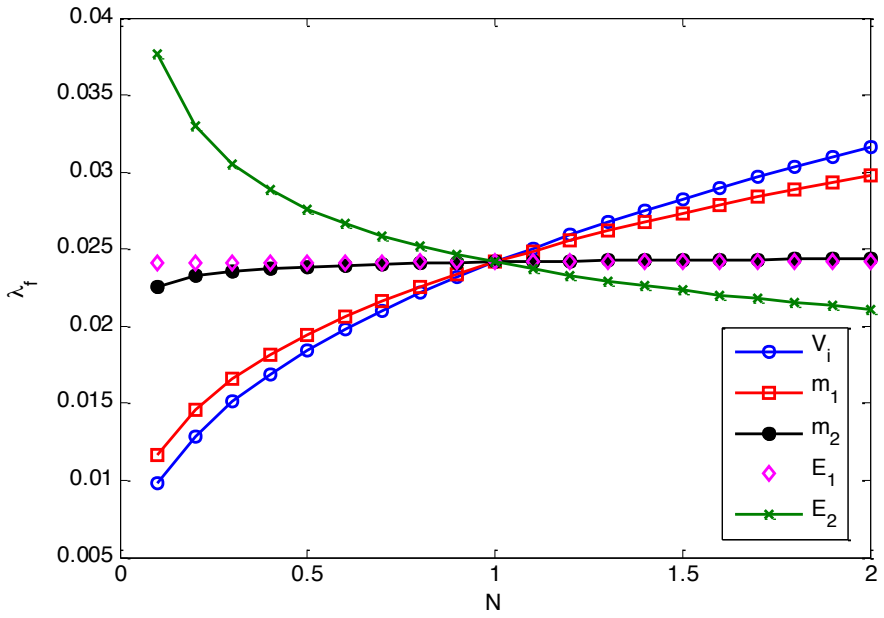

Figure 19: Defect model sensitivity of influencing factors on flexural energy loss λ_f

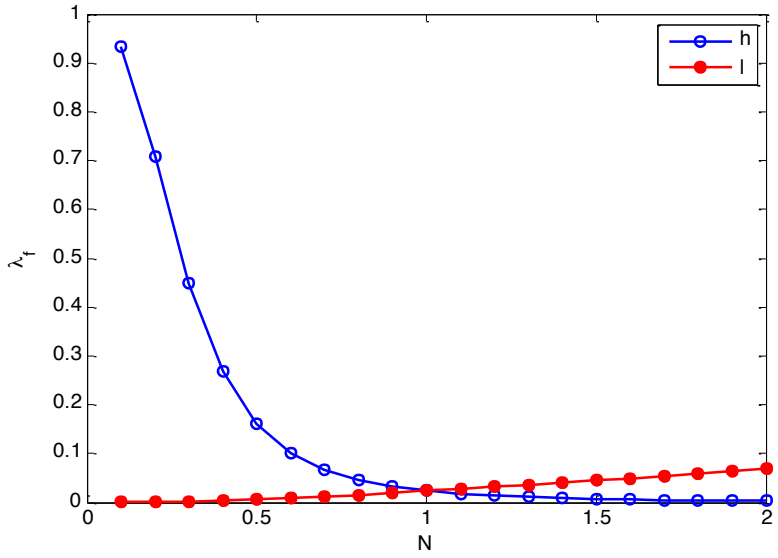

Figure 20: Crack dimensional quantities sensitivity analysis on flexural energy loss λ_f

To briefly conclude on the sensitivity analysis for the defect model, the four dynamic quantities F_{max}, τ, $(\alpha_{max} + \delta_{fmax})$ and λ_f were proved sensitive to depths of crack within a limited range. Therefore, these quantities can be used as defect discriminators. The sensitive range or detectable range can be roughly determined as 0 to 25.4mm for the crack depth. All the four discriminators are not as sensitive to the crack length l as to the crack depth h, extremely for the first three dynamic quantities. Comparatively the crack length l influences λ_f more dominantly than the other parameters besides crack depth h. From Figure 20, it can be seen that λ_f is approaching 1 when the crack gets closer to the impacted surface. In the case of very shallow crack, the materials above it is like a very thin membrane, and most of the impact energy is transformed into flexural vibrations. So if the flexural vibration energy can be distinguished from the resonant energy in the experimentally measured impact acoustic

signal, the ratio of these two energies is identical measurement of the theoretical dynamic quantity λ_f. The sensitivity results state that it is reliable to adopt λ_f as an indicator to identify lengths of crack for further development of the impact acoustic method for the purpose of defect quantification. In this thesis, discussion of the impact acoustic NDT method is only focused on defect localization.

4 IMPACT ACOUSTIC SIGNAL ANALYSIS

4.1 Introduction

The impact acoustic signal discussed in this thesis includes two parts: one is the impact force signal which can be measured by using a load cell as the impact tip; another is the resultant acoustic signal recorded from microphone. According to the contact dynamics model, the dynamic quantities are verified as sensitive to the existence of internal crack in a rubber structure. The focus in this chapter will be placed on targeting the corresponding discriminators that can be extracted from the impact acoustic signals.

4.2 Analysis of Impact Force Signal

4.2.1 Theoretical Analysis of Impact Force Signal

The experimental impact force signal provides direct measurements of peak impact force and impact duration. These two quantities can be theoretically derived from the contact dynamics model. It is necessary to compare the experimental and theoretical derived quantities in order to validate the model. Also, the effects of crack on the quantities are to be analyzed to verify the rationality of adopting these two quantities as defect discriminators. First, theoretical analysis was performed in order to learn the effect of internal crack on these two dynamic quantities.

Rubber samples are prepared with regular cubic shape and made of rubber with material properties as listed previously in Table 2. Two sets of block dimensions were used: 50.8mm×279.4mm×101.6mm and 50.8mm×279.4mm×152.4mm, to study the effects of block length on the impact dynamics quantities. They are referred as 101.6mm block and 152.4mm block for convenience in this thesis. Four samples of each dimension were fabricated, which are one integral block and three defective blocks with artificial cut-through cracks on both ends, as shown in Figure 21.

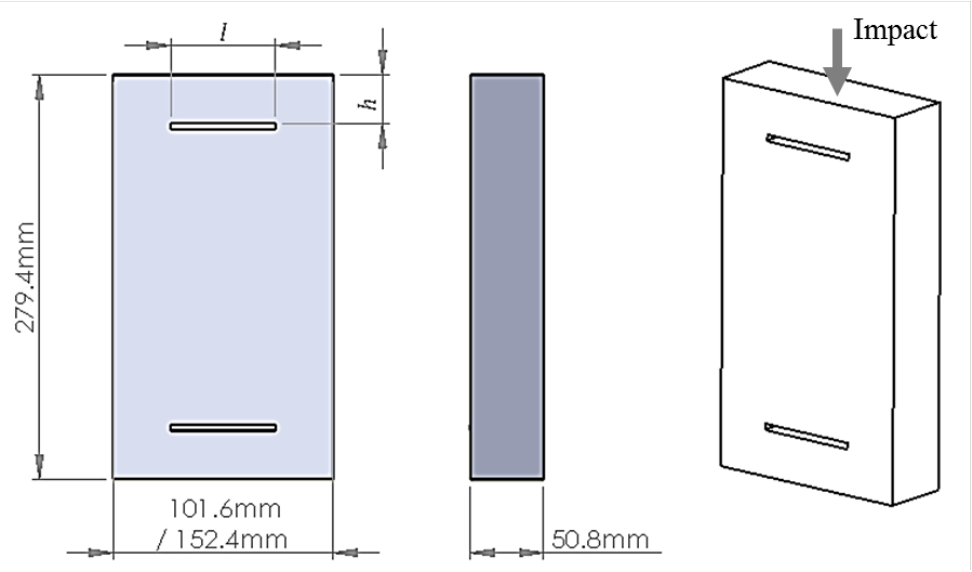

Figure 21: Sample rubber block with artifical cut-through cracks

Given three different crack depths h as 25.4mm, 19.05mm, 12.7mm and two crack length l of 25.4mm and 50.8mm, three defective blocks with two cut-through cracks on each of them, enumerate six combinations of the crack dimensions h and l. The closest distance between the top and bottom cracks is 228.6mm, which is obtained by deducting two crack depths of h =25.4mm from the overall height of the block. It was

proved previously that impact dynamics discriminators become very insensitive to crack deeper than 25.4mm, and correspondingly it can be assumed that far-field variations (such as another crack located at 228.6mm away from the affected zone of the applied impact) can be ignored.

Theoretical values of peak impact force F_{max} and impact duration τ are calculated based upon the developed integral model and the defect model, for four scenarios in 101.6mm rubber block. F_{max} and τ were plot against the impact velocities respectively in Figure 22 and Figure 23, which were also compared among integral and three different crack depths with $l = 25.4mm$. At higher velocities, the model predicts higher impact force and lower impact duration for each scenario. For a certain impact velocity, the integral block (curve 1) gives higher impact force and lower impact duration than

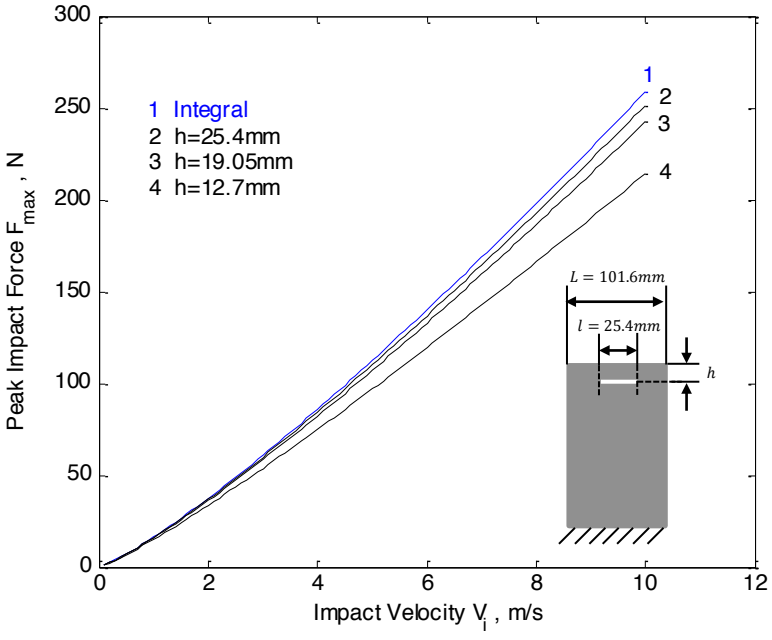

Figure 22: Theoretical peak impact force versus impact velocity for one integral and three defective rubber blocks with different depths of embedded crack

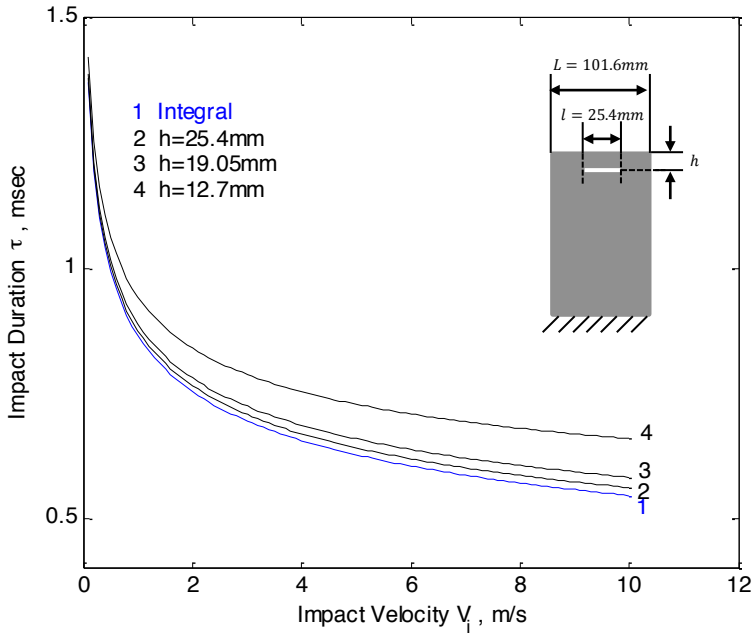

Figure 23: Theoretical impact duration versus impact velocity for one integral and three defective rubber blocks with different depths of embedded crack

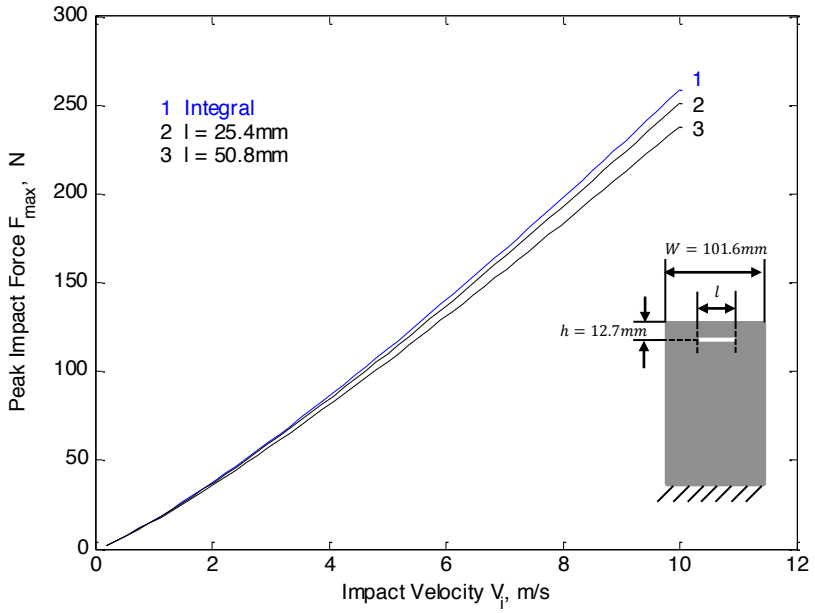

Figure 24: Theoretical peak impact force versus impact velocity for one integral and two defective rubber blocks with different lengths of embedded crack

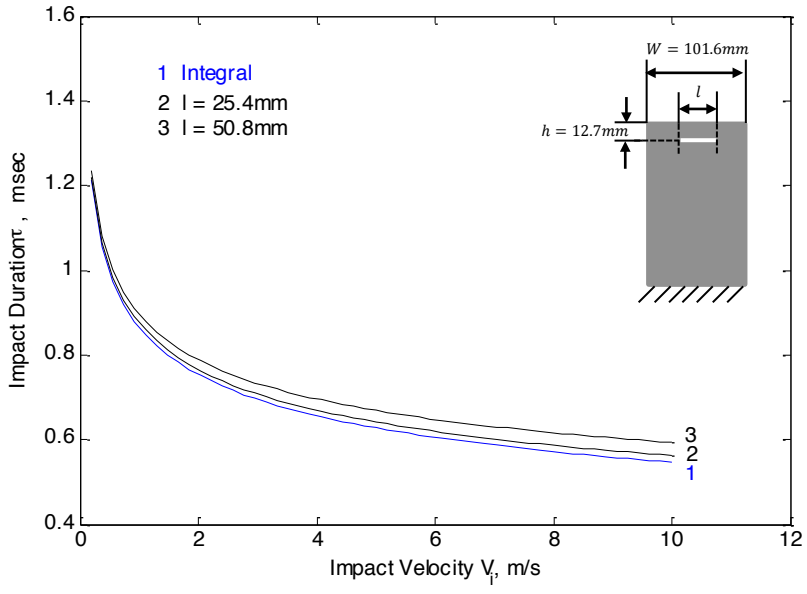

Figure 25: Theoretical impact duration versus impact velocity for one integral and two defective rubber blocks with different lengths of embedded crack

defective blocks (curve 2,3,4), which is associated with additional membrane bending deflection introduced by the embedded crack other than local contact deformation. It can also be observed that the peak impact force arises while the impact duration decreases with growing depth of embedded crack, by approaching the predicted value for the integral model. The trend shows that the deeper the crack is located, the less effect the existence of crack has on the predicted discriminators, which validated the rationality of fabricating two cracks in a single block for simulating the two shoulders in a tire casing.

Figure 24 and Figure 25 show the varying tendency of peak impact force and impact duration resulted by impact velocity for three scenarios, which are the 101.6mm integral block and two defective 101.6mm blocks with crack length of 25.4mm and 50.8mm at a same depth as 12.7mm. For a given impact velocity, the defective blocks

present lower impact force and longer impact duration than the integral block; the narrower the crack is, the less difference there is in the two discriminators between the integral and defective cases. It is straightforward that a defective block with crack length infinitely approaching zero is identical to an integral block. It can be inferred simultaneously that the impact dynamics discriminators can be incapable of detecting cracks which are too small in size. Therefore the capability of the impact dynamic quantities in defect inspection relies on the sensitivity and detectable range of the sensors. This adds tradeoff between economical consideration and requirements for inspection accuracy. The targeted belt edge defect in the tire shoulder as discussed in this these is always less than 25.4mm, which means current discriminators can identify the belt edge separations that are commonly found in a tire.

Another significant value of studying the effect of impact velocity on the force and duration of impact is to determine the practical range of the impact velocity. The upper bound of the impact velocity can be determined by the measuring range of the force sensor, which for instance should be lower than 8m/s for the scenarios in Figure 22 if the maximum scale of the force sensor is 200N. The lower bound can partially be related to the frequency coverage of the impact generated acoustic signal, which is approximately the inverse of the impact duration, and this topic is further discussed in Chapter 4. Short impact duration assures sufficient frequency coverage allowing useful range of frequency spectral information provided, which alternatively implies that a minimal impact velocity is important to guarantee sufficiently short impact duration.

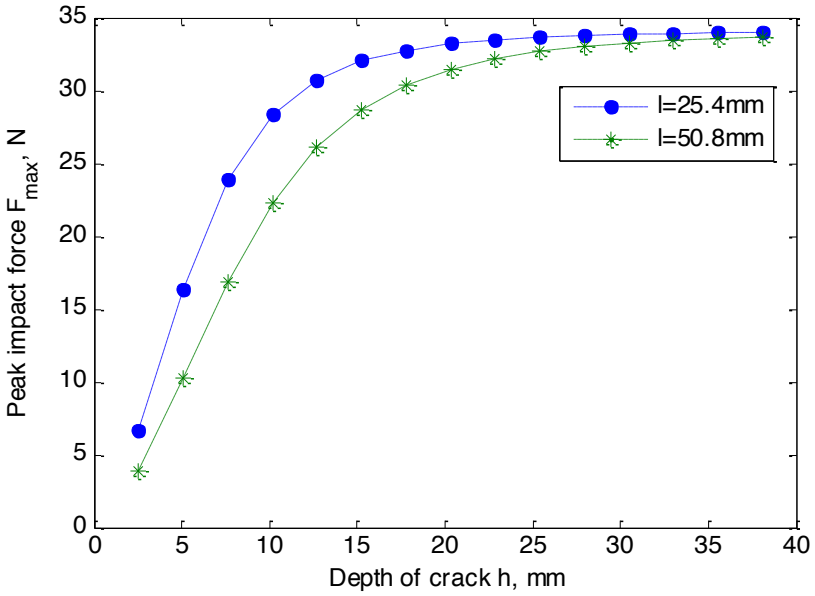

Figure 26: Predicted peak impact force versus depth of crack by defect model

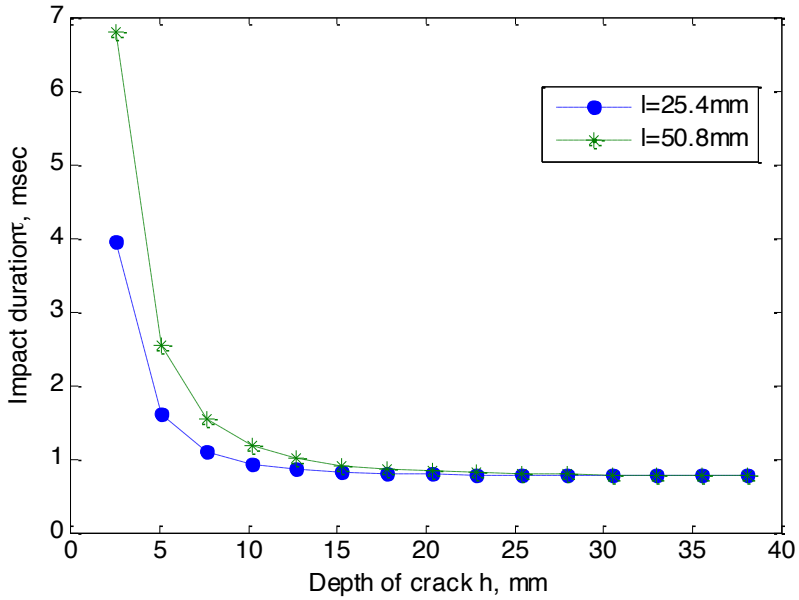

Figure 27: Predicted impact duration versus depth of crack by defect model

In Figure 26 and Figure 27, F_{max} and τ are theoretically derived for 101.6mm defective blocks with crack of various depths, considering an impact velocity at 1.85m/s. Two scenarios are compared between crack with length of $25.4mm$ and $50.8mm$. For shallower cracks at depth less than $25mm$, the impact force increases much more rapidly with the increase in the depth of crack than for deeper cracks. The phenomenon indicates that the impact force can be a very sensitive discriminator for cracks close to the impacted surface, but be more difficult to distinguish cracks at different depths when they are deeper in the structure, especially when the measuring sensitivity of the force sensor is not sufficiently high. Considering the current scenario, it can also be summarized that when the crack is located deeper than $25mm$, the crack can hardly be seen by looking for change in the measured peak impact force. However, sensitive region of the impact duration judging from Figure 27 is even smaller, which is limited to cracks of length below $15mm$. There are two designated crack depths fabricated in the sample rubber blocks (19.05mm and 25.4mm) fallen out of the sensitive range of the impact duration, but still within that of the peak impact force. It can be predicted that differences in the measured impact durations are very small or even imperceptible. However, the peak impact force can be used as discriminator to differentiate the two depths.

4.2.2 Experimental Validation of Impact Force Discriminators

Both the integral and the defect contact dynamics model were validated by experimental impact force measurements on the fabricated rubber block samples depicted

previously. Generally there are two sets of impact tests on the integral block (both top and bottom) and six measurements of cracks from the defective ones in 101.6mm block and 152.4mm block respectively.

Figure 28 compares the peak impact force F_{max} which is theoretically predicted and experimentally obtained. It shows very good coherence between the predicted and experimental F_{max}, where all the plotted points in the figure fall within the 5% error margins. The good correlation makes possible the prediction of impact force measured from rubber composite structure, and defect identification based upon the measured peak impact force.

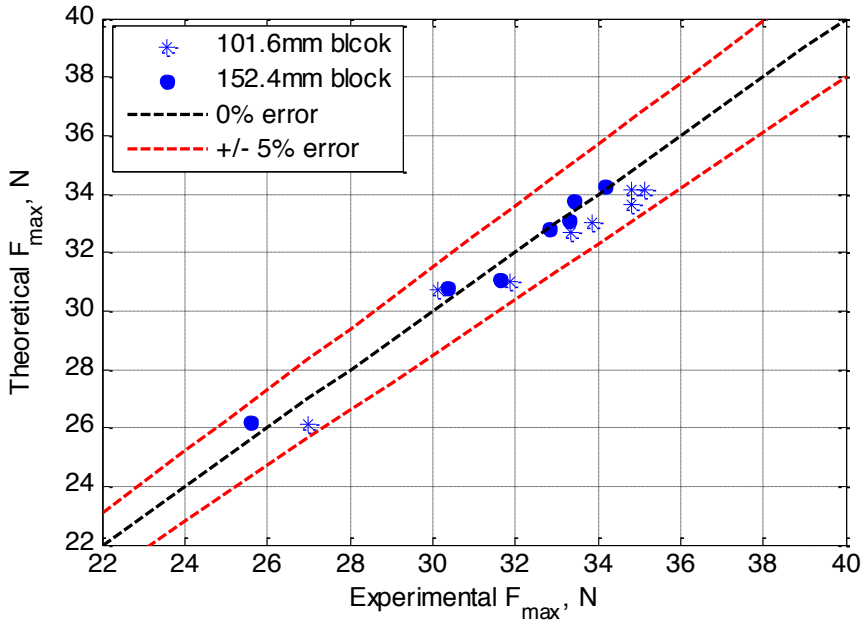

Figure 28: Experimental versus predicted peak impact force

Figure 29 shows the correlation between the predicted and the experimental impact duration, where the majority of the measurements fall in a relatively small range

from 0.75 to 0.85 msec, which can be demonstrated by the previous discussion about sensitive region in Figure 27. The two measurements out of the crowd in the chart are taken from two samples with the most severe cracks with longest transverse length and lowest depth. This phenomenon suggests that impact duration can be a good discriminator for a very severe damage, but for a crack which is relatively small and deep, it may not provide clear distinction from that measured from a good structure. Most of the points are still inside of the ±5% error margins, which are acceptable. Concentration of the impact durations for cracks of different dimensions requires good resolution at reading this discriminator from the experimental data, which yields needs for sufficient sampling points while collecting the force signal.

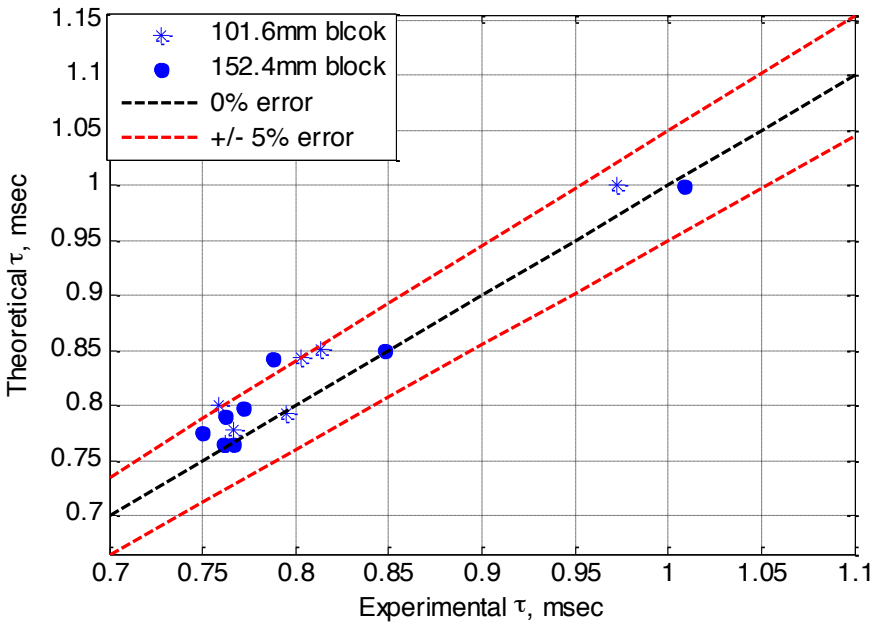

Figure 29: Experimental versus predicted impact duration

It can be concluded that there is a detectable or sensitive range for the impact dynamics method while using peak impact force and impact duration as defect discriminators. Alternatively it means that the cracks that are too deep or too narrow can be invisible to the current inspection method or a certain contact dynamics discriminator (F_{max} and τ). With the knowledge of a specific set of input parameters for the impact acoustic method including impact velocity, impactor's material properties, etc., the most ideal detectable range of the embedded crack can be roughly determined. Given the provided sample rubber blocks, which were made of materials similar as the rubber compound around the shoulder area, the estimated effective detectable crack is of depth less than 25mm from the impacted surface, and length greater than 15mm.

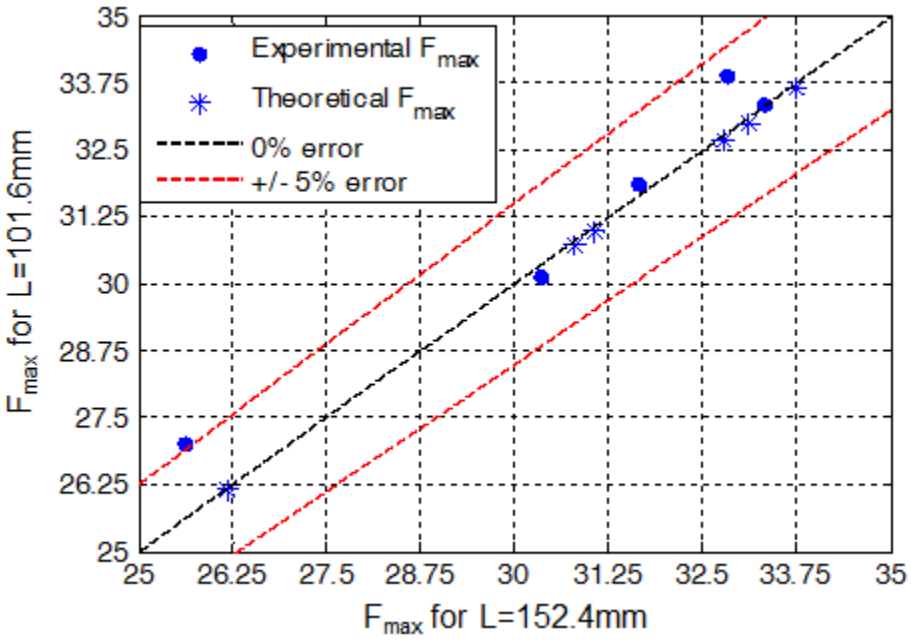

Figure 30: Effect of block length on F_{max}

Study of the effect of block lengths on the examined discriminators can provide experimental validation on approximating tire section into cubic rubber block. The peak impact forces measured for 101.6mm blocks displayed along the vertical axis in Figure 30 are compared to those of 152.4mm blocks along the horizontal axis. Most of the measurements are very close to the 0% error line, only with two outliers which are located in or around the 5% error boundaries. The good coherence between two sets of block lengths suggests that either block boundaries or target mass can bring in very little influence on the discriminators.

In Figure 31 and Figure 32, the peak impact duration and the impact duration were plot against the crack length for 152.4mm block with crack at depth of 12.7mm and 19.05mm respectively. The solid curves represent the theoretical calculations from the defect impact dynamics model and the symbols are measurements from the test data. The test data point at $l = 0$ corresponds to that measured from the integral rubber block. Both of the theoretically deducted discriminators agree well with the test data when the crack is at depth of $h = 12.7mm$. For the case of $h = 19.05mm$, the predicted impact forces still agree reasonably well with the test data, but the impact duration exhibits large discrepancy. The trend matches the conclusion made earlier according to sensitivity analysis of the theoretical model and the study on the relationship between the two discriminators and the impact velocities. The impact duration becomes very insensitive to change in the crack depth when the crack is deeper than 15mm, which yields large deviation between prediction and experimentation for the 19.05mm scenario.

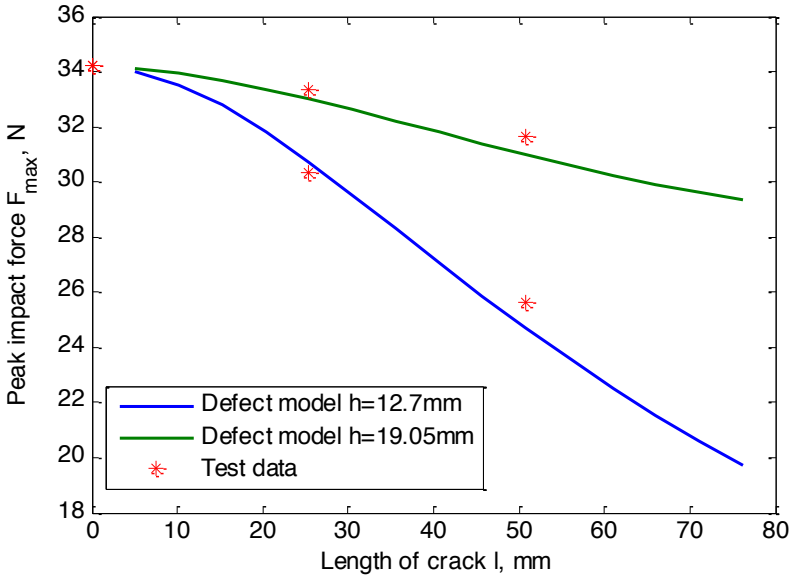

Figure 31: Peak impact force versus lengths of crack at h=12.7mm, 19.05mm (Comparison between predicted value and test data: good coherence)

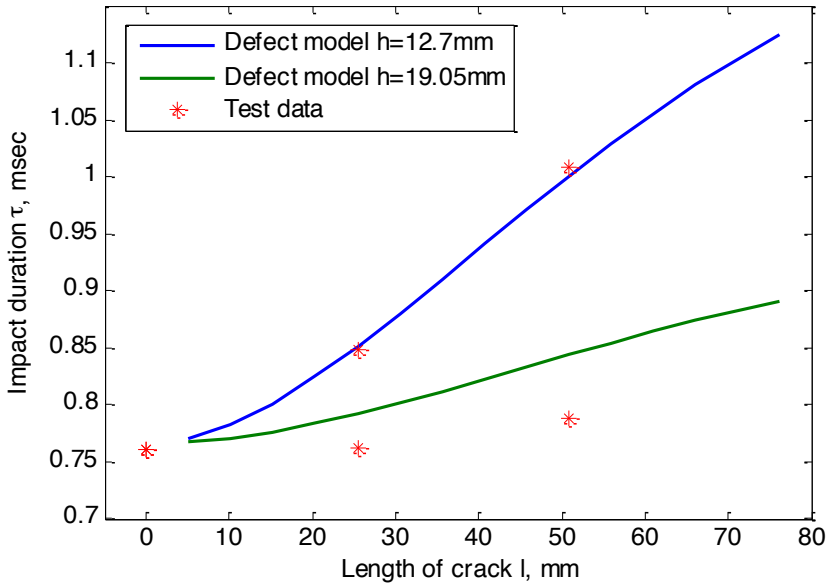

Figure 32: Impact duration versus lengths of crack at h=12.7mm, 19.05mm (Comparison between predicted value and test data: poor coherence for deeper crack)

4.3 Analysis of Acoustic Signal

4.3.1 Fundamentals of Acoustics

An acoustic wave is produced by a vibrating medium, involving solid, liquid or gas. The vibration results in a fluctuation in the ambient state of the medium radiating outward from the source of the vibration. Fluctuations above or below the normal air pressures are called compression and rarefaction. Compression of air particles results in high acoustic energy, and rarefaction yields low acoustic energy. Acoustic energy can be measured by either acoustic pressure or electrical voltage. The number of pressure fluctuations per second is called the frequency of sound, and is expressed in cycles per second, or Hertz.

Understanding the propagation of an acoustic wave in a medium is the critical basis for impact acoustics. General radiation of acoustic wave is actually the expansion of the wavefronts. The simplest case is that sound waves are emitted from a point acoustic source and wavefronts propagating spherically. The propagation speed of the wavefronts is a constant dependent on the nature of the medium that it passes through. The sound wave speed in dry air at 20°C is usually approximated as 343m/s. The physical size of the sound wave is defined by the wavelength, which is determined by the following equation:

$$\lambda = \frac{c}{f} \qquad \text{Eq. 36}$$

where c is the wave speed, and f as the frequency of sound. Thus at higher frequencies, the wavelengths become shorter. When the wavelengths are shorter compared to the

obstruction size in the path of propagation, reflections and echoes occur; while the wave diffracts around the obstruction when it is smaller than the wavelength.

Attenuation of the recorded acoustic energy is mainly affected by the distance from the vibration source. The relationship between the acoustic energies at two different distances from a point source can be expressed as

$$\frac{U_2}{U_1} = \frac{D_1}{D_2} \qquad \text{Eq. 37}$$

where U_1, U_2 are the recorded electrical voltages, and D_1, D_2 are the corresponding distances from the point source. The pressure fluctuations are usually sensed by electroacoustic devices which convert acoustic energy into electrical voltages. The electrical output corresponds to the instantaneous particle velocity in the sound wave. Therefore with the increase in the distance from the point source, the electrical voltage decreases caused by attenuated particle velocity.

The atmospheric effects also attenuate acoustic energy such as air absorption. The amount of air absorption depends on the humidity and temperature of the atmosphere. Other effects such as materials absorption can be neglected in the current study by placing the microphone adequately close to the impacted location.

4.3.2 Theoretical Analysis of Acoustic Signal

Impact generated acoustic signal is generally discussed in two stages: initial contact stage, and free vibration stage. Initial contact stage produces initial contact sound below the normal state due to the contact deformation on the impacted surface. Ringing

sound above or below the normal state is generated due to the impact-induced free vibrations of the structure. Since dynamic behavior of the impacted solid can be analyzed for both stages, it is worthwhile to link the impact acoustic signal with the dynamic responses. Based on the developed contact dynamics model in Chapter 3, the initial contact stage has been explained analytically.

According to the fundamentals of acoustic waves, impact acoustic signal reproduces the vibration energy of the impacted object. No one microphone will reproduce the dynamic responses perfectly, but in order to achieve a satisfactory interpretation, careful selection of microphone is crucial. Unidirectional electret microphone can be used for the purpose of eliminating noises and picking up signals from only one direction.

The signal can be analyzed in both time- and frequency-domain. The benefit of studying acoustic signal in the frequency-domain is to avoid the complexity in distinguishing multiple arrivals of acoustic waves received at the microphone. The focus is transformed into acoustic wave frequencies, which basically is associated with the modal frequencies of the impacted structure. The internal crack will introduce variation in the structural modal frequencies. The deformations happened on the surface of the impacted structure introduce compression and rarefaction of the ambient air, thus producing positive or negative sound pressures. Therefore the impact excited acoustic waves are actually recording the surface movements of the structure, and the frequency domain analysis of acoustic signal provides an easy means to screen out flexural vibration frequencies from resonant frequencies for a defective structure.

Before studying the effects of internal crack on the frequency features of acoustic signal, it needs to guarantee that the operating bandwidth of the microphone will cover the interested range of these modal frequencies. In order to excite all the resonances within the interested frequency range, the impact duration is decisive. It is known that an infinitely short impulse corresponds to a constant gain covering all frequencies in the frequency spectra. The bandwidth in this case is infinite, and inversely proportional to the duration of the impulse generally. A shorter impulse can excite a larger bandwidth. Therefore, the impact duration needs to be sufficiently small to obtain desired frequency contents.

It has been investigated earlier through the contact dynamics model that impact velocity and impactor's mass have phenomenal effects on the duration of impact, which in turn controls the excitable range of frequency components. Experimental studies are performed for both parameters, and the frequency spectrums are compared between two scenarios for each observing parameter in Figure 33 and Figure 34. The first figure compares the effects of impact velocity on frequency coverage, while the second figure investigates the effects of impactor's mass on the corresponding bandwidth. The figures indicate clearly that the frequency coverage is larger for higher impact velocity and lower impactor's mass, which matches the theoretical conclusions made previously. Consequently, selection of proper impact velocity and impactor's mass is significant to the success in the frequency domain analysis of the impact acoustic signal.

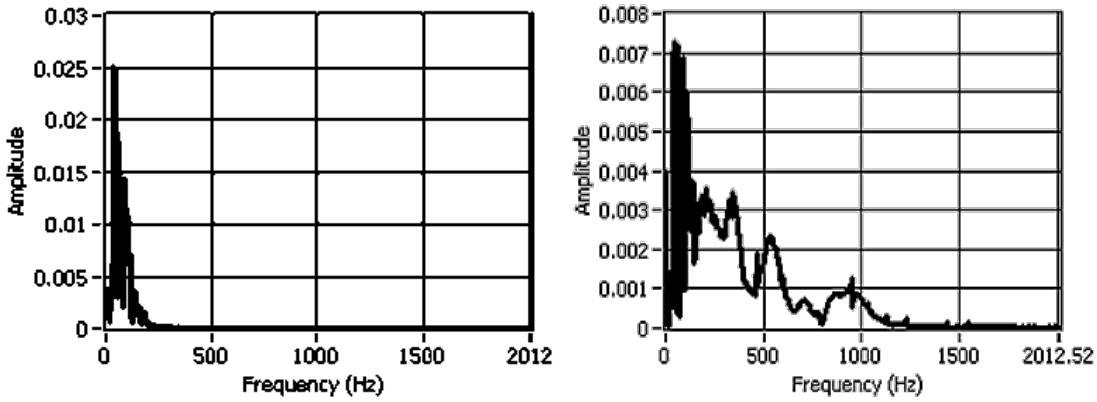

Figure 33: Effects of impact velocity on frequency coverage: $V_{i\_left} < V_{i\_right}$

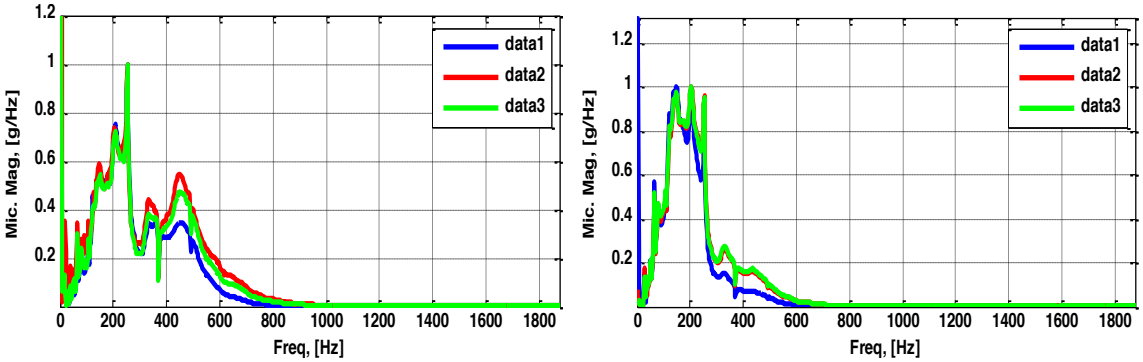

Figure 34: Effects of impactor mass on frequency coverage: $m_{1\_left} < m_{1\_right}$

Considering the attenuation effects as invariable during the sound wave propagation, the received acoustic signal by microphone can be estimated as

$$U(f) = G(f)v(f)e^{-\alpha D} \qquad \text{Eq. 38}$$

where α is the attenuation coefficient considered constant, and D is the distance from the source to the receiver. $U(f)$ is the received electrical voltage at frequency *f*, $v(f)$ is the vibration velocity of the source, $G(f)$ is the corresponding gain at frequency *f*. The microphone gain is usually not a constant value at lower audible frequency range (20-

200Hz). If the impact acoustic signal contains large amount of low audible frequency contents, the time-domain amplitudes $U(t)$ are distorted proportional reproduction of the velocity $v(t)$. Accordingly, the initial contact sound wave amplitude U_τ can be estimated as proportional to the velocity of vibration v_1 in the impacted solid. Furthermore, it can be derived by Eq. 39 to Eq. 41 that the area under the initial contact sound waveform A_1 is proportional to the maximum deformation d_{max} generated by the impact while assuming the displacement to voltage gain $G(t)$ is constant over time.

$$d_{max} = \int_0^\tau v_1 dt = \int_0^\tau \frac{U(t)}{G(t)e^{-\alpha D}} dt \quad \text{Eq. 39}$$

$$A_1 = \int_0^\tau U(t)dt \quad \text{Eq. 40}$$

$$A_1 \propto d_{max} \quad \text{Eq. 41}$$

The free vibration stage of the acoustic signal is an indirect measurement of the surface movements after the contact. Therefore the ringing sound amplitudes are dependent on the initial position of the structure at the beginning of free vibration. This initial condition can be assumed as the maximum deformation d_{max}, thus the solution for free vibration displacement x_2 can be written as

$$x_2(\mathrm{t}) = \sum_i e^{-\xi\omega_i t} d_{max} \sin(\omega_i t + \emptyset_i),\ t \geq \tau \quad \text{Eq. 42}$$

where ω_i is the i-th modal frequency of the structure.

Similarly the accumulated area under the ringing sound waves A_2 and the surface displacement x_2 are both integral of the measured sound amplitude $U_2(t)$ over time from $\mathrm{t} = \tau$ to the total sampling time t_s as

$$A_2 = \int_{\tau}^{t_s} U_2(t)dt \qquad \text{Eq. 43}$$

$$x_2 = \int_{\tau}^{t_s} v_2 dt = \int_{\tau}^{t_s} \frac{U_2(t)}{G(t)e^{-\alpha D}} dt \qquad \text{Eq. 44}$$

Therefore another proportional relationship can be derived by combining Eq. 42 to Eq. 44.

$$A_2 \propto d_{max} \qquad \text{Eq. 45}$$

Both A_1 and A_2 are marked in Figure 35, which are the two experimental features extracted from both stages of the time-domain acoustic signal, and are proportional to the maximum deformation.

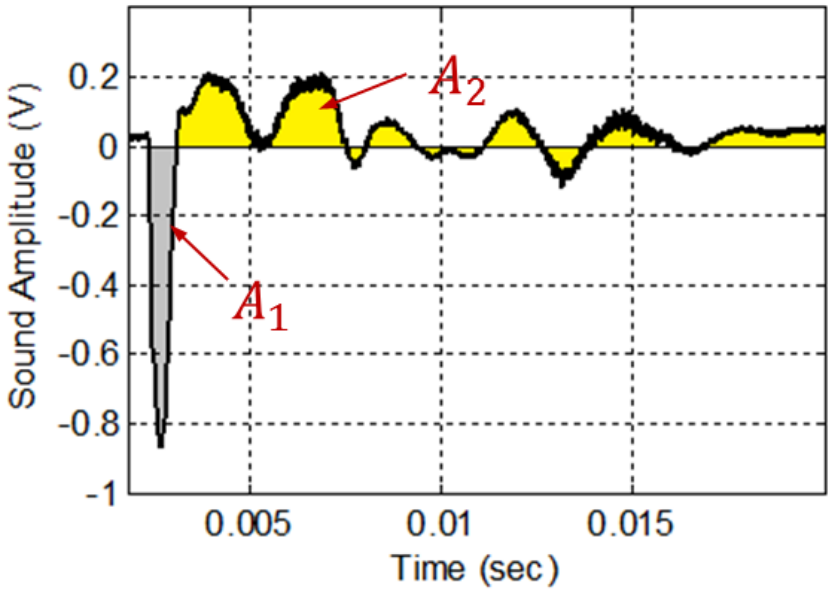

Figure 35: Time-domain acoustic signal

The maximum deformation d_{max} subjected to the impact at the end of the contact duration was analyzed in the contact dynamics model as related to the existence of internal crack. The maximum deformation is the superposition of the maximum contact deformation and the maximum flexural bending deformation as

$$d_{max} = \alpha_{max} + \delta_{fmax} \quad \text{Eq. 46}$$

where $\alpha_{max} = (F_{max}/K_c)^{2/3}$ and $\delta_{fmax} = F_{max}/K_f$.

The relationship between the maximum deformation d_{max} and the crack dimensions can be theoretically derived based on the developed defect model as shown in Figure 36. Contact deformation α_{max} and bending deformation δ_{fmax} varies in opposite direction with regard to increasing crack depth. Overally, the total maximum deformation decreases with increase in the depth of crack, which equivalently indicates that d_{max} gets increased by the presence of internal crack. This relationship is less significant when the crack is located deeper than around 20mm, which suggests that this dynamic quantity is also limited to reveal crack within a certain detectable range. As demonstrated from Eq. 39 to Eq. 41, the experimental feature A_1 extracted from time-domain acoustic signal should present similar trend as d_{max}, which will be discussed in next session.

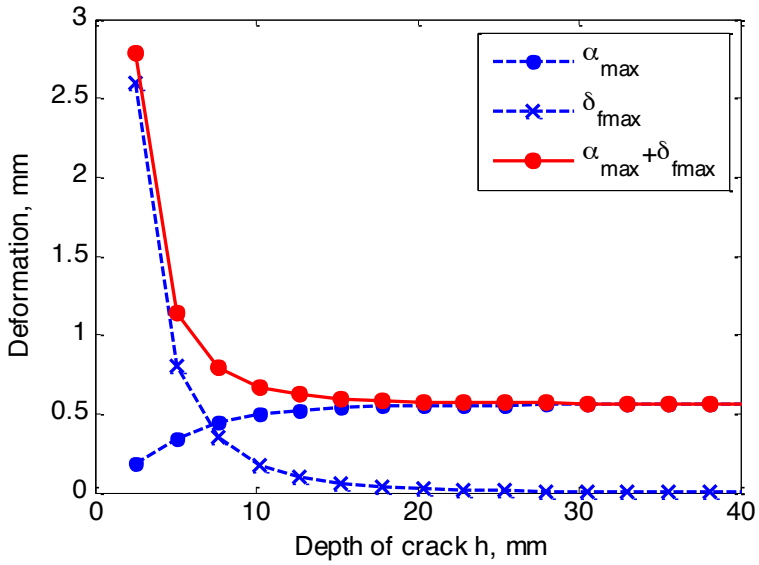

Figure 36: Predicted maximum deformation versus crack depth h ($l = 25.4mm$)

Ringing sound stage of the impact sound composes of multiple sinusoidal reverberations at all modal frequencies associated with structural free vibrations. It is more common to study the impact-induced free vibration behavior in frequency domain in the work by other researchers (Armstrong, et al., 1997). The natural frequency of a simplest single degree-of-freedom spring mass system is expressed by

$$\omega_n = \sqrt{m/k} \qquad \text{Eq. 47}$$

The fundamental basis of frequency-domain analysis for structural health monitoring is that defect usually lowers the structural stiffness k, thus resulting in increased resonant frequencies ω_n. Correspondingly, it results in richer frequency components at higher frequency bandwidth of the acoustic signal. The basic fundamentals of the increased natural frequencies are relied on the change in the energy dissipation, which was explained by the contact dynamics defect model that the total impact energy transformed into the structure is partially dissipated by flexural bending deformation caused by the internal crack as in Eq. 31. It is much more efficient to distinguish vibrations due to local contact deformation at lower frequencies from flexural vibrations at higher frequencies in the power spectrum of the acoustic signal than the time domain waveform. Flexural vibration energies U_f are directly related to the initial maximum deflection δ_{fmax} caused by the impact, while the amount of resonant vibration energies U_c can be attributed to the magnitude of the local contact deformation α_{max} as in Eq. 48 and Eq. 49

$$U_f = \int_0^{\delta_{fmax}} F_c d\delta_f \qquad \text{Eq. 48}$$

$$U_c = \int_0^{\alpha_{max}} F_c d\alpha \qquad \text{Eq. 49}$$

These two parts of energies would be overlapped and dissipated over time according to the hysteretic behavior of the real materials after the impact. The amount of energy in an acoustic spectrum reflects both stages of the impact acoustic responses: the initial contact stage and the free vibration stage. The flexural energy loss factor λ_f is a theoretical quantity that measures the percentage of energy lost by the flexural bending deformation. This flexural energy loss can be alternatively understood as contributed to the decrease in the structural stiffness. The bending stiffness of the materials above the internal crack K_f is a function of crack depth and length as in Eq. 23, where the increase in h and decrease in l both reduce K_f. So basically the bending stiffness decreases from infinite for an integral structure to a finite value for a defective structure, and reduces with growing severity of the internal crack. Therefore the energy loss factor can be estimated as an alternative measurement of increased higher frequency components.

4.3.3 Experimental Validation of Acoustic Time-Domain Discriminators

In the time-domain of the acoustic signal, two accumulated areas A_1 and A_2 were demonstrated as experimental interpretation of the maximum deformation d_{max}, thus can be adopted as defect discriminators. Experimental validation on the effects of internal defect on A1 is given by applying impact acoustic testing on the artificial rubber samples in this session.

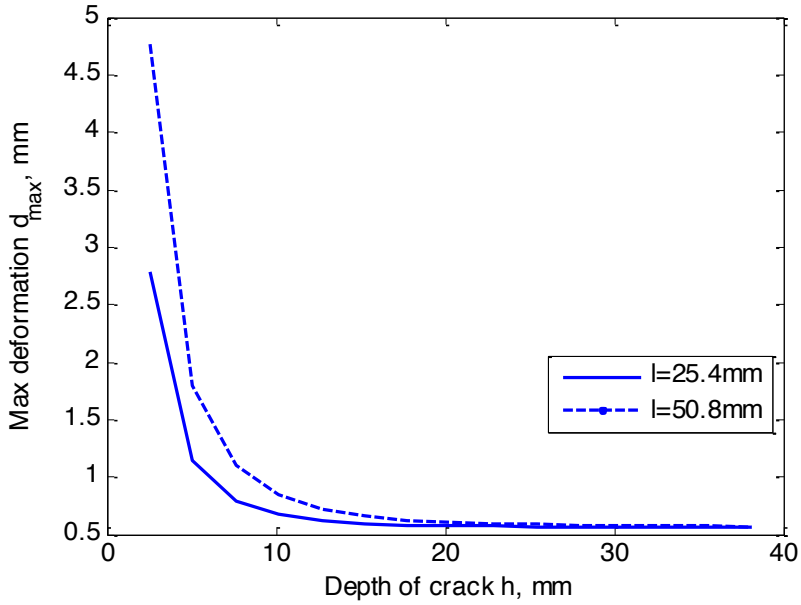

Figure 37: Predicted maximum deformation versus depth of crack

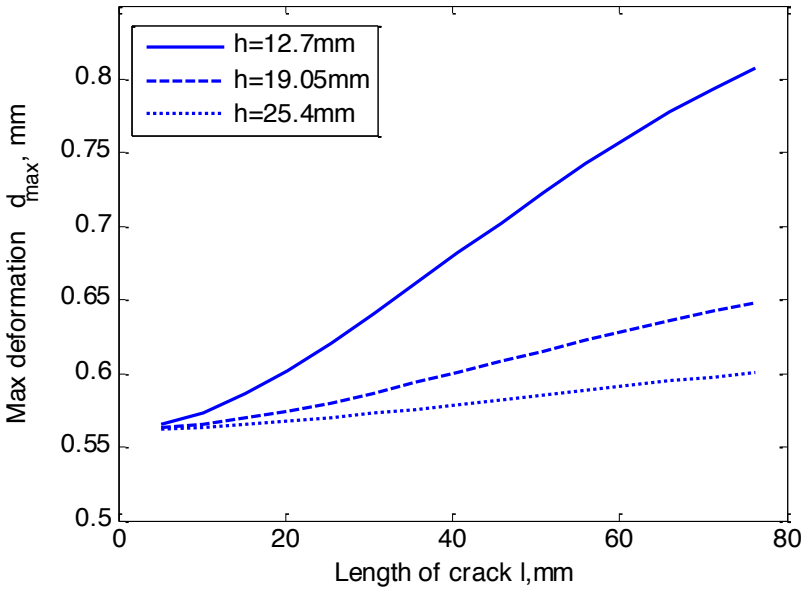

Figure 38: Predicted maximum deformation versus length of crack

Figure 37 and Figure 38 present the predicted results of maximum deformation d_{max} derived from the defect model versus the dimensions of the internal crack. It can be observed that d_{max} decreases dramatically as the crack gets farther away from the impacted surface. The curve for the narrower crack ($l = 25.4mm$) flattens out at a minimum d_{max} earlier than the curve for the wider one ($l = 50.8mm$). The two curves intersect at around $h = 25mm$, indicating that the effect of crack length has very little influence on the maximum deformation when the defect is deeper than 25mm. It also agrees with previous conclusions that it can be difficult to identify cracks deeper than 25mm. Similarly, the three curves in Figure 38 all initiate from a common point at a pretty small crack length, which should match the maximum deformation for the case of integral structure. In this figure, d_{max} gains much more quickly with the increase in growing crack length which locates closer to the impacted surface.

Experimental quantity that equivalently measures the maximum deformation is the initial area of the acoustic time signal A_1. Figure 39 shows the experimental attribute A_1 measured on 101.6mm rubber blocks versus the depth of crack compared between two different lengths. In Figure 40, A_1 is plot against the length of crack compared among three different depths. The two experimental figures correlate well with the predicted trends in Figure 37 and Figure 38. Thus experimental attribute A_1 has been validated to be correlated with the crack dimensions as the theoretical quantity d_{max} does, and it can be adopted to reveal the presence of internal cracks in rubber structures.

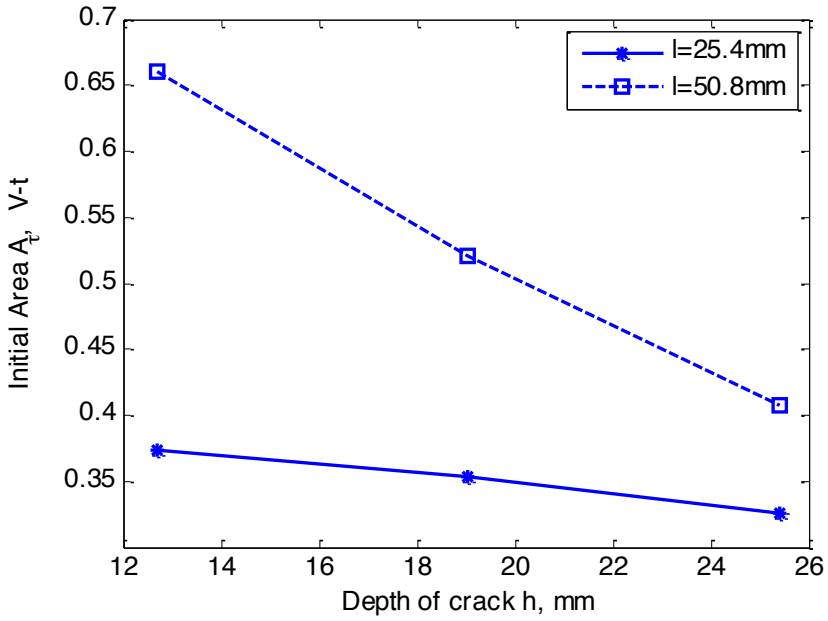

Figure 39: Experimental sound waveform attribute A_1 versus depth of crack

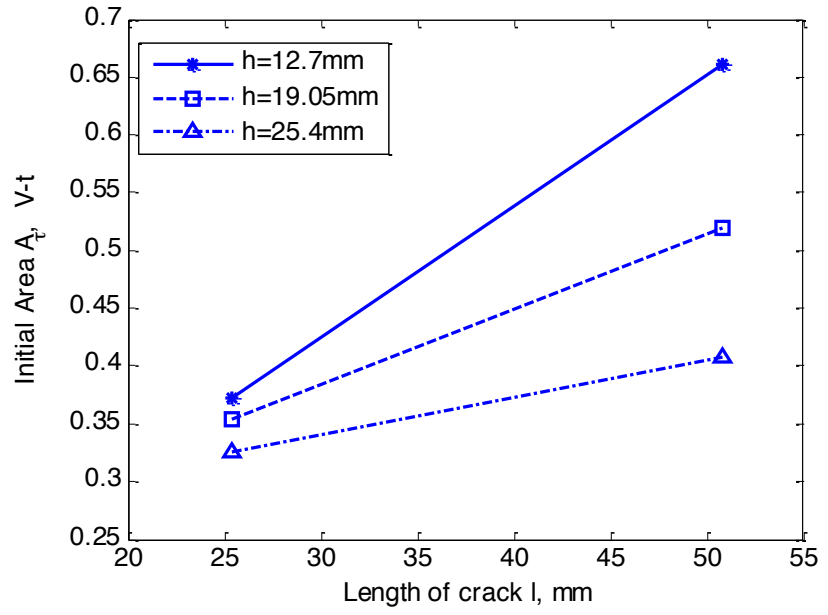

Figure 40: Experimental sound waveform attribute A_1 versus length of crack

The accumulated areas A_2 calculated from the ringing sound waves are plot against the depth of crack in Figure 41. It shows that increased severity of internal crack produces higher A_2, which matches the predicted trend of d_{max}. The two features A_1 and A_2 calculated from the time-domain acoustic waveform are both promising discriminators for internal crack in rubber structure.

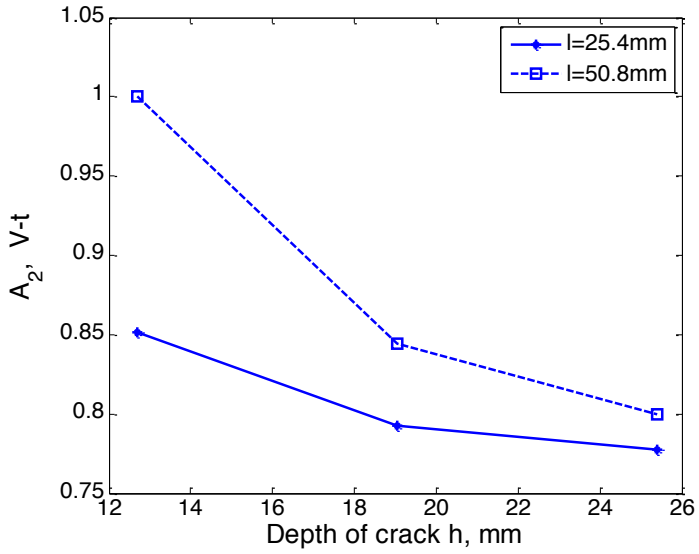

Figure 41: Experimental accumulated ringing sound area A_2 versus depth of crack

4.3.4 Experimental Validation of Acoustic Frequency-Domain Discriminators

Resonant frequency of the impact-induced vibrations subjected to local contact deformation can be estimated by $f_c = 1/2\tau$, thus $f_c = 640Hz$ for the case that impact duration $\tau = 0.78msec$. It can be observed directly in Figure 42 that spectral energy lower than 640Hz is higher for the integral than the two defective structures, and

becomes lower when the crack gets closer to the surface. Accordingly, the spectral energy higher than 640Hz assumed as attributed to flexural vibrations, is presented higher for defective structures due to the flexural vibrations introduced by the internal delamination. The relationship of the power spectral energy below or above 640Hz matches the trend of α_{max} and δ_{fmax} respectively, which in turn indicates that the effect of internal crack on impact acoustic responses can be identified through manipulation of spectral energies. Either the local peak amplitudes or accumulated spectral densities can be regarded as discriminators for defect identification.

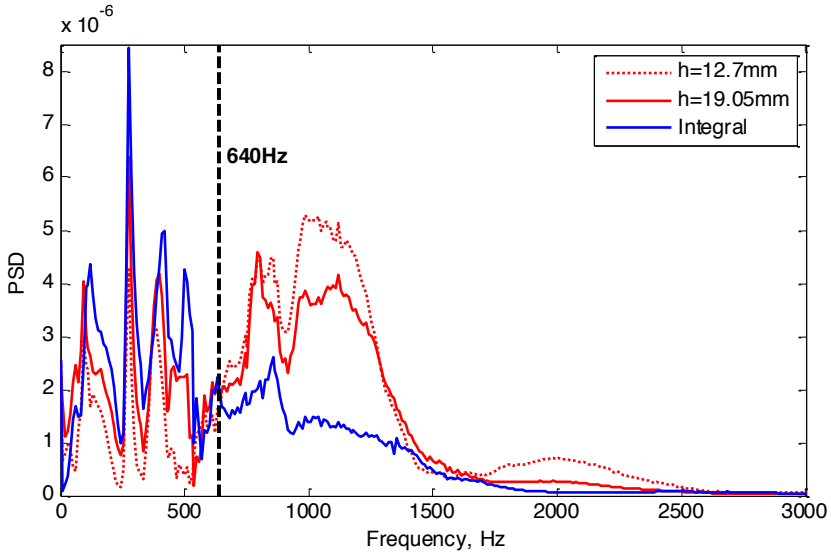

Figure 42: PSD of experimental acoustic signals (l=25.4mm for the two defective structures)

The shifts in modal frequencies are attributed to the flexural vibration of defective structure. They can also be related to the energy distribution ratio of the resonance to the overall vibration energy. The accumulative power ratio is defined for this purpose to examine energy distribution of an interested frequency range.

$$PR_i = \frac{\sum_{f>f_i}^{f_{max}} PSD(f)}{\sum_{f=0}^{f_{max}} PSD(f)} \quad \text{Eq. 50}$$

where f_i is the left boundary of the interested higher frequency range, f_{max} is the maximum frequency, $PSD(f)$ is the power spectral density at frequency f. It is reasonable to select f_i as the resonant contact frequency $f_c = 1/2\tau$. Compared to a healthy structure, the accumulative power ratio should be higher for a structure with internal crack. Impact acoustic tests were performed on the rubber block samples with artificial internal cracks. The power spectrums measured from each different sample are shown below in Figure 43 and Figure 44.

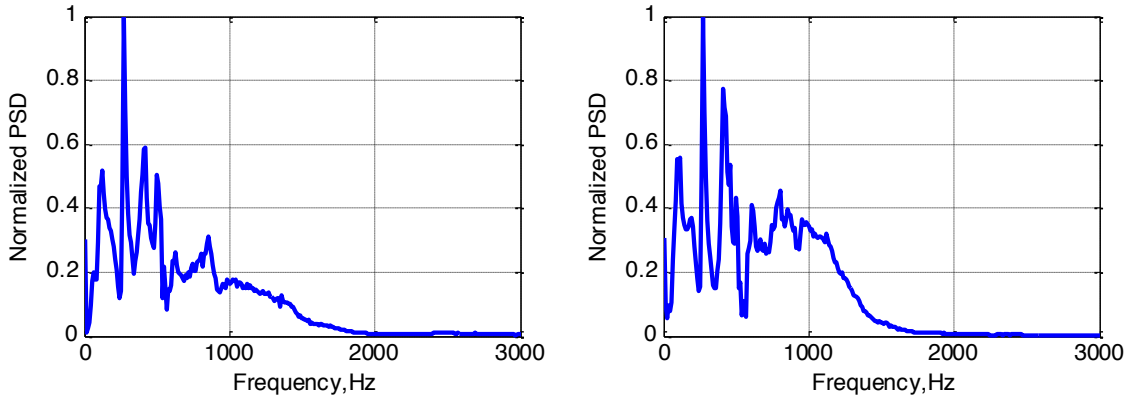

Figure 43: Normalized power spectrum of experimental impact acoustic signal
Left: integral rubber block; Right: $h = 25.4mm, l = 25.4mm\ L = 152.4mm$

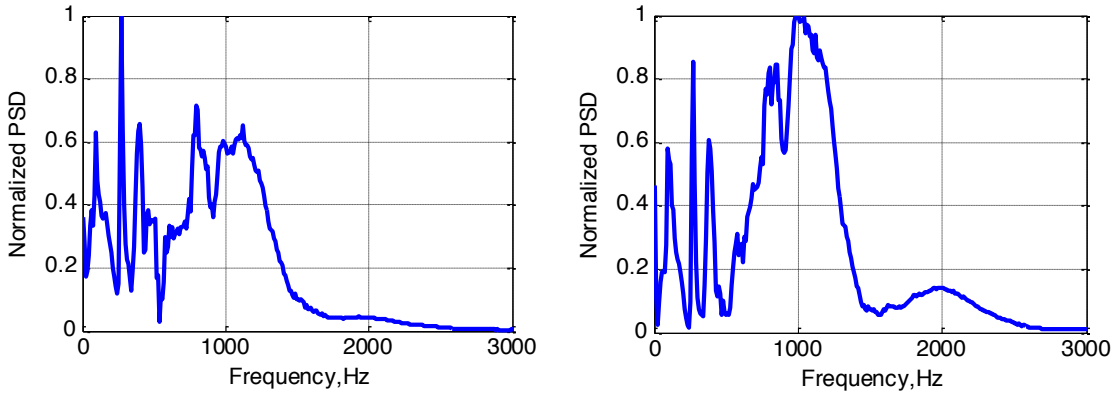

Figure 44: Normalized power spectrum of experimental impact acoustic signal. Left: $h = 19.05mm$; Right: $h = 12.7mm$ ($l = 25.4mm, L = 152.4mm$ for both)

The four power spectrums are experimentally acquired from an integral rubber block sample and three defective samples with cracks at depth of 12.7mm, 19.05mm, 25.4mm, respectively. All the power spectral densities are normalized to their corresponding maximum density in each plot. In comparison, the power density at higher frequencies (above 500Hz) becomes greater from the integral block to the shallowest cracked block.

Furthermore, a term ΔPR is defined as the difference of power ratio values of defective scenario from the integral measurement. The experimentally measured discriminator ΔPR is identical to the theoretically predicted λ_f, which both indicate the defect status of the structure.

$$\Delta PR = \Delta PR_{integral} - \Delta PR_{cracked} \quad \text{Eq. 51}$$

The power ratio values are calculated by taking the ratio of accumulated densities in the frequency range between 400 and 550Hz to those in the overall frequency coverage (0~3000Hz). The results for the four scenarios above are presented in Figure 45. Values

of ΔPR for the three cracked blocks are then calculated and compared to theoretical curve for λ_f versus depth of crack in Figure 46. It shows good accordance between the experimental discriminator ΔPR and the theoretically estimated flexural energy loss factor λ_f.

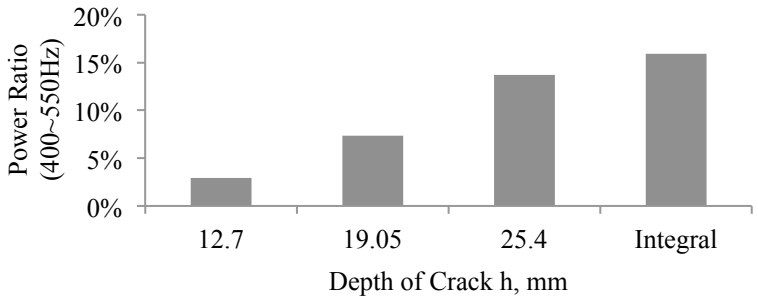

Figure 45: Experimental measured power ratio value versus depth of crack

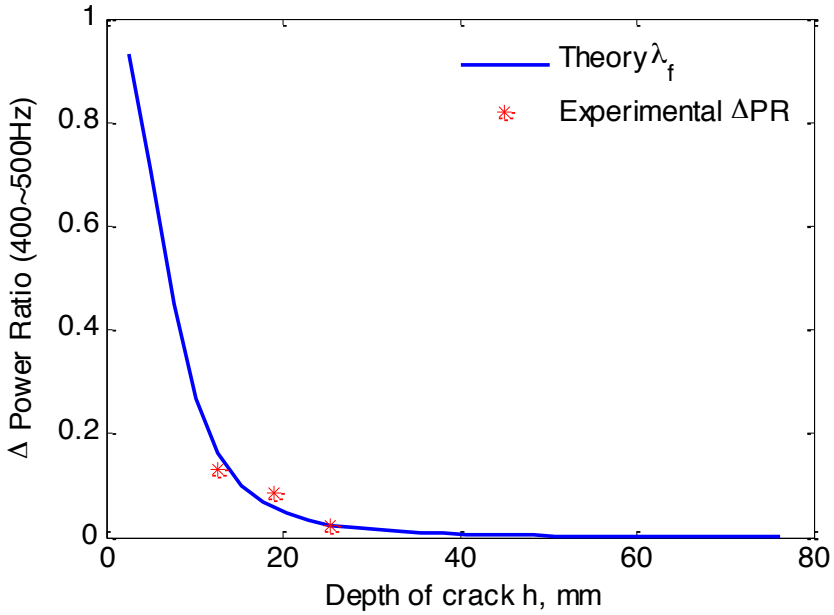

Figure 46: Comparison of theoretical calculated λ_f and experimental measured ΔPR (l=25.4mm, L=152.4mm)

5 EXPERIMENTAL IMPLEMENTATION

5.1 Introduction

In this chapter the experimental verification of the impact acoustic method is implemented on used truck tires. The purpose is generally to examine the used truck tire casings to determine the integrity conditions. Based on the previous two chapters, the impact dynamics model for both integral and defective structures were given, meanwhile both force-time function and acoustic signals in time- and frequency-domain associated with the impact acoustic method were analyzed. In a brief summary, there are seven discriminators verified feasible for inner crack identification: peak impact force, impact duration, area under initial contact sound, free vibration energy, accumulative power ratio, power spectrum local peak magnitude and accumulated spectral energy, see in Table 12.

F_{max} and τ can be measured directly from force-time as shown in Figure 47. A_1 and A_2 can be calculated from sound-time signal shown as the left chart in Figure 48. In the right chart, three discriminators are yielded based on the theoretical analysis of frequency-domain acoustic signal. The accumulative spectral energy is calculated as the area under the magnitude curve in the power spectral plot. E_f is the accumulative spectral energy calculated at frequencies higher than around $f_c = 1/2\tau$. P_f is the peak spectral density within the higher frequency range. The accumulative power ratio is obtained by taking the ratio between E_f and the total spectral energies.

Table 12: Summary of discriminators of impact-acoustic defect identification

Experimental Measurements	Experimental Discriminators		Analytical Contact Dynamics Quantities	
Force-time	Peak impact force	F_{max}	Peak impact force	F_{max}
	Impact duration	τ	Impact duration	τ
Sound-time	Area under initial peak	A_1	Maximum deformation	d_{max}
	Area under ringing sound	A_2	Maximum deformation	d_{max}
Sound-frequency	Accumulative power ratio	PR_i	Flexural energy loss factor	λ_f
	Local peak spectral density at higher frequency bandwidth	P_f		
	Accumulative spectral energy at higher frequency bandwidth	E_f		

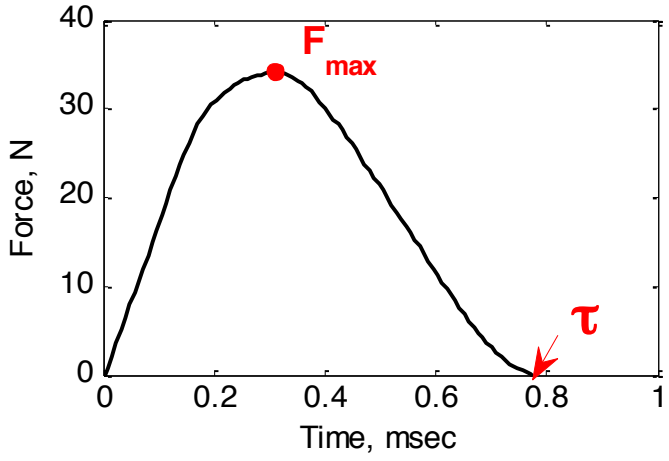

Figure 47: Force-time signal

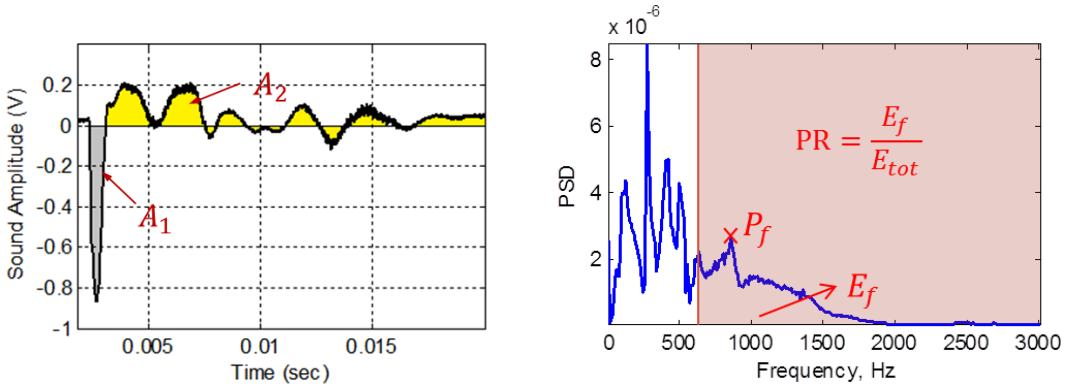

Figure 48: Acoustic-time signal and its power spectrum

Table 13 indicates how the model predicted dynamic quantities change for increasing crack depth and length respectively. It has been validated by testing cubic rubber samples with artificial cracks that the experimentally measured discriminators are identical to the corresponding analytical dynamic quantities. For example, lower F_{max} and higher flexural energy E_f can be measured from a defective structure than an integral one.

Table 13: Effect of crack dimensions on chosen parameters

Analytical Dynamic Quantities	**Direction of Change**		**Experimental Discriminators**
	Depth of crack h increased from 0 ~ ∞(integral)	Length of crack l increased from 0(integral) ~ ∞	
F_{max}	Increase	Decrease	F_{max}
τ	Decrease	Increase	τ
d_{max}	Decrease	Increase	A_1, A_2
λ_f	Decrease	Increase	PR_i, P_f, E_f

5.2 Experimental Setup and Instrumentation

In the experimental stage, used radial truck tires of three different belt constructions were tested by impact-acoustic method. The treads were buffed off for all the samples to guarantee uniform quantity of materials circumferentially to eliminate the effect of tread design variances. The focused area of defect examination is the belt edge separation at both shoulders of tire casing, as seen in Figure 49. The separation between the belt edge and the surrounding rubber materials usually predicts the initiation of severe tire failures, which lays parallel along the belt direction. The cracks can propagate into the belted regions in the under tread area resulting in catastrophic tread separations (Gent, 1994).

The experimental setup as shown in Figure 50 contains three major parts: the impact system, the tire rotation test bed, the data acquisition and processing system. The test bed is designed to test only one tire shoulder at a time automatically. For each tire shoulder, it approximately requires 170 seconds to run both tests and post-processing algorithm.

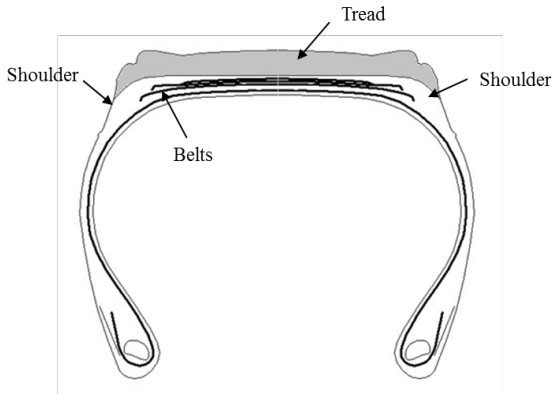

Figure 49: Cross section of a radial pneumatic tire

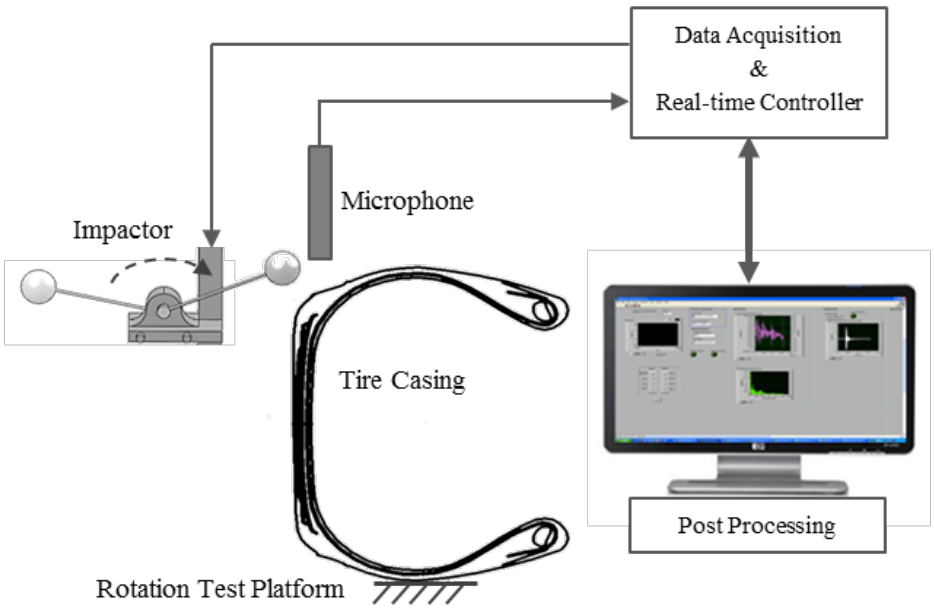

Figure 50: Experimental setup

The impact system includes a motor driven impactor and a microphone placing close to the targeted shoulder of the tire casing, with a fixed distance. Continuous experimentation was realized by implementing rotation after each measurement to a horizontal test platform, where the sample tire was centered on. The impactor has a miniature size and low mass (4.5g) IEPE force sensor designed to measure dynamic forces over a ±222N dynamic range scale, with sensitivity of 22.5mV/N. The DC motor driving the impactor can reach a maximum speed with maximum efficiency at 8170r/min, i.e. approximately 0.98m/s for the Ø2.3mm rotor. Therefore the impactor attached at the tip of a 50mm shaft can reach a maximum impact velocity at around 40m/s. The electret condenser microphone receives signal from a single direction covering acoustic frequency from 70Hz up to 20kHz.

Figure 51: Field test setup

The flowchart for the testing algorithm including data collection and post-processing is presented in Figure 52. Complete impact acoustic tests are performed circumferentially on both shoulders of the tire casing with desired resolution controlled by the rotation stepper motor. A minimal resolution of 0.9° can be achieved by running the motor under half step mode, while it is more decent to choose a sufficient resolution in order to save the cycle time. Test resolution is chosen as 3.6° in this work, which discretizes the circumference of the test line into 100 segments, as seen in Figure 53. After each impact and signals recording, the tire is rotated 3.6° toward the next test location until the entire circumference gets covered. The starting location of the test line, marked as 0° or 360°, is measured with two repetitions. For accuracy of the collected sound waveform, the minimum sampling frequency should be at least ten times of the highest frequency of interest. The sampling rate for acoustic signal acquisition is set as 41kHz for this purpose. Total number of samples is set as 16384, thus total recording time of the acoustic signal is 0.4 second, yielding a frequency resolution of 5Hz. The

Post-processing stage concludes discriminators extraction from both force and acoustic signals and further integrated analysis for defect identification.

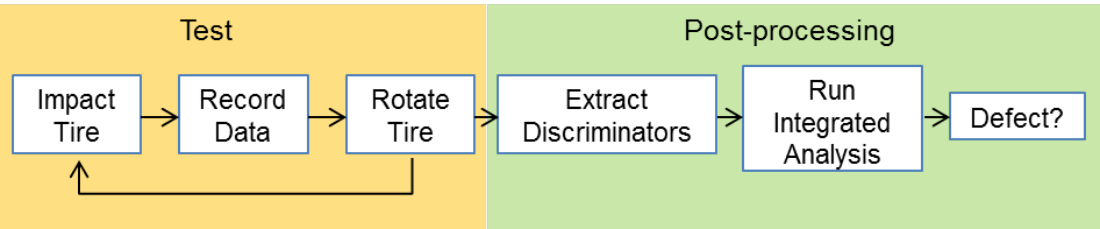

Figure 52: Flowchart of the test algorithm

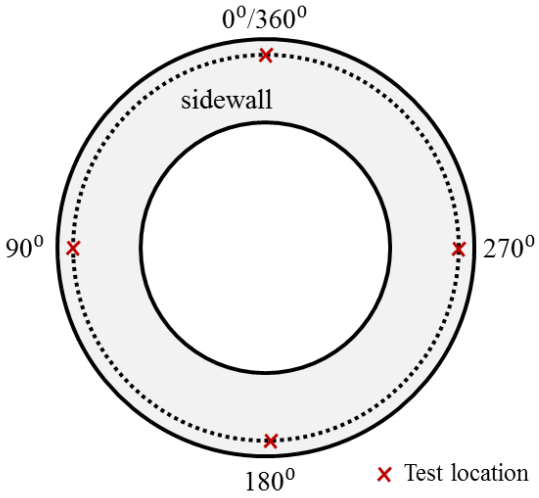

Figure 53: Test tire plan view, indicating the test line and locations

5.3 Shearography Interpretation

Each sample tire was preliminarily inspected by the Casing Integrity Analyzer (CIA) which is a shearography imaging tire casing inspection machine. A sample of shearography image is shown in Figure 54. The speckle patterns are presented

dominantly in shoulder 1 indicating severe separations around the belt edges, while the remaining areas without irregular spots are regarded as non-damaged.

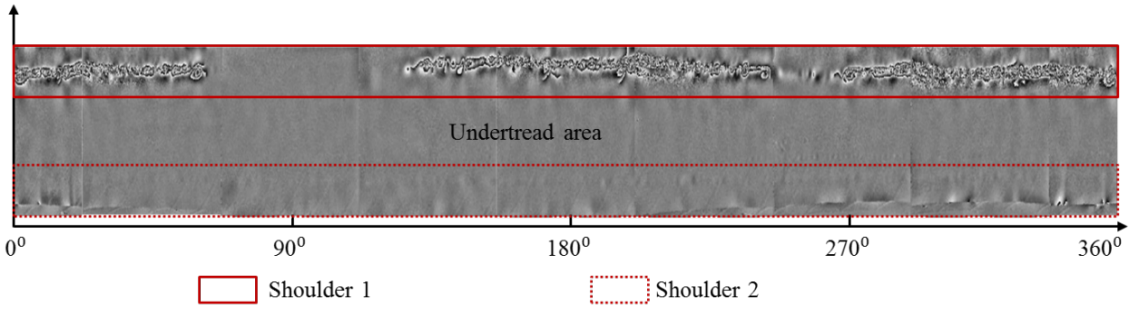

Figure 54: Shearography of a tire sample with severe damages in shoulder 1

The shearography image was used in the experiments to provide relatively reliable information about internal conditions of the tested tires. The image is taken from the inside of the tire, which is more sensitive to separations located near the tire carcass. However, some anomalies such as the crack seen in Figure 55 will cause this tire section not sensitive to the stressing during the shearography testing. Therefore the embedded crack around this region may be undetectable. The corresponding section of the shearography image in Figure 54 does not provide any abnormal information, however technicians believe that there are some internal cracks embedded. Experimental results investigated for this region using impact-acoustic method will be discussed.

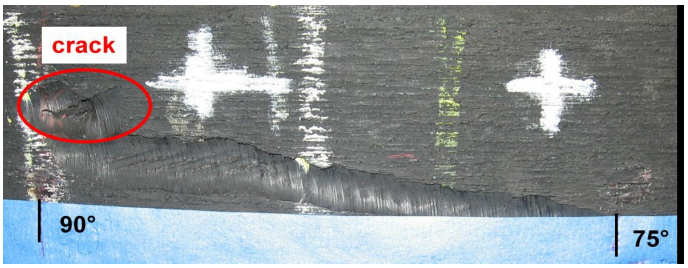

Figure 55: Shearography testing limited by existing surface cracks on a used tire casing

5.4 Experimental Results

Typical time histories of impact forces measured from the sample tire are shown in Figure 56. The two representatives are measured from the corresponding positions on the tire, which are selected from the integral and damaged area respectively according to the shearography image. The solid force-time curve for the integral spot presents higher peak force and shorter contact duration than the dashed curve of the damaged spot. The results agree with the theoretical impact dynamics model, in which higher impact force and shorter impact duration were predicted for an integral structure.

Figure 57 shows the typical time histories and the corresponding power spectrum of the impact sound measured from the same two spots as those in Figure 56. It can be easily observed from the sound-time waveform that the area under the initial downward peak is smaller for the integral spot than the damaged one. The analysis of the frequency-domain features requires the knowledge of the resonant frequency f_c subjected to the local contact deformation, which can be determined according to the impact duration that $f_c = 1/(2\times 0.9msec) \approx 555Hz$. In the power spectrum, it is obvious that the spectral densities at frequency higher than 550Hz are greater for the damaged curve, which indicates more flexural vibration energy due to the embedded crack. Accumulative power ratio PR calculated for the higher frequency components ratio, peak flexural spectral density P_f and accumulated flexural energy E_f can be taken as defect discriminators.

$$PR = \frac{\sum_{f=550Hz}^{2000Hz} PSD(f)}{\sum_{f=0}^{f_{max}} PSD(f)} \qquad \text{Eq. 52}$$

$$E_f = \sum_{f=550Hz}^{2000Hz} PSD(f) \qquad \text{Eq. 53}$$

The flexural bending deformation can be smaller than the artificial defective rubber sample, since the actual belt-edge crack in a tire structure usually presents much smaller gap between two separated surfaces than the artificial crack made in the rubber samples. This mitigates the effect of the resonant frequency shift by reducing the variances in the structural stiffness.

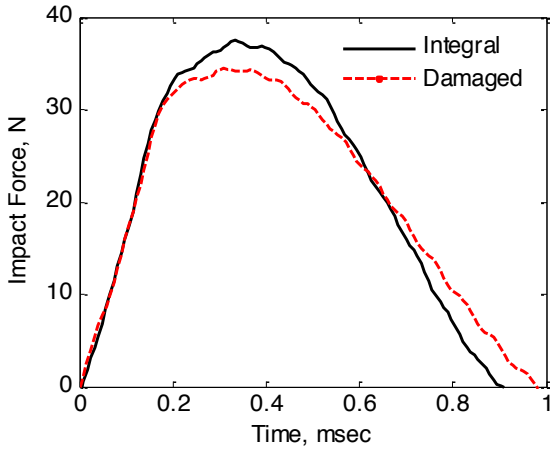

Figure 56: Typical time histories of impact forces measured from the sample tire

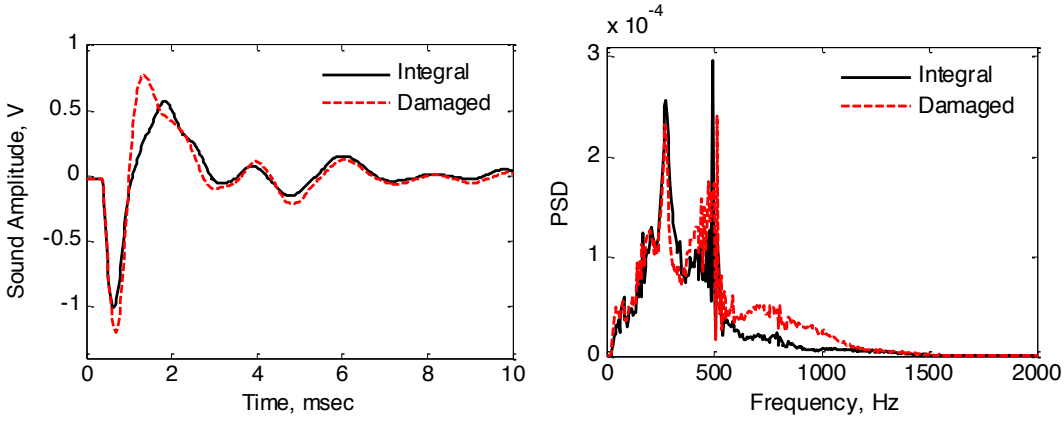

Figure 57: Typical time histories and power spectrums of impact sound

5.4.1 Effect of Impact Location

The contact area due to the impact was assumed as much smaller than the crack area in the theoretical impact dynamics model. However the actual lateral area of the crack can be very small which means the impact results are very sensitive to the impact location. In Figure 58, the scale is used for marking impact locations on the tire surface, where mark zero is determined by a referenced distance from the inner diameter of the tire casing. From the cross sectional view of the impact locations, 0mm are right above the edge of the second layer of belts. To evaluate the influence of the impact locations, three other locations toward the tire center are compared with the origin. Theoretically, smaller crack can yield less or subtle effect on the impact acoustic signals when the impact location is offset from the belt edge. Similarly, for cracks appeared at the belt edge of the first layer as shown in Figure 59, the current origin of the impact location scale can be insensitive to those cracks, but a higher impact location should be adopted.

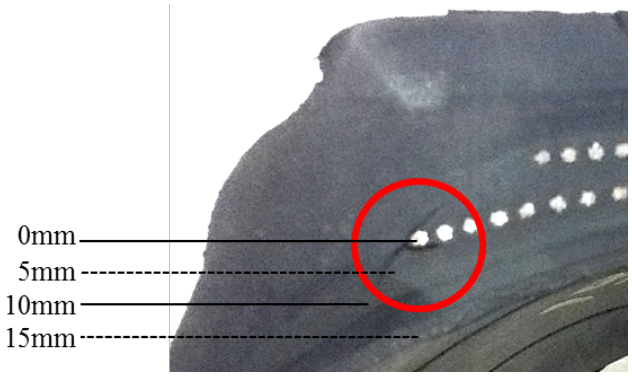

Figure 58: Scale arranged for four different impact locations

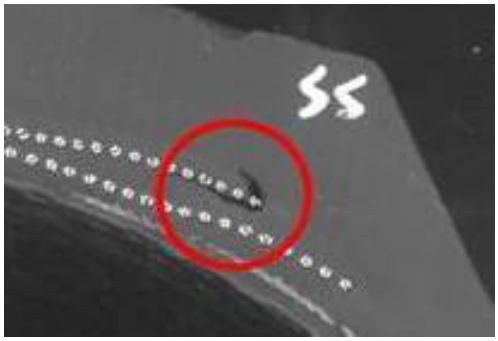

Figure 59: Small crack located at the edge of the first layer of belts

Figure 60 shows the influence of the impact location on the peak sound amplitude measured from shoulder 1 of the extensively damaged tire. Each curve represents 101 measurements at the corresponding impact location x for the entire circumference, with 2 repetitions at the initial test location. For the cracked areas, the peak sound amplitudes measured at x=0mm shows much larger discrepancy between the crack areas and the integral areas. For example, the amplitudes measured around 250 degree are as low as about 0.4V, but as high as 1.4V near 200 degree. The only mismatches between the amplitudes and the shearography are the region from 75 to 120 degree, where the shearography testing fails due to the surface crack as discussed in Figure 55. This suggests the advantage of the impact acoustic method over the shearography imaging method, since shearography testing can be strongly affected by surface damages that found in relative far field. Impact acoustic method is normally only affected by local surface damages or anomalies, and the testing results over this specific region indicate that there are embedded defects which were not discovered by shearography.

The other three curves are measured at x=5mm, 10mm, and 15mm respectively, which exhibit overall higher amplitudes than those of x=0mm. This can be attributed to

the decrease in the cross-sectional thickness from x=0mm to 15mm. The span of the curve becomes smaller when the impact location is farther from the origin, and the curve measured at x=15mm is almost flat. It indicates that the effect of cracks is less significant when the impact is not applied close to the crack. The results state clearly that the impact location affects dominantly on the impact acoustic discriminators, and it requires precise selection of multiple impact locations for comprehensive examination of the shoulder areas.

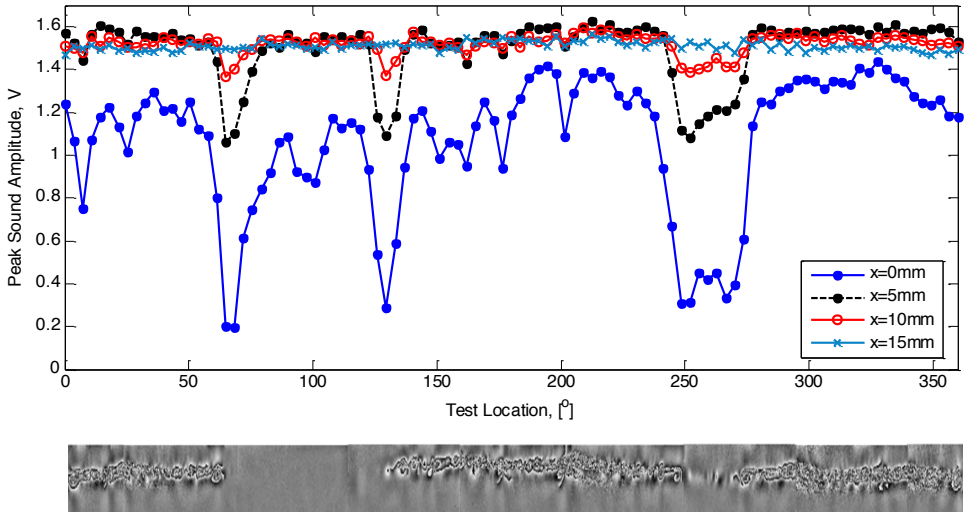

Figure 60: Influence of the impact location on the peak sound amplitude

5.4.2 Effect of Impact Velocities

In the sensitivity analysis of the contact dynamics model, the impact velocity has been identified as one of the most influencing factors on the dynamic quantities. Throughout sensitivity study, with the variance in the impact velocity, the dynamic quantities all change rapidly. It was pointed out in the theoretical study that the impact

duration at relatively higher impact velocities presents much smaller variations compared to lower impact velocities. The trend was experimentally examined on a specific location of a tire performing the impact acoustic tests, as seen in Figure 61, which demonstrates the theoretical predictions. As the impact velocity exceeds $1.4V_0$, where V_0 is the lowest velocity adopted in the experiments, the curve almost flattens out and even exhibits a certain amount of irregularities. The impact acoustic data can be unreliable when the impact velocity is too high. For the impact system used in the tire experiments, it is reasonable to keep the impact velocity lower than 2m/s in order to maintain the values of impact duration in a distinguishable range.

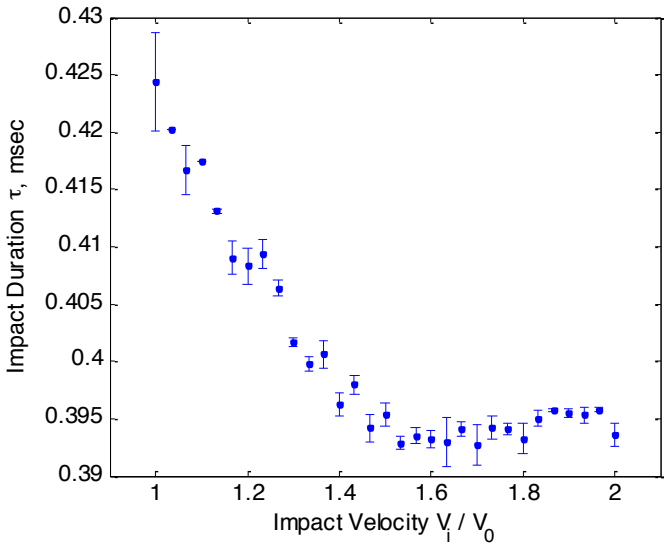

Figure 61: Impact duration versus impact velocity measured from a specific location on tire

Three different impact velocities were used to compare its effect on the impact duration and the peak sound amplitude. The results were plot against each corresponding test location on the tire shoulder as in Figure 62. Both discriminators can effectively indicate the defect conditions at all three impact velocities. The three curves in each plot

representing corresponding impact velocities are shifted from each other without much variance in the span. Comparing to the impact location, the impact velocity is much less influential in the defect identification. Moreover, the benefits of detecting a tire at various impact velocities can provide a set of paralleled information about tire casing integrity conditions, which is useful for system identification in the future study.

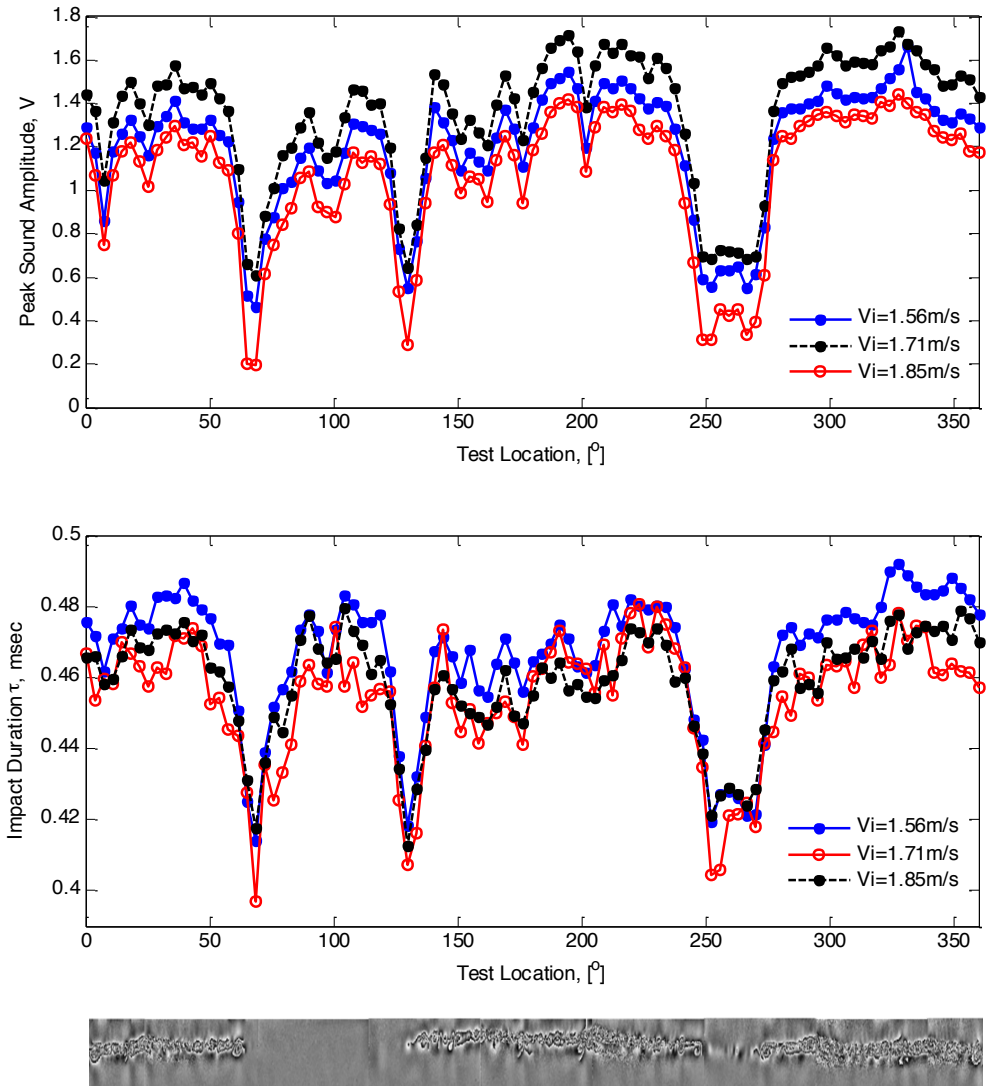

Figure 62: Influence of the impact velocity on the impact duration (upper) and the peak sound amplitude (lower)

5.4.3 Tire Inspection

All the impact acoustic discriminators were extracted for each measurement from the representative tire sample as plot in Figure 63 and Figure 64. Each plot is presented with results from two independent repetitions, where there are 101 measurements around the entire circumference for each repetition.

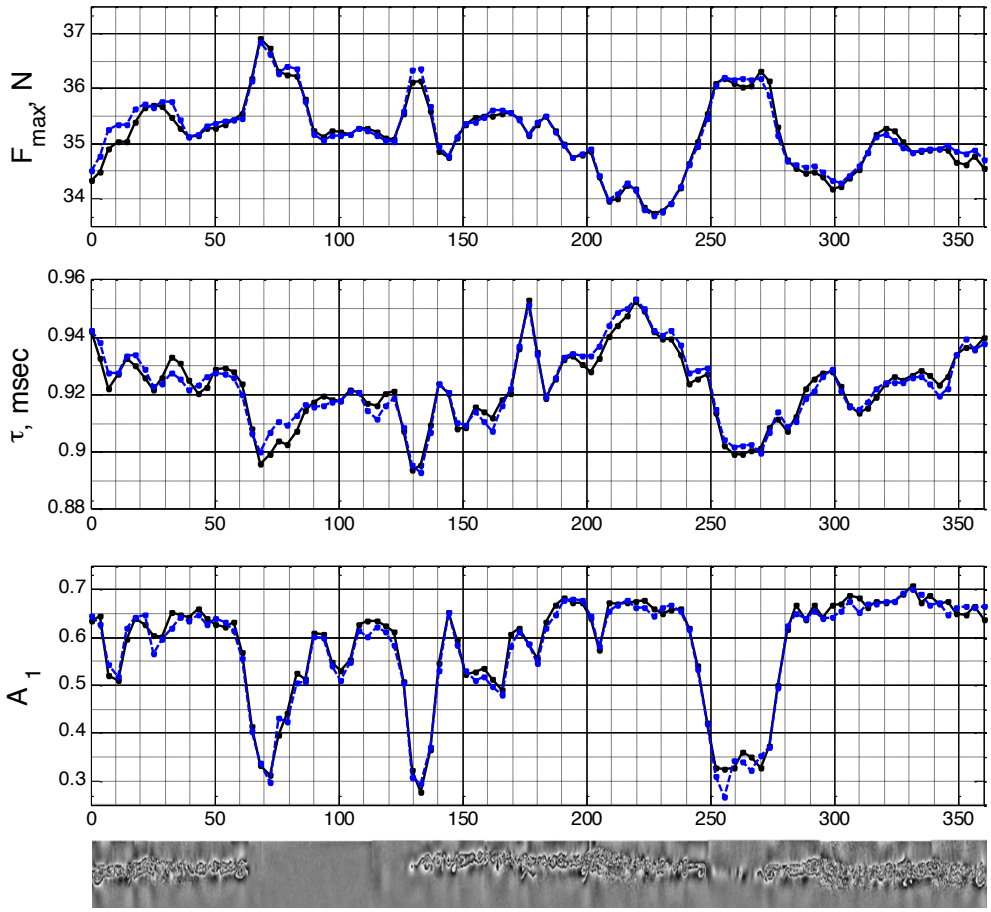

Figure 63: Defect discriminators measured on the representative tire shoulder

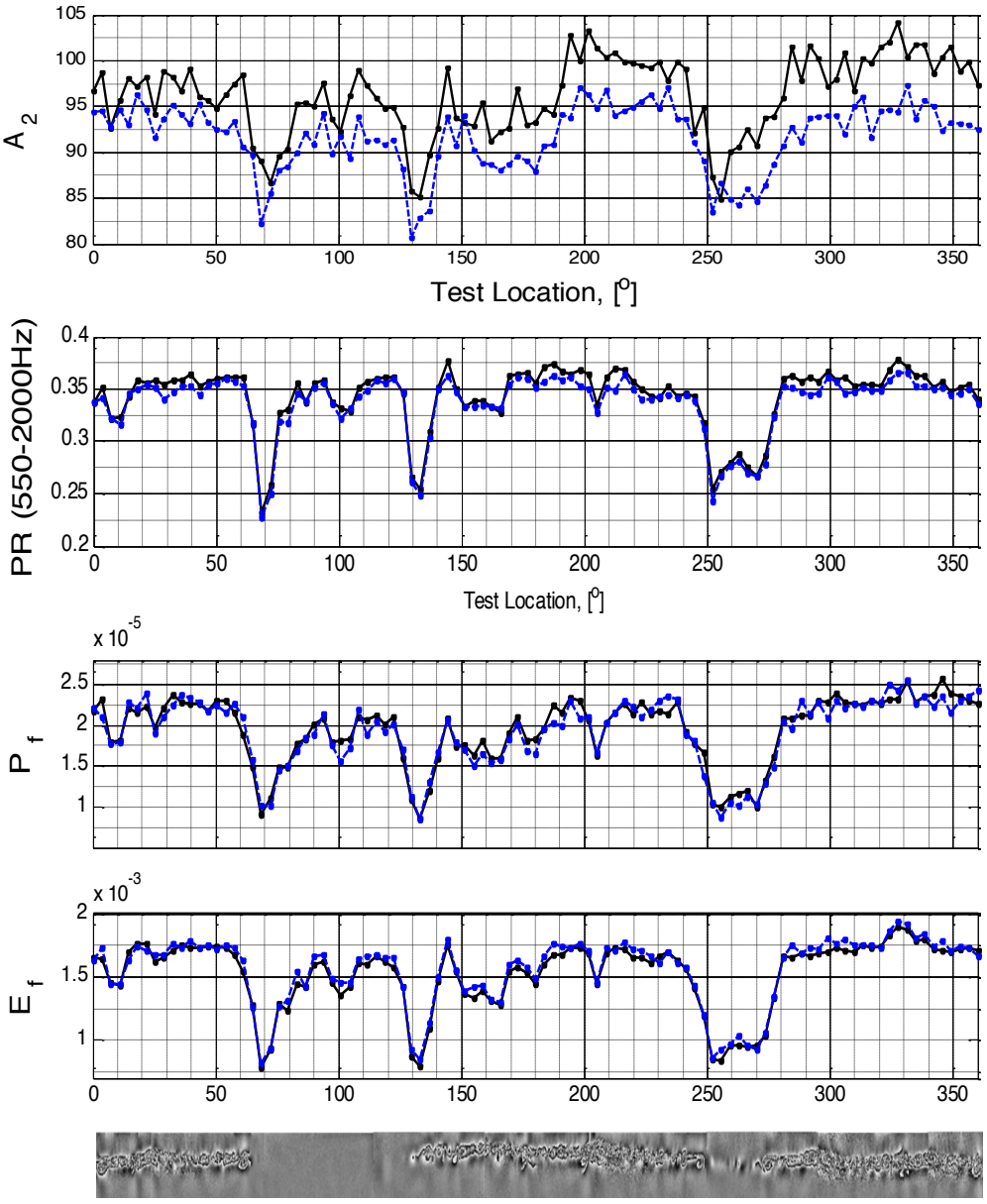

Figure 64: Defect discriminators measured on the representative tire shoulder

It is clearly that A_2 exhibits much poorer repeatability between two repetitions than the other six discriminators. This can be introduced by the variations in the acoustic attenuation effects between two repetitions, which will be magnified in the ringing sound. The accumulation of ringing sound amplitudes can enlarge this variation, resulting in

poor robustness. For the integration method that will be discussed next, A_2 is not included.

The first two discriminators extracted from the force-time signal present much more fluctuations over the circumferential measurements compared to the latter four discriminators calculated from the sound waveform. This trend can be clarified more clearly by performing statistical analysis of correlating the discriminators to the shearography results. Due to the difficulty in interpreting the shearography image, it is not easy to scale the extent of damage judging from the size or shape of the speckle patterns. A subjective method of rating the damaged conditions according to the shearography image was used to study the relationship between the discriminators and the defects. For example, in Figure 65, the overall shoulder is rated subjectively by five scales from 0 to1, where 0 indicates non-damaged, and 1 for most severely damaged condition. The ratings for the region from 75° to 110° are given as 0.25. The ratings are generally given on the basis of the lateral height of the speckle pattern, which to some extent representing the length of the cracks.

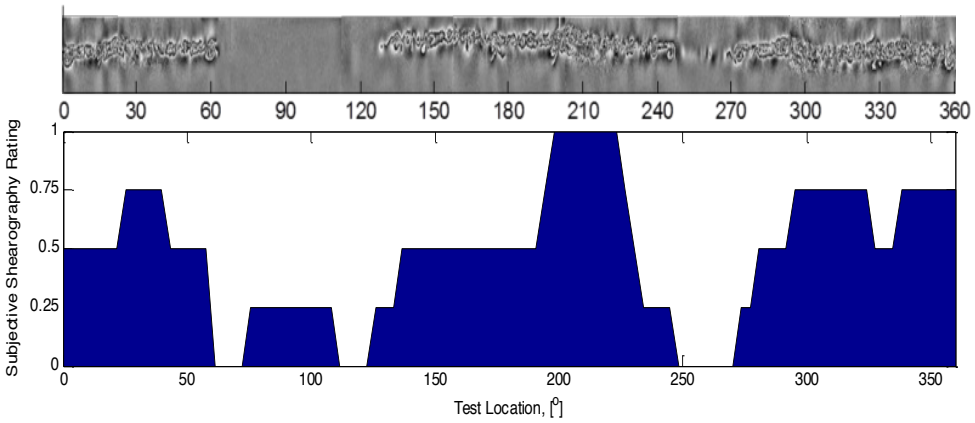

Figure 65: Subjective ratings of a shearography image

As a result, the force discriminators F_{max} and τ for 101 measurements were plot against the corresponding subjective shearography ratings as in Figure 66. The mean values in the plot are connected indicating the effect of the defects on the discriminators. Because the subjective ratings can more or less deviate from the actual situations, the range of box varies widely in the plots indicating poor statistical convergence. However, the mean connecting line is a relative more reliable statistical feature, which assumes that the means can represent the most dominant values of the discriminators of each corresponding group. The trendline shows decreasing F_{max} and increasing τ for aggravated damaged condition, which matches the theoretical results. Similar analysis was also performed on another two discriminators extracted from the acoustic signals, and the corresponding statistical boxplots are shown in Figure 67. The mean connecting lines of the initial area A_1 and the power ratio PR versus the subjective shearography ratings agrees reasonably well with the predicted trend. Whereas the acoustic signal discriminators seem not as sensitive to damage intensity as the force signal discriminators. This phenomenon is reflected through the fact that the slope of the connecting lines is approaching zero while the shearography rating becoming higher, which means the later two discriminators are affected less and less dominantly with growing damage intensity. This result suggests that the discriminators of the force signal are more sensitive to the variations of the lateral area of the cracks, which is promising to be further investigated for defect characterization. However, the differences in those discriminators between integral and defective regions are much less distinguishable than the ones extracted from the acoustic signals.

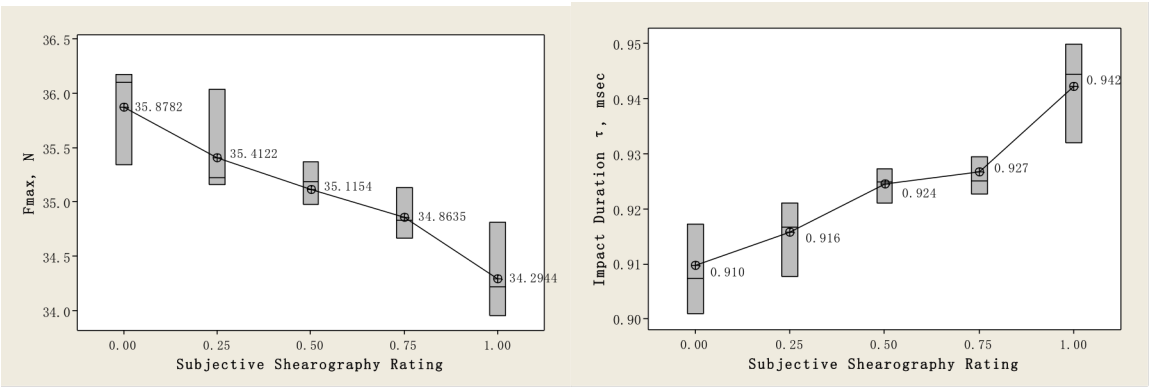

Figure 66: Boxplot of force discriminators versus subjective shearography ratings

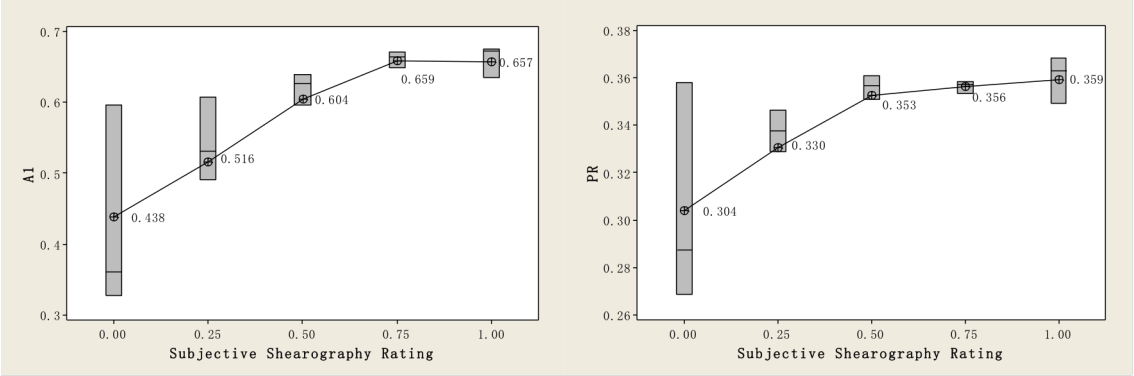

Figure 67: Boxplot of sound waveform discriminators versus subjective shearography rating

From the standpoint of defect identification which aims at pursuing a threshold value to distinguish damages from good conditions, the acoustic discriminators provide better contrast. In fact, it is desirable to take advantage of all the discriminators from both force and acoustic signals.

The normalized root-mean-squared-error (RMSE) is calculated between two sets of repeated measurements for each discriminator and normalized by the range of the data as in Eq. 54. Then the RMSE indices were compared in Figure 68, where it shows very small normalized RMSE indices for all the evaluated discriminators. It can be noticed

that the accumulated flexural energy E_f with much lower RMSE than the peak flexural magnitude P_f provides a discriminator with better robustness. The power ratio PR as a normalized index eliminates uncertainties introduced by measurement errors and deviations among samples, and has the lowest RMSE indicating good repeatability.

$$Nor\_RMSE = \frac{\sqrt{\sum_{i=1}^{N}(y_{i1} - y_{i2})^2}/N}{(y_{max} - y_{min})}, \qquad N = 101 \qquad \text{Eq. 54}$$

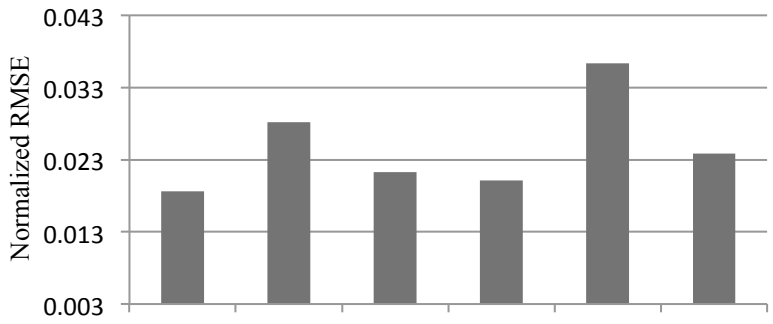

Figure 68: Normalized RMSE of discriminators between two independent repeated tests

Another mean of evaluating the statistical performance of the discriminators is depicted by boxplots in Figure 69, which groups data with subjective shearography rating greater than zero as defective. Greater spacing between the defective and integral boxes indicates higher degree of dispersion in the discriminators for defect identification. The spread of each box represents the size of the group, which ideally is greater for the defective group and less versatile for the integral data. Accordingly, some of the discriminators which provide better robustness as summarized earlier, such as PR and E_f, does not agree as well with the ideal characteristics of the boxplots as the other discriminators. In short conclusion, it is more reliable to combine all the useful

discriminators for the purpose of achieving a single defect index with good robustness and repeatability, better correlation with defect and higher quality of defect identification.

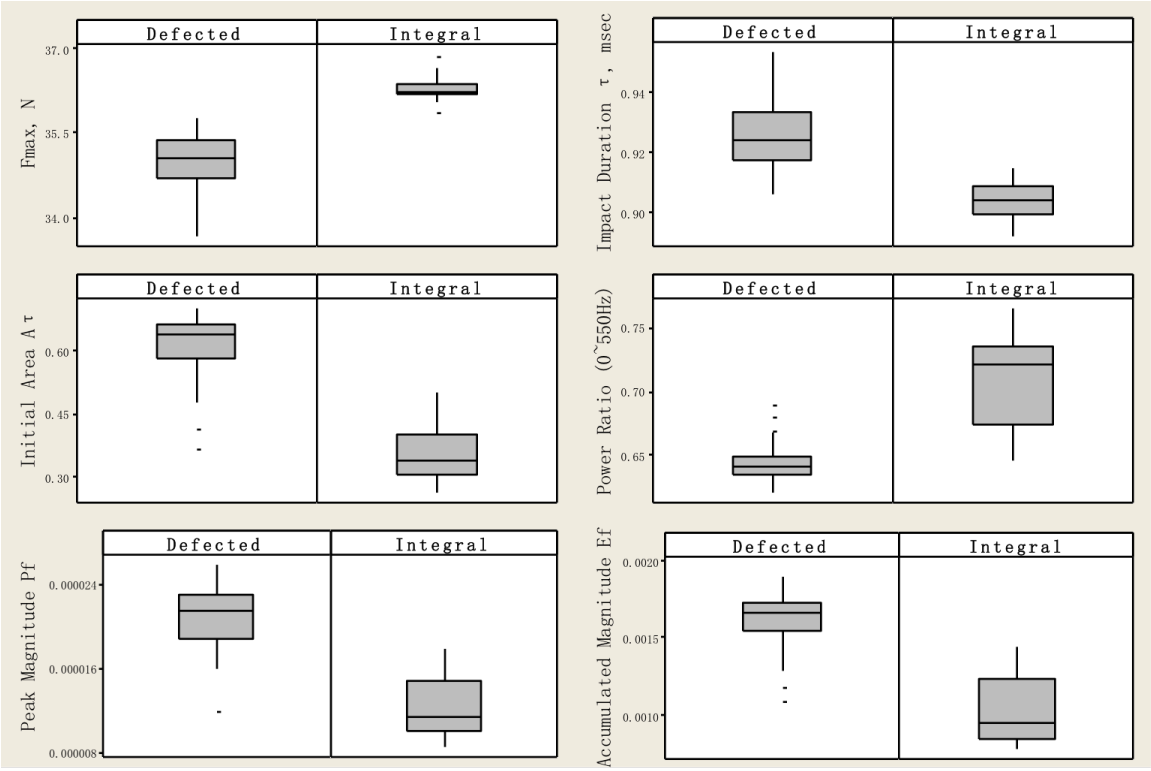

Figure 69: Boxplots of the discriminators

In Figure 70 and Figure 71, the six discriminators (E_2 excluded) are plot for both shoulders from the averaged results of two repeated test data measured on the representative tire. The shearography image of the second shoulder indicates no damages found. It can be seen that the discriminators for this shoulder present much less variations compared to the results for the damaged shoulder. For F_{max} and PR, the values for the second shoulder are generally higher than the values for the damaged regions, and matches with the non-damaged regions in the first shoulder. For the other four discriminators, the second shoulder curves are located lower than the non-damaged

regions of the first shoulder, which are in good accordance with the predicted trend. Variations in the discriminators can be observed in the curves for the beginning 100 circumferential degrees in the second shoulder, which can possibly be due to the embedded initiating cracks which are not easily detected by the shearography method, but degrade the structural stiffness thus sensed by the impact acoustic discriminators. If to look back at the shearography for the second shoulder, some anomalies can be observed but not as noticeable as the anomalies in the first shoulder.

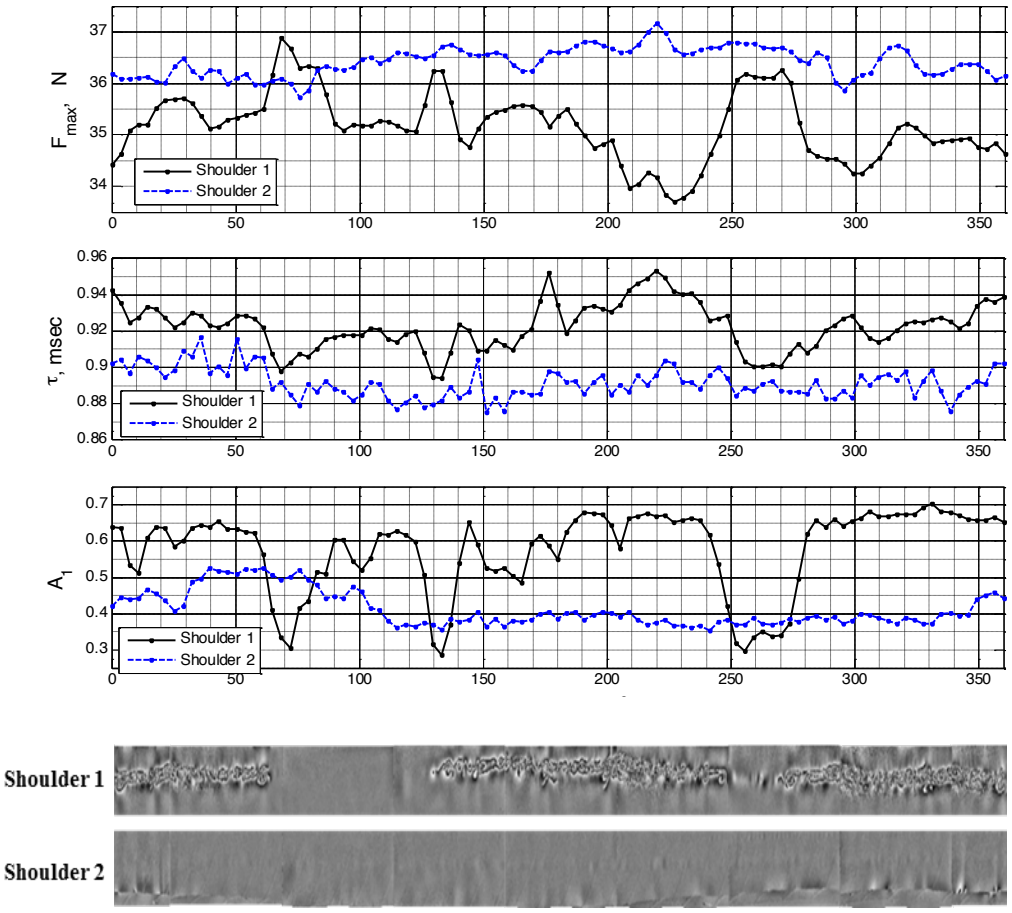

Figure 70: Defect discriminators measured for both shoulders on the representative tire

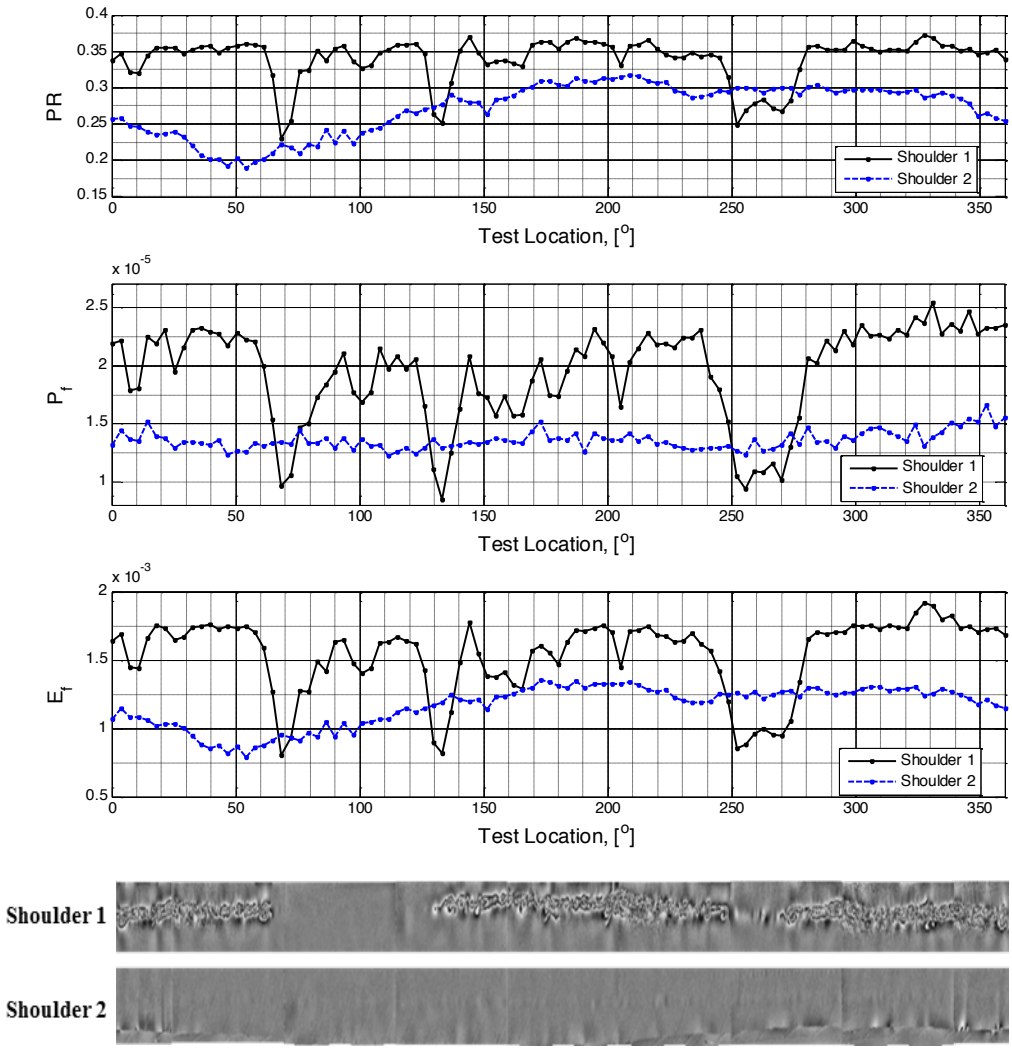

Figure 71: Defect discriminators measured for both shoulders on the representative tire

5.4.4 Interpretation of Results

To combine seven discriminators into a single robust defect index, the most intuitive method is to calculate the weighted mean as illustrated in Figure 72. The defect index DI can be calculated through Eq. 55 and Eq. 56, which performs a scaling to put the original discriminators into [0, 1] range denoted as normalized discriminators y_i. To

obtain the same scales for all the normalized discriminators where 0 stands for non-damaged and 1 for most severely damaged, it can be simply realized by setting $x_m = x_{max}$ for F_{max} and PR, and using $x_m = x_{min}$ for the rest of the discriminators.

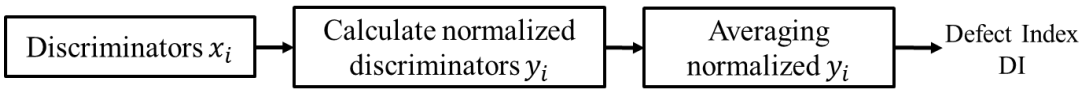

Figure 72: Schematic representation of the integration method

$$y_i = \frac{|x_i - x_m|}{x_{i,max} - x_{i,min}} \quad \text{Eq. 55}$$

$$DI = \left(\sum_{i=1}^{N} y_i\right) \Big/ N \quad \text{Eq. 56}$$

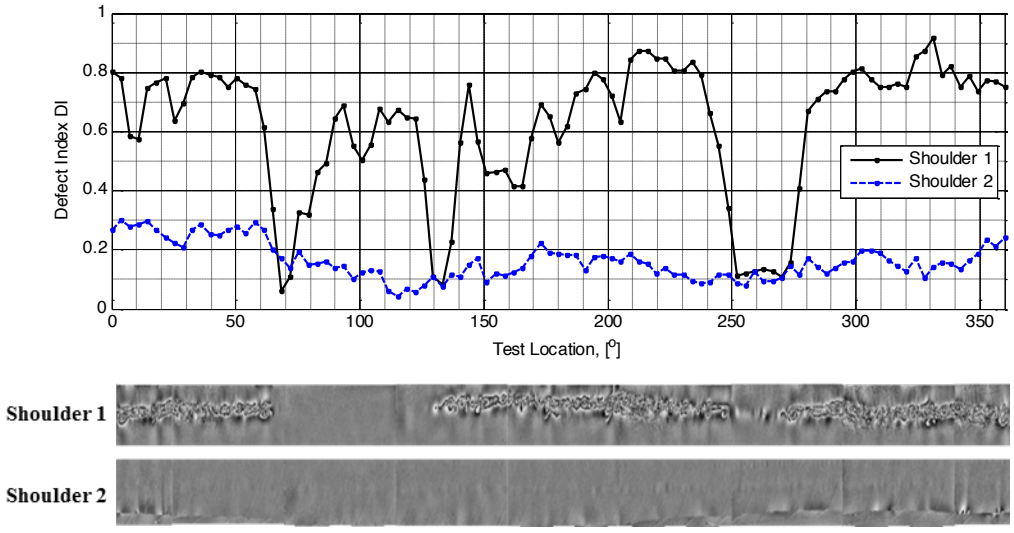

Figure 73: Defect indices for the representative tire

The corresponding defect indices for the representative tire were plot against each test location for both shoulders in Figure 73. The $x_{i,min}$ and $x_{i,max}$ are the minimum and maximum x_i measured from the first shoulder on the representative tire, and shared for

the other shoulder of the same tire and both shoulders for the other two sample tires. The defect indices were also integrated from the discriminators extracted from the recorded impact acoustic signals. For the brand new tire in Figure 74, the defect indices are almost zero for both shoulders. In Figure 75, discontinuous speckles are shown in shearography image of the first shoulder, indicating initiation of belt edge separations in the shoulder area. The impact acoustic indices pointed out the two butterfly shaped speckles around 180 degree in the first shoulder. The DI values are generally around than 0.25 for this shoulder and almost zero for the second shoulder, showing good contrasts between damaged and non-damaged conditions. A significant point of the integration method is that three tires of different constructions (with same inner diameter, and tread buffed) share a single set of parameters for normalization, which is of practical worth to propagate the method to larger populations of tires for defect inspection.

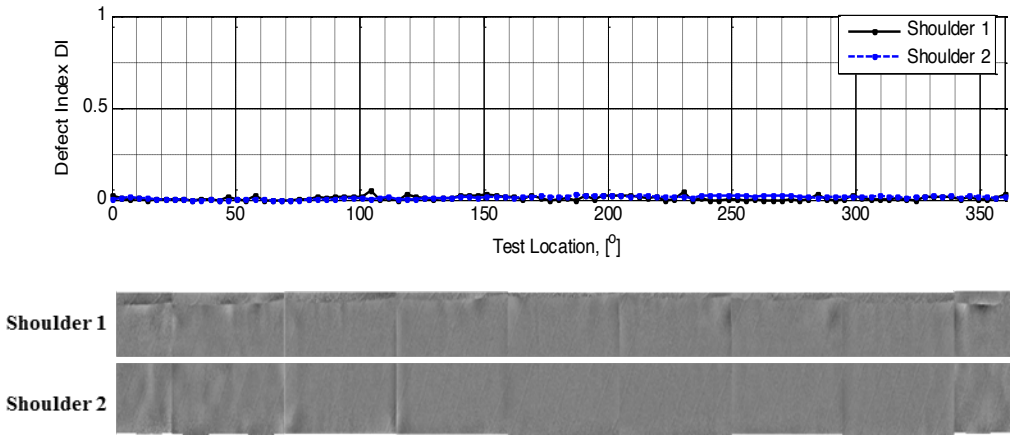

Figure 74: Defect indices for a brand new tire

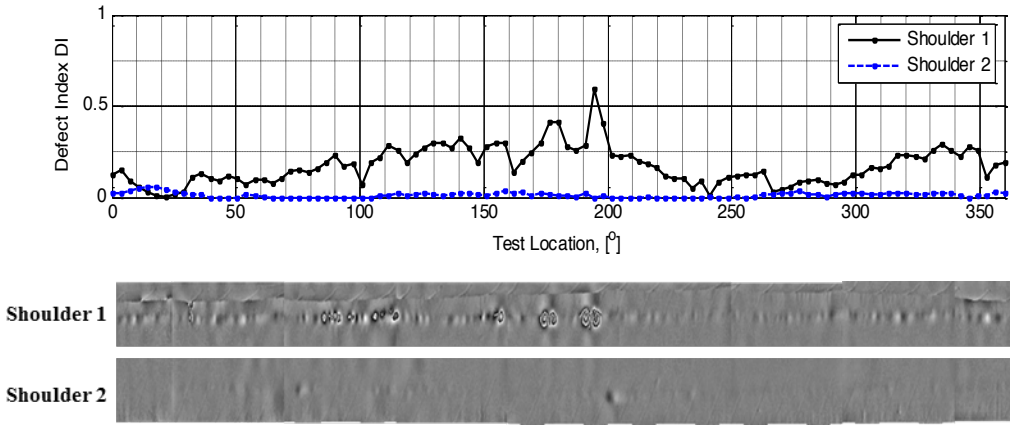

Figure 75: Defect indices for a tire with discontinuous small cracks in one shoulder

The extraction of discriminators and integration into a single defect index provide an indirect interpretation of the impact acoustic signals. Three discriminators (PR, P_f, E_f) are calculated from the power spectrum of the acoustic signals, which are reflections of energy shift from frequencies to frequencies. This phenomenon can be visually interpreted from the B scan mapping of the power spectrums, where the magnitude of the color map in Figure 76 displays the density of the power spectrum. The frequency is along the vertical axis, and the test location displayed along the horizontal axis. The top colormap shows the power spectrums from 500 to 2000Hz measured on the first shoulder, where the damaged areas display more colors of green or even red around 500-1000Hz. The other shoulder comparatively presents continuous blue color in this frequency band, indicating low magnitudes at flexural frequencies.

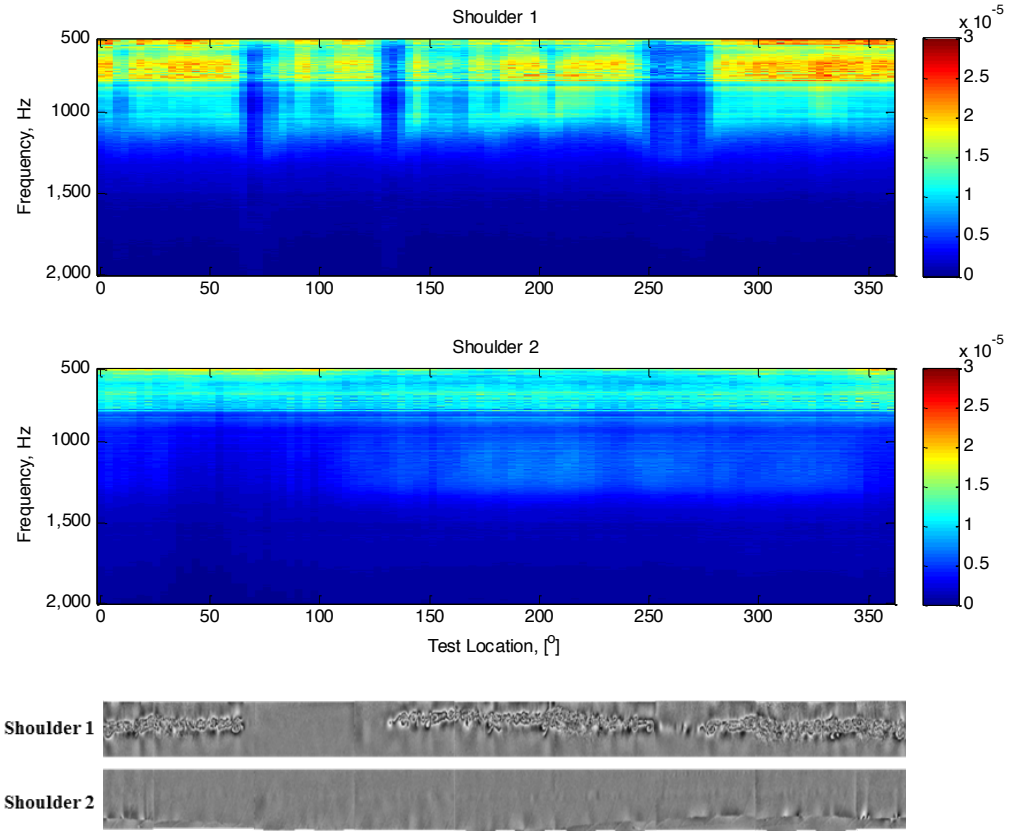

Figure 76: B scan imaging of the power spectrums measured from the representative tire

6 CONCLUSION

6.1 General Summary

This thesis presents the development of the impact acoustic based NDT method for delamination evaluation in rubber composite structure. Generally the impact acoustic method discussed herein has been analyzed in two aspects: the impact force and the impact induced acoustic sound. They can be measured by replacing a force sensor with the impactor's tip, and placing a microphone close to the impacted location respectively. It has been focused on seeking discriminators sensitive to the existence of crack from both measured signals.

Comprehensive modeling of the impact dynamics was provided firstly, continued with a series of sensitivity analysis for the parameters involved in the integral and defective model. The impact acoustic signal was analyzed from both time- and frequency-domain. Two stages of the impact acoustic signal were discussed, which are the initial contact sound stage, and the free vibration stage. Discussion about fundamentals of the formation of acoustic signal is significant to link the measured acoustic signal to the contact dynamic quantities that can be theoretically determined.

Both integral and defective contact dynamics model were developed for simplified cubic rubber blocks with laterally embedded cut-through crack, which approximates the sectional tire structure. Rationality of the approximation in the shapes has been based on the major presumption that the applied impact only introduces

mechanical responses in the nearby materials of the impacted body, which diminishes quickly with the increased distance from the exciting source. Another significant assumption is that the strains caused by the impact are so small that the rubber composite materials only behave in the linear region of the stress-strain curve. Experimental validation of the defect discriminators was carried out on the simplified rubber block samples before applied for defect inspections on tire casings.

Statistical analysis of the discriminators extracted from impact acoustic measurements for tire shoulders was given. By eliminating the most unrepeatable discriminator, six discriminators were considered as useful for identifying internal defects in the shoulder area of the tire casing. The purpose of making use of as many discriminators as possible in this thesis is to minimize the noises that may be introduced in a single discriminator and to optimize the capabilities of defect identification. Therefore an integration method by weighted averaging of the discriminators was developed. A single defect index was generated from the integration method accordingly as the indicator of the integrity conditions of the inspected tire shoulders.

6.2 Chapter 3 Conclusions

A simple spring-mass model was used and modified analyzing impact dynamics for the rubber composite material, which takes hysteretic effects into consideration. The model was developed for characterizing both integral and defective rubber structures. Fundamentally, the difference in the impact dynamics between integral and cracked

structure rests in the additional flexural vibrations introduced by the membrane formed by the crack. The impact dynamics can be analyzed as superposition of local contact dynamics and flexural bending effect. Four features in the impact dynamics mechanism can be predicted by the defect model, which are the peak impact force F_{max}, the impact duration τ, the maximum deformation d_{max}, and the flexural energy loss λ_f. They are correlated with two dimensional quantities which define the internal crack.

Sensitivity analysis of the parameters involved in derivations for the dynamic quantities is performed. The results indicate that the impact velocity V_i, the impactor's mass m_1 and the target's stiffness E_2 are the three most significant parameters that influence the four discriminators. By controlling m_1 and V_i as constant, the variations in the dynamic quantities can be regarded only attributed to stiffness change of the target structure, which in turn is the result of internal cracks. This assumption is valid while considering that the variations in the belts, foreign inclusions, and other effects that may vary the composite structural stiffness can be ignored. A local effective zone of the exerted impact is validated since the dynamic quantities are only sensitive to crack dimensions h and l within a limited range. The sensitivity range for h is larger than that for l, which indicates that the mechanical dynamics are only excited within a very limited local area around the impacted location, especially in the direction perpendicular to the impact. So the variances in the far field may not influence on the dynamic quantities.

6.3 Chapter 4 Conclusions

This chapter focuses on studying the impact force signal and impact-induced acoustic signal. The purpose is to target the corresponding experimental features that alternatively interpret the theoretical dynamic quantities, so that the relationships between the experimental features and the presence of internal crack can be established.

Impact force signal directly measures the peak impact force F_{max} and impact duration τ. The effects of internal crack dimensions on theoretically derived F_{max} and τ are given. Validation of the contact dynamics model is conducted on the cubic rubber blocks with cut-through cracks, which is the simplified case approximating the tire shoulders with belt edge separations. The samples are made of rubber compound which are used in the shoulder area of the interested tire casings for this thesis. Two block lengths of 101.6mm and 152.4mm are prepared with one integral sample and several cracked samples respectively. For each block length set, three different depths of crack combined with two different crack lengths make six cracked samples. F_{max} and τ measured directly from the experimental force signal show very small discrepancies from the theoretically predicted values. Experimental measurements on rubber blocks with 101.6mm and 152.4mm are compared, indicating that block length has minor influence on the discriminators. The presumption concluded earlier determines that it is rational to apply the results obtained for a cubic rubber block on a complicated shaped tire casing structure.

Both stages of the acoustic signal in time-domain were verified as related with the maximum deformation d_{max}. It has been proved according to the fundamentals of

acoustics that the area under the initial contact sound A_1 is proportional to d_{max}. Moreover, the accumulated area of the ringing sound amplitudes A_2 was also demonstrated as correlated with d_{max}. It has also been discussed that the flexural bending deformation introduced by the internal crack results in more frequency components at higher frequency bandwidth, which in turn yields frequency-domain features extracted from the acoustic signal. Three types of energy related discriminators are determined as correlated with internal defects, which are the accumulative power ratio PR, the peak spectral density P_f and the accumulative spectral energy E_f. It has been both theoretically and experimentally verified that all the three features are well connected with the flexural energy loss factor λ_f.

6.4 Chapter 5 Conclusions

In the experimental study for tire casing integrity inspection, the focus is mainly on the belt edge separations in the shoulder areas. Three tire samples are provided, where one representative tire contains extensive belt edge cracks in one shoulder, one is brand new, and the other is slightly damaged in one shoulder. The conditions of the tire are almost completely relied on another NDT tire inspection method, which is the shearography imaging technique. The method can be insensitive to the separations close to the outer diameter of the tire casing. The non-damaged region of the first representative tire sample indicated by the shearography image was double checked by destructive method, which reveals some damages. These unseen damaged conditions

through the shearography testing method are pointed out by the impact acoustic discriminators, which indicate that the impact acoustic method can be a promising substitution of the expensive shearography technique.

Furthermore, the six most robust impact discriminators are summarized for the representative tire sample. They correlate well with the damaged conditions indicated by the shearography image. However, some of the discriminators such as PR are less sensitive to the variations in the damage even though it exhibits great distinction between damaged and non-damaged measurements, and also shows impressive test repeatability. Some discriminators such as F_{max} and τ present opposite characteristics to PR. It indicates that integration of all the promising discriminators may mitigate the deficiencies and noises introduced by a single discriminator. Average of the six normalized discriminators is defined as defect index DI. Each discriminator for the three different samples is normalized by the same denominator taken from the representative tire shoulder. The results based on the single defect indicator DI for all the three tire samples agree with the shearography results quite well. The use of statistical characteristics balanced weighting parameters is recommended to improve the current integration method in the future.

REFERENCES

Armstrong P. R., Stone M. L. and Brusewitz G. H. Peach firmness determination using two different nondestructive vibrational sensing instruments [Journal]. - [s.l.] : Transactions of the ASAE, 1997. - 3 : Vol. 40.

Armstrong P. R., Zapp H. R. and Brown G. K. Impulsive excitation of acoustic vibrations in apples for firmness determination [Journal]. - [s.l.] : Transactions of the ASAE, 1990. - Vol. 33. - pp. 1353-1359.

Asano M. [et al.] Impact acoustics methods for defect evaluation in concrete [Online] // Non-Destructive Testing in Civil Engineering. - 2003. - http://www.ndt.net/article/ndtce03/papers/v040/v040.htm.

ASTM C 1383 Test method for measuring the P-wave speed and the thickness of concrete plates using the impact-echo method // 2000 Annual Book of ASTM Standards. - West Conshohocken : ASTM.

Berger H. An overview: new ideas in nondestructive evaluation [Journal]. - [s.l.] : Rubber Chemistry and Technology, 1981. - 5 : Vol. 54. - pp. 996-1002.

Borza D. N. Specialized techniques in holographic non-destructive testing of composites [Journal]. - [s.l.] : Composites Part B: Engineering, 1998. - Vol. 29. - pp. 497-504.

Boustani Avid [et al.] Tire Remanufacturing and Energy Savings [Report]. - [s.l.] : MITEI, 2010.

Cheng C. and Sansalone M. Determining the Minimum Crack Width that can be Detected Using the Impact-echo Method, Part I: Experimental Study [Journal] // RILEM Journal of Materials and Structures. - 1995a. - Vol. 28. - pp. 74-82.

Cheng C. and Sansalone M. Determining the Minimum Crack Width that can be Detected Using the Impact-echo Method, Part II: Numerical Fracture Analyses [Journal] // RILEM Journal of Materials and Structures. - 1995b. - Vol. 28. - pp. 125-132.

Christoforou A. P. and Yigit A. S. Effect of flexibility on low velocity impact response [Journal]. - [s.l.] : Journal of Sound and Vibration, 1998. - 3 : Vol. 217. - pp. 563-578.

dos Reis H. L.M. and Golko P. J. On the instrument to evaluate damage in steel belted radial truck tires [Journal]. - [s.l.] : Kautschuk Gummi Kunststoffe, 2000. - 12 : Vol. 53. - pp. 694-700.

Downs Justin, Zhang Peihong and Peterson M. L. A high-speed high-resolution ultrasonic inspection machine [Journal]. - [s.l.] : IEEE/ASME Transactions on Mechatronics, 1999. - 3 : Vol. 4.

Forney J. M. Proceedings of the Second Symposium on Nondestructive Testing of Tires [Conference] // the Army Materials and Mechanics Research Center / ed. Vogel Paul E.J.. - Watertown,MA : [s.n.], 1974. - p. 13.

Gent A N Strength of Elastomers [Book] / ed. Mark J E, Erman B and Eirich F R. - [s.l.] : Academic Press, 1994. - pp. 471-512.

Gent A. N. and Walter J. D. The Pneumatic Tire [Book]. - [s.l.] : NHTSA, 2005.

Gent A. N. and Walter J. D. The Pneumatic Tire [Book]. - [s.l.] : NHTSA, 2005.

Goldsmith W. Impact: The theory and Physical Behavior of Colliding Solids [Book]. - [s.l.] : Edward Arnold Press, Ltd., 1965.

Heirtzler F. and Hill W. Tire Defect Detection System and Method [Patent] : US Patent 6381547 B1. - April 30, 2002.

Hung Y. Y. A speckle-shearing interferometer: a tool for measuring derivatives of surface displacements [Journal]. - [s.l.] : Optics Communications, 1974. - 132-135 : Vol. 11.

Hung Y. Y. Shearography for non-destructive evaluation of composite structures [Journal]. - [s.l.] : Optics and Lasers in Engineering, 1996. - Vol. 24. - pp. 161-182.

Ito Y. and Uomoto T. Nondestructive testing method of concretre using impact acoustics [Journal]. - [s.l.] : NDT&E Int., 1997. - 4 : Vol. 30. - pp. 217-222.

Kim Koungsuk [et al.] Non-destructive evaluation of separation and void defect of a pneumatic tire by speckle shearing interferometry [Journal]. - [s.l.] : KSME International Journal, 2004. - 9 : Vol. 18. - pp. 1493-1499.

Krautkramer Josef and Krautkramer Herbert Ultrasonic testing of materials [Book]. - [s.l.] : Springer - Verlag New York, Inc., 1977. - p. 667.

Lin J. M. and Sansalone M. The Impact-Echo Response of Hollow Cylinderical Concrete Structures Surrounded by Soil or Rock, Part 1 - Numerical Studies [Journal]. - [s.l.] : American Society of Testing and Materials - Journal of Geotechnical Testing, 1994a. - 2 : Vol. 17. - pp. 207-219.

Lin J. M. and Sansalone M. The Impact-Echo Response of Hollow Cylindrical Concrete Structures Surrounded by Soil or Rock, Part 2 - Experimental Studies [Journal]. - [s.l.] : American Society of Testing and Materials - Journal of Geotechnical Testing, 1994b. - 2 : Vol. 17. - pp. 220-226.

Lin J. M. and Sansalone M. The Transverse Elastic Impact Response of Thick Hollow Cylinders [Journal]. - [s.l.] : Journal of Nondestructive Evaluation, 1993. - 2 : Vol. 12. - pp. 139-149.

Luk B. L., Liu K. P. and Tong F. Rapid evaluation of tile-wall bonding integrity using multiple-head impact acoustic method [Journal]. - [s.l.] : NDT&E International, 2011. - Vol. 44. - pp. 297-304.

Mark James E, Erman Burak and Eirich Frederick R Science and Technology of Rubber (3rd Edition) [Book]. - [s.l.] : Elsevier Academic Press, 2005.

Mark James E, Erman Burak and Eirich Frederick R Science and Technology of Rubber (3rd Edition) [Book]. - [s.l.] : Elsevier Academic Press, 2005.

Mujumdar P. M. and Suryanarayan S. Flexural vibrations of beams with delaminations [Journal]. - [s.l.] : Journal of Sound and Vibration, 1988. - 3 : Vol. 125. - pp. 441-461.

Mujumdar P. M. and Suryanarayan S. Flexural vibrations of beams with delaminations [Journal]. - [s.l.] : Journal of Sound and Vibration, 1988. - 3 : Vol. 125.

Muthukumar Susendar A contact element approach with hysteresis damping for the analysis and design of pounding in bridges [Journal]. - [s.l.] : Georgia Institute of Technology, 2003. - pp. 80-85.

Rens K L, Wipf T J and Klaiber F W Review of non-destructive evaluation techniques of civil infrastructure [Journal]. - [s.l.] : J. Perf. Constr. Facilities, 1997. - 4 : Vol. 11. - pp. 152-60.

RMA Scrap Tire Markets in the United States 9th Biennial Report [Report]. - [s.l.] : Rubber Manufacturers Association, 2009.

Roark R. J. Formulas for Stress and Strain [Book]. - New York : McGraw-Hill, 1954.

Sansalone M J and Carino N J Impact-Echo: A Method for Flaw Detection in Concrete Using Transient Stress Waves [Journal]. - Gaithersburg, Maryland : National Bureau of Standards, 1986.

Sansalone M J and Carino N J Impact-Echo: A Method for Flaw Detection in Concrete Using Transient Stress Waves [Journal]. - Gaithersburg, Maryland : National Bureau of Standards, 1986.

Sansalone M J and Carino N J Impact-Echo: A Method for Flaw Detection in Concrete Using Transient Stress Waves [Journal]. - Gaithersburg, Maryland : National Bureau of Standards, 1986.

Sansalone Mary J Flaw Detection in Concrete Using Transient Stress Waves [Book]. - [s.l.] : Ph.D. Dissertation, Cornell University, 1986.

Sansalone Mary J. and Streett William B. Impact-Echo: Nondestrucitve Evaluation of Concrete and Masonry [Book]. - [s.l.] : Bullbrier, 1997.

Zou Y., Tong L. and Steven G. P. Vibration-based model-dependent damage(delamination) identification and health monitoring for composite structures - a review [Journal]. - [s.l.] : Journal of Sound and Vibration, 2000. - 2 : Vol. 230. - pp. 357-378.

Zukas Jonas A. [et al.] Impact Dynamics [Book]. - Malabar, FL : Krieger Publishing Company, 1992.